DEVELOPMENTS IN THE FIELD OF ENGINEERING 2025

Editor:

Prof. Dr. Ahmet TURŞUCU

Assoc. Prof. Dr. Sedat ÖZCANAN

yaz

yayınları

DEVELOPMENTS IN THE FIELD OF ENGINEERING 2025

Editors

Prof. Dr. Ahmet TURŞUCU

Assoc. Prof. Dr. Sedat ÖZCANAN

yaz yayınları

2025

yaz
yayınları

Developments in the Field of Engineering 2025

Editor: Prof. Dr. Ahmet TURŞUCU

ORCID NO: 0000-0002-4963-697X

Editor: Assoc. Prof. Dr. Sedat ÖZCANAN

ORCID NO: 0000-0002-8504-7611

E_ISBN 978-625-8508-85-7

Aralık 2025 – Afyonkarahisar

Dizgi/Mizanpaj: YAZ Yayınları

Kapak Tasarım: YAZ Yayınları

YAZ Yayınları. Yayıncı Sertifika No: 73086

M.İhtisas OSB Mah. 4A Cad. No:3/3
İscehisar/AFYONKARAHİSAR

www.yazyayinlari.com

yazyayinlari@gmail.com

info@yazyayinlari.com

CONTENTS

LOCUS ANALYSIS AND THE EFFECT OF GAIN VARIATION ON SYSTEM STABILITY

Mehmet Latif LEVENT[1]

Mehmet Sefik UNEY[2]

1. INTRODUCTION

In control systems, determining the optimal gain value for the controller is crucial to enhance system performance and ensure overall stability (Goble, 2010). Various methods have been developed to meet such criteria, and among the most effective of these is the root locus technique. When this method is analyzed, it is observed that the closed loop poles of the controller system move to different regions of the complex plane depending on the gain value. The graphical technique that illustrates this movement is known as the root locus technique (Evans, 2009). Using this method, the system's output response curve, transient behavior, and overall stability can be effectively analyzed (Ogata, 2010).

The root locus plots obtained from the zeros and poles of the open loop transfer function show how the pole locations vary with different gain values. Accordingly, it becomes possible to determine for which gain range the system remains unstable or becomes stable. As a result, performance parameters such as overshoot, damping ratio, and settling time can be identified and

[1] Asst. Prof. Dr., Hakkari University, Faculty of Engineering, Department of Electrical and Electronics Engineering, Hakkari/Türkiye, ORCID: 0000-0002-7185-9029.

[2] Asst. Prof. Dr., Batman Üniversitesi, Department of Electricity and Energy, Vocational School, Batman University, Turkey, ORCID: 0000-0003-4743-0764

adjusted by the designer to achieve the desired system response. (Gumussoy & Michiels, 2020).

In this study, the root locus technique is employed to analyze the system's output response and stability characteristics. The second chapter presents general information about root locus theory and outlines the steps involved in constructing root locus plots. To facilitate a clearer understanding of the method, several different examples are examined and discussed. In the third chapter, sample applications are carried out in the MATLAB/Simulink environment, and the obtained plots are analyzed in detail. This section also includes the unit step response of the controller system for different gain values.

2. ROOT LOCUS PLOTS

The root locus illustration provides a visual representation of how the system's characteristic roots of a control system shift when the feedback gain K is altered. This graphical analysis offers an intuitive way to interpret the system's dynamic characteristics and stability trends. The foundation of this method lies in the the stability-defining equation, which is typically expressed as: $1+G_sH_s=0$. Where $H_s(s)$ *and* $G_s(s)$ denote the feedback transfer functions and open loop respectively (Dorf & Bishop, 2011). As the value of gain parameter varies, the corresponding locations of the closed loop poles migrate within the complex s-plane. The continuous trajectories traced by these poles are referred to as the root loci. Root locus analysis enables designers to determine gain parameters for which the closed loop system remains stable. Each trajectory starts from the poles associated with the open-loop transfer function and completes either at the open loop zeros or extends toward infinity, depending on the number of poles and zeros. By visualizing these trajectories, one can gain valuable insight into how changes in gain affect the

transient and system's steady-state behavior (Kuo & Golnaraghi, 2003). Overall, the root locus approach serves as a powerful and efficient graphical framework that assists in evaluating system stability and performance under varying gain conditions (Chen & Lee, 2018).

2.1. Closed-Loop Structure

Illustrated in Figure 2.1 is a classical control system with negative feedback. Through the forward path transfer function, comprising the controller and the plant, the reference curve $R_{plant}(s)$ is transmitted to the output $Y_{plant}(s)$. Simultaneously, a portion of the output signal is feedback to the input via the feedback element $H_{plant}(s)$. The objective of such systems is to ensure that the output signal follows the input signal within an acceptable error margin. Feedback is employed to enhance stability, reduce steady state error and improve the system's performance (Di Bernardo et. al, 2013).

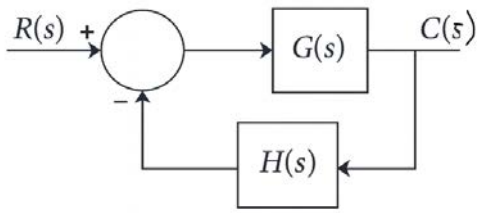

Figure 2.1. A Classical Negative Feedback Control System

When defining the transfer function of a system, the ratio of the output to the input is calculated. The expression of the transfer function is given in Equation (1).

$$T_s(s) = \frac{C_s(s)}{R_s(s)} = \frac{G_s(s)}{1 + H_s(s)G_s(s)} \tag{1}$$

Here, $G_s(s)$, $H_s(s)$ and $T_s(s)$ defined the open loop transfer function, feedback transfer functions, closed loop transfer function respectively. The denominator term in Equation (1) defines the system's characteristic equation, which is subsequently expressed in Equation (2).

$$1+G_s(s)H_s(s)=0 \tag{2}$$

This equation determines the poles of the system and consequently, its stability. It serves as the foundation for root locus analysis, as it defines how the poles of closed loop shift in the complex plane with variations in value of K_{plant}.

Thus, the closed-loop arrangement presented in Figure 2.1 represents a fundamental model in classical control theory, defining the system's dynamic behavior, stability, and steady-state error characteristics. In Equation (3), the transfer function of open loop is defined as the product of the forward path and feedback transfer functions.

$$G_s(s)H_s(s) = K_{plant}\frac{N_s(s)}{D_s(s)} \tag{3}$$

Here, K_{plant} is a scalar gain constant, while $D_s(s)$ and $N_s(s)$ denote the denominator and numerator polynomials of the open-loop system, respectively. The expanded version of the expression in Equation (3) is shown in Equation (4).

$$G_s(s)H_s(s)=\frac{K_{plant}\left(s+m_1\right)\left(s+m_2\right)\left(s+m_3\right)....\left(s+m_a\right)}{\left(s+k_1\right)\left(s+k_2\right)\left(s+k_3\right)....\left(s+k_b\right)} \tag{4}$$

In this equation, the terms m_a represent the zeros of the system, which appear in the numerator and influence the dynamic behavior by adding phase lead. Zeros are typically introduced through controller design and have a significant impact on shaping the transient behaviour. The denominator in this equation is especially significant, since the poles it contains are directly

proportional to and therefore indicative of the system's stability. he system is stable when the poles are in the left half-plane (negative real part) and unstable when they lie in the right half-plane (positive real part).

The gain K_{plant} acts as a positive scalar that adjusts the overall amplitude response of the system. In root locus analysis, this parameter is crucial since it can alter the pole locations. The denominator polynomial defines the intrinsic dynamics of the system, while the numerator polynomial represents the influence of the controller.

Therefore, this formulation completely characterizes the open-loop behavior of a control system. In root locus analysis, it is used to visualize how the poles move in the complex plane as K_{plant} increases, satisfying the fundamental condition $G_s(s)H_s(s) = -1$. Since the magnitude of -1 is 1 and its phase is $(2\ell+1)\pi$, two essential conditions emerge: the angle condition and the magnitude condition. The angle condition is given as:

$$\angle\left[G_s(s)H_s(s)\right] = \angle\left[K_{plant}\frac{N_s(s)}{D_s(s)}\right] = \sum_{i=1}^{a}\angle(s+m_a) - \sum_{i=1}^{b}\angle(s+k_b) = (2\ell+1)\pi,\ \ell \in Z. \tag{5}$$

If a point s satisfies the angle condition, the root locus can pass through that point for a certain gain K_{plant}. The gain condition is expressed as:

$$\left|G_s(s)H_s(s)\right| = \left|K_{plant}\frac{N_s(s)}{D_s(s)}\right| = 1 \Rightarrow K_{plant} = \left|\frac{D_s(s)}{N_s(s)}\right| \tag{6}$$

By applying these angle and magnitude conditions, root locus plots can be drawn for any system. If the gain K_{plant} at a specific point on the root locus is desired, it can be determined directly from the magnitude condition. Computer-aided tools,

such as MATLAB, utilize these relationships to plot root loci efficiently. Root locus analysis is instrumental in determining all possible pole locations, identifying stability regions as a function of K and aiding in the design of suitable controllers to achieve desired system performance.

2.2. Procedures for Plotting Root Locus

To construct a root locus plot, the transfer function of open loop must first be defined, as given in Equation (7):

$$G_s(s)H_s(s) = K_{plant}\frac{N_s(s)}{D_s(s)} = K_{plant}\frac{\prod_{a=1}^{i}(s+m_a)}{\prod_{b=1}^{j}(s+k_b)} \tag{7}$$

Here, K represents the scalar gain, m_a the zeros of open loop, k_b the poles of open-loop, a the zero count, and b the pole count. From this expression, it is clear that the system possesses *n-pole, m-zero*. The root locus analysis investigates how the poles of the closed-loop move as K_{plant} changes from *0* to infinity. When $K_{plant}=0$, It is noted that the closed-loop poles coincide with the open-loop poles. As $K_{plant}\to\infty$, A tendency of the closed-loop poles to approach the open-loop zeros is observed. Thus, the branches of root locus originate at the poles of open loop (when $K_{plant}=0$) and terminate either at the zeros of open-loop or at infinity (when $K_{plant}\to\infty$). If the number of poles exceeds the number of zeros ($b>a$), then $b-a$ branches extend toward infinity along asymptotic lines, which represent the directions of the infinite zeros (Steiglitz, 1969).

To demonstrate how the beginning and end points of the root-locus trajectories are determined, Consider a simple open-loop transfer function having two poles. This example clearly illustrates the behavior of the system for $K_{plant}\to\infty$ and $K_{plant}=0$. The transfer function of open loop is given by Equation (8):

$$G_s(s)H_s(s) = K_{plant}\frac{1}{s(s+2)} \tag{8}$$

From this equation, it is clear that the control structure has no zeros, but two poles located at $k_1=0$ and $k_2=-2$. Therefore, since $b-a=2$, two root locus branches will be plotted, each extending to infinity.

When $K_{plant}=0$, the poles of closed loop coincide with the poles of open loop; that is, the loci start at $k_1=-2$ and $k_2=0$. As the gain K_{plant} increases, the poles begin to move in the complex plane: one pole moves leftward along the negative real axis, while the other departs from the real axis and heads toward infinity along an asymptotic path.

Consequently, in this system, one part of the root locus lies along the real axis between $-2<s<0$, while the other branch leaves this region and extends toward infinity. This clearly shows how pole locations change with gain variation, thereby influencing the system's stability. To gain a deeper understanding of root locus plotting, consider another open-loop transfer function given in Equation (9):

$$G_s(s)H_s(s) = K_{plant}\frac{(s+1)}{s(s+2)} \tag{9}$$

This system has one zero and two poles. The zero is located at $k_1=-1$ while the poles are placed at $s=0$, $s=-2$. The pole-zero difference is $b-a=1$, which means one branch of the root locus terminates at a finite zero, and the other extends toward infinity.

When $K_{plant}=0$, the closed-loop poles coincide with the open-loop poles at $s=0$ and $s=-2$. As K increases, the poles move, affecting the stability of the system. One pole approaches the zero at $s=-1$, while the other departs from the real axis and extends toward infinity. On the real axis, the portion of the root locus lies between $s=-2$ and $s=-1$. In this region, the poles move along the negative real axis. At $s=-1$, one branch terminates, while the

other departs toward infinity. This reveals how the pole locations change as the gain *K* increases. Using MATLAB, the system can be represented as *Gs = tf([1 1],[1 2 0]); rlocus(Gs)*. Figure 2.2 illustrates the resulting root-locus of the system, where poles are indicated by "×" and zeros by "○".

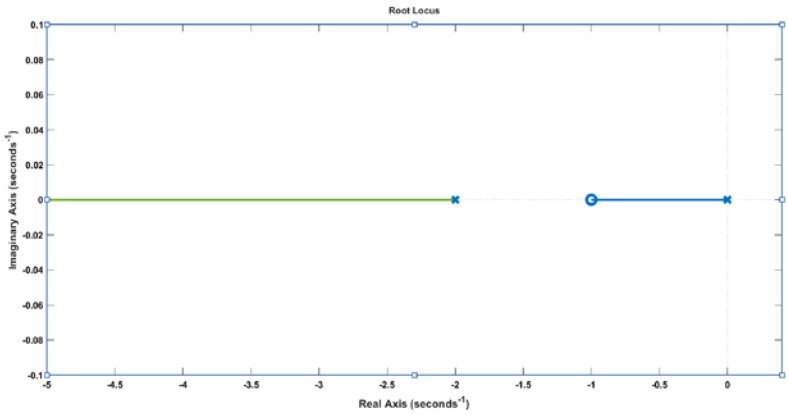

Figure 2.2. Closed-Loop Pole Trajectories for the System in (9) (Root Locus).

This example serves as a fundamental illustration of how root loci originate from poles and terminate at zeros or infinity, and how the direction of pole movement changes with variations in the system gain. When constructing a root locus plot, the following general steps are applied:

1. Identify the singularities (poles and zeros) of $H_s(s)G_s(s)$.
2. The For $K_{plant}=0$, the identified poles are chosen as the origin points of the root loci
3. The for $K_{plant}=\infty$, the identified poles are chosen as the origin points of the root loci.
4. If $b>a$, $b-a$ branches terminate at infinity (Evans, 1950).

The symmetry property of root locus plots should also be noted: the root loci are symmetric about the real axis. This is because the characteristic equation (Equation 2) has real

coefficients, and hence, complex roots appear as conjugate pairs. That is, if $s=\sigma+j\omega$ is a root, then $s=\sigma-j\omega$ must also be a root. Consequently, the root locus is always symmetric with respect to the $j\omega$-axis. To illustrate this property, transfer function of open-loop for system is given Equation (10).

$$G_s(s)H_s(s)=\frac{K_{plant}}{s(s^2+4s+8)} \tag{10}$$

This system has one real pole at $k_1=0$ and two complex conjugate poles at $k_{2,3}=-2\pm j$. Thus, the system is of third order. The root loci originate from these poles — one on the real axis and two as complex conjugates — and are symmetric about the real axis due to the complex conjugate nature of the poles. As K_{plant} increases, the locus starting from $s=0$ moves leftward, while the loci emerging from the complex poles bend upward and downward, diverging symmetrically. This motion directly affects system stability: as the poles approach the imaginary axis, the damping ratio decreases; if they cross it, the system becomes unstable. This example clearly demonstrates the relationship between system gain and pole locations. The symmetry of the root loci with respect to the real axis reflects the physical nature of linear time-invariant systems and serves as an essential indicator in both stability analysis and controller design. In Figure 2.3, the root locus plot corresponding to Equation (10) is illustrated.

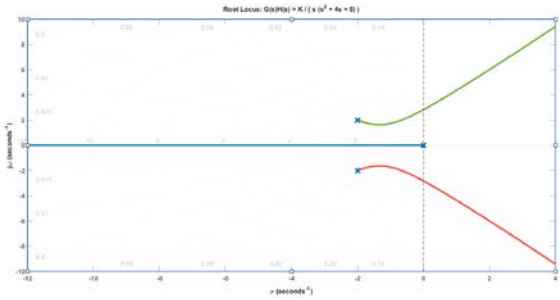

Figure 2.3. Root-Locus Representation Defined by Equation (10) in the MATLAB Environment

When drawing root loci, the asymptotes provide guidance for plotting the branches that extend toward infinity. For a system in which the number of poles is greater than the number of zeros ($b>a$), then $b-a$ branches of the root locus will move toward infinity along straight lines called asymptotes. These lines indicate the general direction of the root locus branches at high gain values and are crucial for predicting the overall shape of the locus.

The number of asymptotes is equal to $b-a$, and their angles with respect to the real axis are determined by the general formula:

$$\theta_k = \frac{(2k+1)180°}{n-m}, \quad (k = 0,1,2,\ldots) \tag{11}$$

In this formula, k represents the index of each asymptote.

- For $b-a=1$, there is one asymptote at 180^o, extending leftward along the negative real axis.
- For $b-a=2$, the asymptotes are at $+90^o$ and -90^o, directed vertically upward and downward.
- For $b-a=3$, they appear at $+60^o$, 180^o, and -60^o.
- For $b-a=4$, the asymptotes are located at $+45^o$, $+135^o$, -45^o, and $+135^o$.

Hence, the number and orientation of the asymptotes depend directly on the system order (b) and the number of zeros (a).

All asymptotes cross the real axis at the same point called the centroid (σ_a). This point indicates where the asymptotes cross the real axis and is calculated as:

$$\sigma_a = \frac{\sum k_b - \sum m_a}{b-a} \tag{12}$$

Here, $\sum k_b$ represents the sum of the overall number of poles and $\sum m_a$ denotes the sum of the overall number of zeros. The computed centroid value defines the intersection point of all asymptotes on the real axis. In summary, the number of asymptotes equals $b-a$, their angles θ_k are determined using Equation (11), and they all intersect at the centroid σ_a given by Equation (12). These geometric properties allow the designer to predict the general form and direction of the root locus even before the full plot is generated.

3. CASE STUDY IN MATLAB / SIMULINK ENVIRONMENT

In this section, the root locus and unit-step response analyses of the system defined by Equation (13) are carried out for various gain values K_{plant} using the MATLAB/Simulink environment.

$$G_s(s)H_s(s) = \frac{K_{plant}(s+1)}{s(s+3)(s^2+4s+16)} \tag{12}$$

In MATLAB, the open-loop poles of a system can be determined by calculating the roots of the denominator polynomial. The built-in function *roots()* is typically used for this purpose. This function computes the poles of the system based on the denominator coefficients of the transfer function. As a result, four poles are obtained for this system. The centroid (σ_a) of the root locus, which represents the intersection point of the asymptotic branches on the real axis, is calculated as follows:

$$\sigma_a = \frac{(-3)+(-2+j2\sqrt{3})+(-2-j2\sqrt{3})-(-1)}{4-1} = -2$$

Thus, the intersection point of the asymptotes lies at $\sigma_a=-2$. The corresponding root locus plot obtained in MATLAB is shown in Figure 3.1.

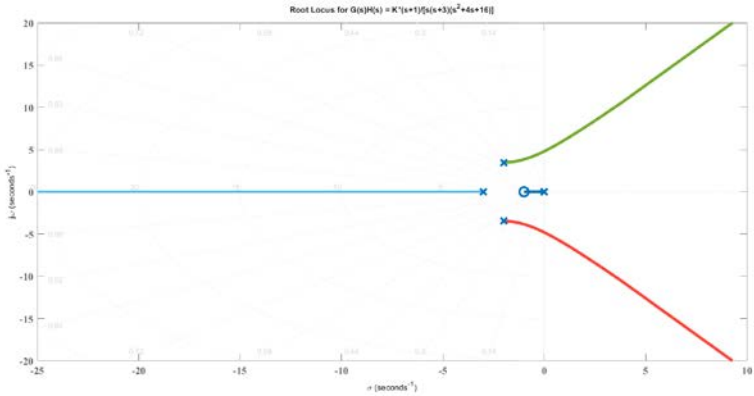

Figure 3.1. Root Locus Plot of the System Defined by Equation (13) in MATLAB

When $K_{plant}=0$, all poles are located in the left-half plane, indicating that the system is stable. However, as the gain K increases, the complex poles move toward the right-half plane. This implies that beyond a certain critical gain, the system becomes unstable. The exact value of critical gain can be determined using Nyquist or Routh–Hurwitz stability criteria.

The MATLAB/Simulink model of the system is shown in Figure (3.2) In this model, the characteristic equation is expressed as a single polynomial, and the feedback path is assumed to be $H_s(s)=1$.

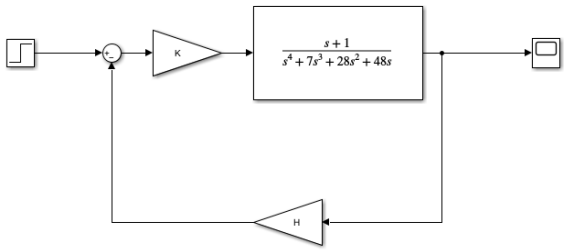

Figure 3.2. Simulink Model of System Defined by Equation (11)

The unit-step response of the system for different gain values is presented in Figure 3.3. This figure clearly illustrates the dynamic behavior of the system as a function of the gain K_{plant}. For $K_{plant}=10$, the system exhibits a slow, non-oscillatory, and overdamped response.

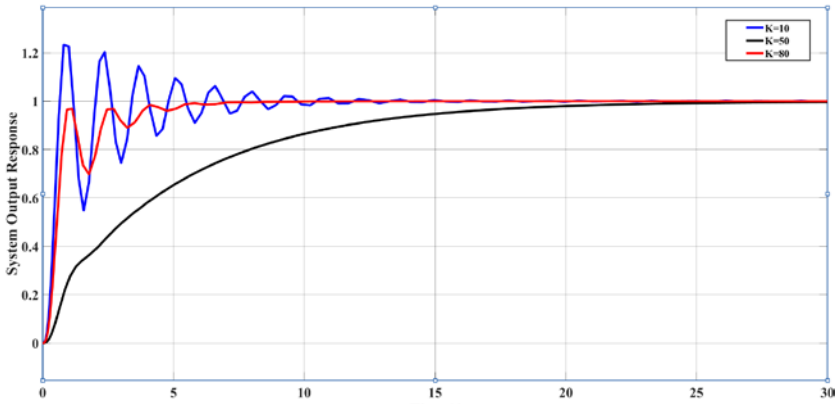

Figure 3.3. Step Responses of the System for Different Gain Values

When $K_{plant}=50$, the system responds faster, but noticeable overshoot and damped oscillations appear. This behavior corresponds to the movement of the complex poles in the left-half plane observed in the root locus plot. At $K_{plant}=80$, the system remains stable but exhibits higher oscillations, and the settling time increases. As the gain grows, the system response becomes faster but less damped, resulting in a larger overshoot. In conclusion, to achieve a stable, fast, and well-balanced response, the gain K_{plant} should be selected within a moderate range. Excessively high gains can lead to instability, whereas very small gains cause sluggish performance.

4. CONCLUSION

In this study, the stability characteristics of a feedback control system were examined through the root locus technique,

emphasizing the influence of the gain parameter K_{plant} on the overall system dynamics. The analysis revealed that variations in K_{plant} have a pronounced effect on the transient and steady-state performance of the system. Because the root locus method graphically depicts the movement of closed-loop poles in the complex domain, it provides an effective means of determining the stability boundaries and assessing the dynamic response of the system. Simulation outcomes showed that when the gain is relatively small, the system behaves in a stable yet sluggish manner, exhibiting minimal oscillations. As the gain increases, the response becomes faster but introduces greater overshoot and damping oscillations. At excessively high gain levels, the dominant poles approach the imaginary axis, which reduces the damping ratio and may eventually lead to instability. These behaviors are consistent with the theoretical pole trajectories observed in the root locus analysis. Therefore, the proper selection of the gain parameter is essential for maintaining a balance between response speed and stability. Choosing a gain value that is too large can cause instability, whereas an insufficient gain results in a slow response. Consequently, the root locus approach remains a practical and reliable design tool for achieving an optimal trade-off between system stability and transient performance. Future work could explore advanced control strategies such as PID, PD, or Lead–Lag compensators, optimized through the root locus framework, to further enhance both stability and transient dynamics.

REFERENCES

Chen, C., & Lee, T. (2018). Root locus analysis for nonlinear systems. IEEE Transactions on Control Systems Technology, 26(4), 1213–1222.

Di Bernardo, M., Budd, C. J., Champneys, A. R., & Kowalczyk, P. (2013). *Piecewise-smooth dynamical systems: Theory and applications*. Springer.

Dorf, R. C., & Bishop, R. H. (2011). *Modern Control System* (12th ed.). Pearson.

Evans, W. R. (1950). Control system synthesis by root locus method. *Transactions of the American Institute of Electrical Engineers, 69*(1), 66–69.

Evans, W. R. (2009). Control system synthesis by root locus method. *Transactions of the American Institute of Electrical Engineers, 69*(1), 66–69.

Goble, W. M. (2010). *Control systems safety evaluation and reliability*. ISA.

Gumussoy, S., & Michiels, W. (2020). *Root locus for SISO dead-time systems: A continuation based approach.* arXiv. https://arxiv.org/abs/2003.09253

Kuo, B. C., & Golnaraghi, F. (2003). *Automatic Control Systems* (8th ed.). John Wiley & Sons.

Ogata, K. (2010). *Modern Control Engineering* (5th ed.). Prentice Hall.

Steiglitz, K. (1969). An analytical approach to root loci. *IEEE Transactions on Automatic Control*, 14(1), 17-23.

BEYOND MATERIALS: NEW PARADIGMS OF MATTER IN THE AGE OF ARTIFICIAL INTELLIGENCE

Cengiz SOYKAN[1]

1. INTRODUCTION: The Crisis of Discovery and the Dawn of a New Era

Material science stands as one of the oldest disciplines in human history, with its origins tracing back to clay shaped by primordial fires and the first metals forged by hammer. Traditionally, this progress has been driven by empiricism - the iterative process of synthesizing a material, characterizing it, testing it, and recording its properties. This approach has initiated numerous revolutions, from bronze to steel, and silicon to high-temperature superconductors. However, as we enter the 21st century, this conventional method faces what can be termed a "discovery crisis." The chemical space of potentially synthesizable organic materials is estimated to be on the order of 10^{60}, constituting a search space vastly larger than the estimated number of atoms in the observable universe ($\sim 10^{80}$) (Aghanim, 2020; Eddington, 1920; Ryden, 2006). Human lifespans and resources have become increasingly inadequate for this discovery process, akin to searching for a needle in an oceanic expanse.

This crisis simultaneously heralds a radical transformation. Virtual screening techniques have emerged as a groundbreaking tool for molecular discovery, enabled by the

[1] Assoc. Prof. Dr., Kırşehir Ahi Evran University, Health Services Vocational School, Department of Medical Services and Techniques, ORCID: 0000-0003-0897-2384.

exponential growth in available computational power and the continuous refinement of simulation and machine learning methods. The multidisciplinary integration of theoretical prediction, quantum chemistry and physics, chemoinformatics, machine learning, industrial expertise, organic synthesis, and molecular characterization has accelerated scientific progress at an unprecedented rate (Gómez, 2016).

For instance, extensive research on the electronic and optoelectronic properties of complex oxides like $SrTiO_3$ (strontium titanate) and perovskites such as $CsPbI_3$ (cesium lead iodide) has provided us with vast datasets of material properties. The central challenge has consequently shifted from merely synthesizing more materials to interpreting this "big data" and extracting novel insights from it.

This chapter examines this paradigmatic evolution in materials science - from empiricism to rationalism, and onward to artificial intelligence (AI)-driven autonomous discovery. Our central argument posits that we are currently experiencing a fundamental shift that is transforming not merely which "materials" we study, but the very mindset through which we design, simulate, and discover them. The tangible outcomes of this paradigm shift can be observed across a broad spectrum of applications, ranging from shape-memory alloys and next-generation solar cells to hydrogen storage materials and advanced optical glasses (Kaya Soykan, 2023; Soykan, 2014; Soykan, 2019; Soykan, 2019; Soykan, 2020; Soykan, 2025).

2. HISTORICAL ROOTS: From Empiricism to Quantum Rationalism

The early stages of materials science were based entirely on empirical observations. A blacksmith could enhance the properties of steel through practical knowledge transmitted across

generations, without any understanding of quantum mechanics. The beginning of the 20th century fundamentally transformed this paradigm. The discovery of quantum mechanics unveiled the microscopic world of matter, enabling us to correlate macroscopic material properties (conductivity, magnetism, strength) with their atomic structures.

This "quantum revolution" represents the first major paradigm shift in materials science: the transition from empiricism to rationalism. It became possible to understand how a material would behave before synthesizing it. One of the most powerful tools emerging from this understanding is Density Functional Theory (DFT), developed in the 1960s (Hohenberg, 1964). DFT enables the calculation of fundamental material properties (band gap, bond lengths, phase stability) from its electron density.

For example, we can predict why $SrTiO_3$ behaves as an insulator or why $CsPbI_3$ possesses a high absorption coefficient through DFT calculations before physically synthesizing these materials in the laboratory. This has accelerated the discovery process and significantly reduced costly trial-and-error cycles. However, DFT calculations are computationally intensive and remain impractical for complex systems. This limitation has paved the way for the next revolution: utilizing computational power more intelligently.

3. THE CURRENT PARADIGM: Design through Artificial Intelligence and Machine Learning

Artificial Intelligence (AI) and Machine Learning (ML) have permeated materials science through two fundamental approaches: prediction and design.

3.1 Data-Driven Discovery and Prediction: Initiatives such as the Materials Project, AFLOWLIB, and OQMD have established extensive open-access databases containing properties of hundreds of thousands of materials calculated using Density Functional Theory (DFT) (Jain, 2013). ML models can leverage these databases to predict properties of novel materials within seconds, without performing additional computations. For example, when searching for a new semiconductor with a specific bandgap and stability, an ML model can screen the database to identify the most promising candidates. This process is analogous to using a search engine with keywords rather than manually searching for a book in a library.

3.2 Inverse Design: This approach represents perhaps the most radical departure from traditional methodology. While conventional methods investigate "What are the properties of this material?", inverse design addresses the question "What material configuration is required to achieve these target properties?" (Long, 2022). Researchers define desired characteristics—such as absorption spectrum, bandgap, and stability criteria for an ideal photovoltaic material. The ML model (typically employing architectures like Generative Adversarial Networks - GANs or Variational Autoencoders - VAEs) subsequently proposes novel chemical formulas and structural configurations that satisfy these constraints, including previously unsynthesized compositions.

The $CsPbI_3$ perovskite system serves as a paradigm for these methodologies. While demonstrating near-ideal solar radiation absorption characteristics, this material suffers from thermodynamic instability. ML models have been implemented to propose novel "mixed perovskite" candidates through partial substitution of cesium (Cs) or lead (Pb) sites with alternative elements (e.g., formamidinium organic cations), thereby enhancing stability while preserving optoelectronic efficiency (Hu, 2023). Similarly, in $SrTiO_3$-based systems, ML-driven

analyses are being employed to optimize surface chemistry and interface properties.

4. CASE STUDIES AND APPLICATION DOMAINS: Tangible Evidence of the Paradigm Shift

AI and computational methods have evolved beyond abstract concepts, triggering groundbreaking advances across numerous sub-fields of materials science. The manifestations of this transformation across different application domains are examined below.

4.1. Smart Materials: Optimization of Shape Memory Alloys

Shape memory alloys (SMAs) are "smart" materials capable of reverting to a predefined shape following an external stimulus. Although conventional alloys such as Cu-Al-Be and Ti-V-Mo-Al have been used for years in actuator and sensor applications, they present challenges including precise transformation temperature control, fatigue life, and ductility enhancement. Magnetic shape memory alloys like NiFeGa offer significant advantages due to their magnetic field controllability, but face issues with phase stability and cost. AI-based models are used to simulate thousands of different compositions within these alloy families, thereby identifying new candidate alloys with tailored transformation temperatures, high fatigue resistance, and optimized cost (Yang, 2025).

4.2. Energy Solutions: Next-Generation Photovoltaics and Hydrogen Storage

Energy technologies represent one of the most impactful domains for AI. Halide perovskites such as $CH_3NH_3PbY_3$ (Y= I, Br, Cl) have created a remarkable leap in solar cell efficiency, yet

stability and lead toxicity issues remain the most significant obstacles to practical applications. AI is employed to discover lead-free and stable alternatives; for instance, the optoelectronic properties and stability of compositions like $CH_3NH_3SnI_3$ or $CH_3NH_3BiI_3$ are predicted, thereby accelerating laboratory experimentation (Hu, 2023; Soykan, 2019). Similarly, complex hydrides like Rb_2SnH_4 show promise for safe and efficient storage, which is a fundamental challenge for the hydrogen economy. The hydrogen adsorption/desorption thermodynamics and kinetics of these materials are elucidated through AI-assisted simulations, accelerating the discovery of new hydride compounds with higher energy storage capacity (Allal, 2025).

4.3. Advanced Functional Materials: Optics and Coatings

Boron-based materials like MgF_2B are of significant interest for advanced optical applications due to their combination of high refractive index, low dispersion, and excellent mechanical durability. Such materials are critical for laser systems, protective coatings, and high-quality lenses. While identifying a material that achieves this triple balance (refractive index/dispersion/durability) has been extremely challenging using traditional methods, AI can screen databases of thousands of oxide, fluoride, and boride compounds to identify the most promising candidates possessing these properties, thereby focusing experimental efforts most efficiently (Han, 2025; Kaya Soykan, 2023).

5. THE FUTURE HORIZON: Autonomous Laboratories and Digital Twins

The success of AI in the prediction and design phases has inevitably ushered in the next step: autonomous discovery. These systems, termed "autonomous laboratories" or "materials

acceleration platforms," operate the entire discovery cycle without any human intervention.

These systems function through a four-stage iterative cycle (MacLeod, 2020):

1. Planning: An AI algorithm plans synthesis strategies to achieve a target material property.
2. Synthesis: Robotic systems physically execute this plan (e.g., via solid-state reactions, sol-gel methods).
3. Characterization: Automated characterization tools (e.g., X-ray diffraction, electron microscopy) analyze the synthesized material.
4. Feedback and Learning: The resulting data feeds back into the AI model. The model learns from both successes and failures, thereby refining its hypotheses for the subsequent experiment.

This cycle can condense traditional processes, which typically span weeks or months, into days or even hours. This represents the automation of the scientific method itself. Consequently, the researcher's role evolves from conducting experiments to formulating the right questions and guiding the autonomous system.

In parallel with these physical systems, the concept of the "digital twin" is gaining considerable prominence. A material's digital twin is a virtual representation wherein all its physical, chemical, and mechanical properties are simulated using trained AI models that operate at speeds far exceeding those of DFT. This digital counterpart enables thousands of virtual experiments—those that are impossible or hazardous in the real world, such as extreme temperature/pressure tests or radiation damage assessments—to be conducted. This capability is revolutionary not only for the discovery of new materials but also for predicting

the service life of existing materials deployed in critical applications like nuclear reactors or spacecraft.

6. CONCLUSION AND ETHICAL CONSIDERATIONS: The New Role of Humanity

This extraordinary transformation in materials science brings profound philosophical and ethical questions to the forefront. Our journey, which began with materials like $SrTiO_3$ and $CsPbI_3$, leads us to the very foundations of how humanity produces and applies knowledge.

- Intellectual Property: When a material is designed by an AI and synthesized by a robotic system, who holds the patent rights? Does ownership belong to the creator of the algorithm, the institution that provided the data, or the human researcher who initiated the process? This presents a significant challenge to current patent law frameworks.
- Velocity and Control: Autonomous systems can rapidly discover materials possessing potentially hazardous properties (e.g., highly explosive or toxic compounds). A critical question arises: what occurs when the pace of scientific discovery surpasses the capacity for thorough ethical and safety evaluation? The establishment of new safety protocols and dedicated advisory bodies is imperative for such research domains.
- The Evolving Role of the Researcher: The future materials scientist will transition from a lab technician role to that of a "data steward," an "algorithm curator," and an "ethics auditor." The paramount skill will shift from executing technical procedures to formulating

precise inquiries, effectively training AI systems, and critically interpreting their outputs.

In conclusion, materials science stands at its most thrilling, and perhaps most formidable, juncture in history. Artificial intelligence and autonomous systems are propelling us from merely studying a material's chemical formula to actively designing and optimizing the very process of discovery itself. This signifies more than just the development of superior batteries or more efficient solar cells; it represents a deeper narrative about the convergence of human creativity and machine intelligence to redefine the boundaries of the physical world. The future will be characterized not by the materials themselves, but by the continual reinvention of our fundamental mindset toward them.

REFERENCES

Aghanim, N., Akrami, Y., Ashdown, M., Aumont, J., Baccigalupi, C., Ballardini, M., Zonca, A. (2020). Planck2018 results: VI. Cosmological parameters. *Astronomy & Astrophysics, 641*, A6. doi:10.1051/0004-6361/201833910

Allal, Z., Noura, H. N., Salman, O., Vernier, F., & Chahine, K. (2025). A review on machine learning applications in hydrogen energy systems. *International Journal of Thermofluids, 26*, 101119. doi:https://doi.org/10.1016/j.ijft.2025.101119

Eddington, A. S. (1920). The internal constitution of the stars. *Nature, 106*(2653), 14-20. Retrieved from https://scispace.com/pdf/the-internal-constitution-of-the-stars-4vj4k3qquh.pdf

Gómez-bombarelli, R., Aguilera-iparraguirre, J., Hirzel, T. D., Duvenaud, D., Maclaurin, D., Blood-forsythe, M. A., Aspuru-guzik, A. (2016). Design of efficient molecular organic light-emitting diodes by a high-throughput virtual screening and experimental approach. *Nature Materials, 15*(10), 1120-1127. doi:https://doi.org/10.1038/nmat4717

Han, M., Joung, J. F., Jeong, M., Choi, D. H., & Park, S. (2025). Generative Deep Learning-Based Efficient Design of Organic Molecules with Tailored Properties. *ACS Central Science, 11*(2), 219-227. doi:10.1021/acscentsci.4c00656

Hohenberg, P., & Kohn, W. (1964). Inhomogeneous Electron Gas. *Physical Review, 136*(3B), B864-B871. doi:10.1103/PhysRev.136.B864

Hu, W., & Zhang, L. (2023). High-throughput calculation and machine learning of two-dimensional halide perovskite materials: Formation energy and band gap. *Materials*

Today Communications, 35, 105841. doi:https://doi.org/10.1016/j.mtcomm.2023.105841

Jain, A., Ong, S. P., Hautier, G., Chen, W., Richards, W. D., Dacek, S., . . . Persson, K. A. (2013). Commentary: The Materials Project: A materials genome approach to accelerating materials innovation. *APL Materials, 1*(1). doi:10.1063/1.4812323

Kaya Soykan, F., & Soykan, C. (2023). First-principles study on Boron-doped MgF2−xBx (x=0.0 and 1.0) and F defected MgF1 for anti-reflective coatings in spectacle lenses. *Results in Surfaces and Interfaces, 12*, 100126. doi:https://doi.org/10.1016/j.rsurfi.2023.100126

Long, T., Zhang, Y., Fortunato, N. M., Shen, C., Dai, M., & Zhang, H. (2022). Inverse design of crystal structures for multicomponent systems. *Acta Materialia, 231*, 117898. doi:https://doi.org/10.1016/j.actamat.2022.117898

MacLeod, B. P., Parlane, F. G. L., Morrissey, T. D., Häse, F., Roch, L. M., Dettelbach, K. E., Berlinguette, C. P. (2020). Self-driving laboratory for accelerated discovery of thin-film materials. *Science Advances, 6*(20), eaaz8867. doi:doi:10.1126/sciadv.aaz8867

Ryden, B. (2006). *Introduction to Cosmology*. The Ohio State University, Retrieved from https://assa.saao.ac.za/wp-content/uploads/sites/23/2018/08/Ryden_IntroCosmo.pdf

Soykan, C. (2019). A Study on the Physical Properties of the Newly Calculated Phases of Cu–Al–Be Alloys by ab initio Calculations. *Acta Physica Polonica A, 136*(3), 411-423. Retrieved from http://przyrbwn.icm.edu.pl/APP/PDF/136/app136z3p06.pdf

Soykan, C. (2020). A theoretical approach to the structural, elastic and electronic properties of Ti8−xV4−yMox+y+zAl4−z lightweight shape memory alloys for biomaterial implant applications. *Physica B: Condensed Matter, 598*, 412416. doi:https://doi.org/10.1016/j.physb.2020.412416

Soykan, C., & Gocmez, H. (2019). The physical properties of bismuth replacement in lead halogen perovskite solar cells: CH3NH3Pb1−xBixI3 compounds by ab-initio calculations. *Results in Physics, 13*, 102278. doi:https://doi.org/10.1016/j.rinp.2019.102278

Soykan, C., & Kürkçü, C. (2025). First-principles calculations to investigate structural, electronic, mechanical, optical, vibrational, thermal properties, and hydrogen storage capabilities of Rb2SnH4 for hydrogen storage applications. *Journal of Physics and Chemistry of Solids, 200*, 112618. doi:https://doi.org/10.1016/j.jpcs.2025.112618

Soykan, C., Özdemir Kart, S., Sevik, C., & Çağın, T. (2014). Ab initio calculations of martensitic phase behavior in Ni2FeGa magnetic shape memory alloys. *Journal of Alloys and Compounds, 611*, 225-234. doi:https://doi.org/10.1016/j.jallcom.2014.05.042

Yang, X., Wang, Z., Li, H., Liang, S., Zhang, Z., Yan, X., & Li, Y. (2025). Accelerated discovery of Al-Zn-Mg-Cu alloys with high-strength and high-plasticity by machine learning. *Computational Materials Science, 258*, 114121. doi:https://doi.org/10.1016/j.commatsci.2025.114121

VERMICULITE: CHEMICAL, PHYSICAL PROPERTIES AND APPLICATIONS

Osman Hulusi ÖREN[1]

1. INTRODUCTION

Vermiculite is a 2:1 phyllosilicate mineral group composed of hydrated magnesium–aluminum–iron sheet silicates that contain water molecules within their layered structure (Grim, 1953). The term vermiculite originates from the Latin word vermicularis (meaning “little worm”), referring to the curved and convoluted appearance of the mineral when it is rapidly heated to high temperatures. Natural vermiculite is formed through the hydrothermal alteration and long-term decomposition of phlogopite. Vermiculite possesses a lower layer charge compared to mica and contains hydrated, exchangeable cations in its interlayer spaces. In contrast, the interlayer regions of mica are occupied by non-exchangeable K^+ ions (Rashad, 2016).

Vermiculites can occur in both macroscopic and clay-sized forms. Macroscopic vermiculites are typically trioctahedral in composition, whereas clay-sized vermiculites may be either dioctahedral or trioctahedral and are commonly found in soil environments. Clay-sized vermiculites in soils are often mixed with other clay minerals; therefore, their identification is challenging and requires detailed investigations employing multiple analytical techniques (Rashad, 2016).

The structure, crystal chemistry, mineralogy, and surface chemistry of vermiculites form the basis of their significant roles

[1] Asst. Prof. Dr., Sirnak University, Faculty of Engineering, Department of Civil Engineering, ORCID: 0000-0001-7601-5549.

in natural environments as well as their value in environmental and industrial applications. For instance, vermiculite plays a crucial role in regulating plant nutrient dynamics and mineral transformations in soils through processes such as the retention of K^+ and NH_4^+ ions, hydroxymetal interlayering, and acting as a source or sink for various elements (Wang, et al.,2022).

When vermiculite is rapidly heated above 600 °C, the interlayer water evaporates, generating internal pressure within the structure. This pressure causes the separation of the silicate layers, producing an accordion-like morphology, and leading to the formation of expanded vermiculite. As a result of this process, the material's volume increases more than eightfold, and its lamellar structure becomes flake-like (Li, et al., 2021).

Expanded vermiculite exhibits low density, high thermal and acoustic insulation performance, and a porous, layered morphology that classifies it as a lightweight insulating material. Furthermore, due to its high cation-exchange capacity, vermiculite is effectively used for the removal of heavy metal ions from aqueous environments. Its non-toxic nature, high absorption capacity, and water insolubility make it a favorable material for various industrial and environmental applications, including water purification, agriculture, construction, and insulation (Mysore, Viraraghavan, and Jin, 2005). Similarly, its highly porous structure enables its widespread use as an efficient thermal and acoustic insulation material (Mouzdahir, et al., 2009).

The main objectives of this chapter can be summarized as follows:

(i) to introduce the reader to the structure, mineralogy, and the physical and chemical properties of vermiculite;

(ii) to explain the production process and key characteristics of expanded vermiculite; and

(iii) to present the major fields of application of vermiculite and expanded vermiculite both worldwide and in Turkey.

2. PROPERTIES OF VERMICULITE

2.1. Physical properties

Vermiculite possesses a well-ordered monoclinic crystal structure. Although it commonly exhibits shades of yellow and brown, it may also occur in green or black varieties. The bulk density of raw vermiculite can be reduced from 640–1120 kg/m³ to 64–160 kg/m³ through expansion, depending on the heating duration, temperature, and the efficiency of the furnace used (Kogel, et al., 2006).

The degree of expansion varies according to the mineralogical composition and mica structure of the vermiculite. When rapidly heated in a furnace, vermiculite acquires an accordion- or worm-like morphology. Its hardness ranges from 1.2 to 2 on the Mohs scale. Expansion occurs as a result of the sudden vaporization of interlayer water, which generates vapor pressure that separates the silicate layers, causing them to expand (Li, et al., 2021).Following expansion, vermiculite can reach up to 30 times its original volume. The resulting material is lightweight, low in density, chemically inert, and exhibits superior thermal and acoustic insulation properties (Sutcu, 2015). Variations in expansion and physical behavior depend on the mineral’s biotite or phlogopite origin, the strength of interlayer bonding, the hydration state of interlayer ions, and the conditions of thermal treatment

Vermiculite is classified according to its various physical and chemical properties to determine quality grades, which may vary depending on national standards. In Turkey, vermiculite is

categorized based on particle size and distribution. Raw vermiculite is characterized by five different size grades: micron, super fine, fine, medium, and coarse (Wang, et al.,2022).

The particle size, bulk density, and surface area of raw and expanded vermiculite are presented in Table 2.20. The particle size of raw vermiculite ranges from 0.25 to 8.00 mm. As indicated in Table 1, the bulk density decreases from approximately 1050 kg/m³ for raw vermiculite to 160 kg/m³ for expanded vermiculite. These data are based on the standards established by The Vermiculite Association (2011).

One of the most important physical characteristics of vermiculite is its expansion capacity and interlayer porosity. As the expansion rate increases, the bulk density value decreases. A lower bulk density value indicates a more porous structure, which corresponds to higher material quality.

Table 1. Physical Properties of Vermiculite with Different Particle Sizes (The Vermiculite Association, 2011)

Particle Grade	Raw Vermiculite Particle Size (mm)	Raw Vermiculite Bulk Density (kg/m³)	Expanded Vermiculite Bulk Density (kg/m³)	Specific Surface Area (m²/g)
Micron	0.250–0.710	700–850	90–160	6.4
Very Fine	0.355–1.000	800–950	80–144	5.4
Fine	0.710–2.000	850–1050	75–112	4.4
Medium Fine	1.40–4.00	850–1050	72–90	4.0
Coarse	2.80–8.00	850–1050	64–85	3.8

2.2. Chemical properties and structure

Most of the current knowledge about vermiculite has been derived from studies on the structure of trioctahedral vermiculites. The crystals of these macroscopic vermiculites are granular in form and exhibit a high degree of crystallinity. Consequently, structural analyses performed on these

vermiculites provide more detailed and reliable results compared to other vermiculite types. The layers within the vermiculite structure closely resemble those found in macroscopic mica minerals. Because other types of vermiculite consist mainly of very fine particles and are typically intergrown with other minerals, it is difficult to determine their structures through single-crystal analysis. Consequently, there is limited information that clearly defines the structure of dioctahedral vermiculites on their own. Since these minerals are commonly associated with potassium-deficient muscovites, it is generally assumed that their structural characteristics are similar to those of muscovite (Suvorov and Skurikhin,2003).

The formation of layer charges, i.e., negative charges, in vermiculite results from the isomorphic substitution between Si and Al ions. The layer charge of vermiculite ranges from 0.6 to 0.9 and is balanced by Mg^{2+} and Ca^{2+} cations located within the interlayer spaces. In terms of negative charge density, vermiculite occupies an intermediate position between smectites and micas, but its swelling and expansion behavior make it structurally more similar to smectites. Although vermiculite resembles chlorites in terms of the amount of interlayer cations, the concentration of these cations in vermiculite is approximately 90% lower (Rabello, et al., 2021). The mineral vermiculite primarily originates from the mica group, mainly composed of biotite and phlogopite. Vermiculite forms through the hydration of biotite and phlogopite under the influence of hydrothermal fluids. In mica minerals, which possess strong bonds within their crystal lattice, cation exchange allows water molecules to penetrate between the layers, leading to atomic rearrangements and the formation of the vermiculite structure (Bergaya and Lagaly, 2013). During this process, interlayer K^{+} ions are replaced by Mg^{2+} ions or combinations thereof. The deficiency of positive charge in vermiculite results from the substitution of Si atoms by Al and Fe

within the tetrahedral sheets. This charge imbalance is compensated by interlayer cations. The resulting charge deficiency contributes to the high adsorption capacity of vermiculite.

Structural changes that occur to balance this charge lead to weaker interlayer bonds. These weak bonds break under thermal stress when interlayer water evaporates rapidly, causing the structure to expand and assume an accordion-like morphology. Due to this characteristic, vermiculite is considered an interesting material from a catalytic perspective. Upon the completion of its hydrothermal formation, the cations occupying the interlayer spaces play a critical role in determining the physical and chemical properties of vermiculite (Kogel et al., 2006). The structural diagram of expanded vermiculite is presented in Figure 1.

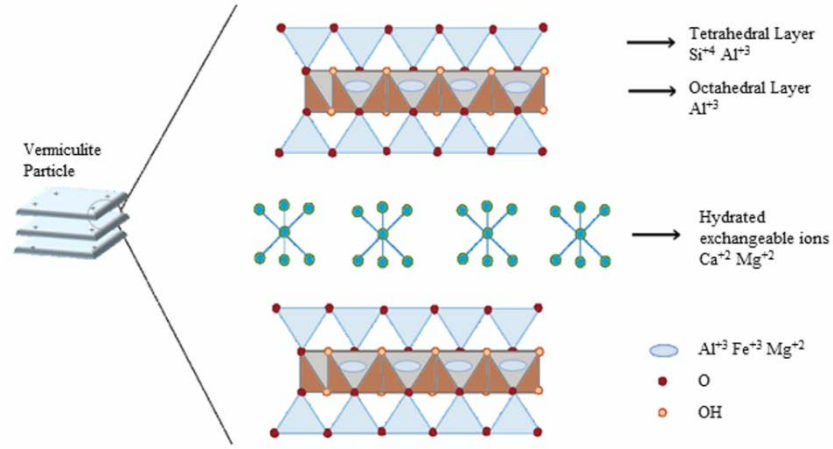

Figure 1. Crystal Structure of the Vermiculite Mineral (Li, et al., 2021).

The chemical composition of vermiculite obtained from different mining locations around the world is presented in Table 2.

Table 2. Chemical Compositions of Vermiculite from Different Countries Worldwide (The Vermiculite Association, 2011)

Mine	SiO_2	TiO	Al_2O_3	Fe_2O_3	FeO	MnO	MgO	CaO
Madagascar	44.50	0.69	14.70	2.69	-	0.07	33.7	-
Colombia	45.40	0.73	13.06	6.91	1.24	0.11	24.1	2.88
Palabora	38.00	1.12	9.46	2.94	-	-	27.9	0.74
Brazil	40.67	0.79	11.51	-	6.69	0.04	25.48	0.03
West China	43.22	1.01	11.87	-	9.58	0.08	18.05	0.4
East China	36.61	1.16	13.91	-	14.29	0.12	14.75	0.12
Egpty	39.15	1.21	12.20	1.54	9.36	-	22.06	0.71
Turkey	39.94	1.13	9.27	-	4.28	0.01	24.27	0.2

An examination of Table 2. reveals that, although vermiculite samples collected from different regions of the world contain similar chemical components, the proportions of these constituents vary. These variations are primarily attributed to differences in the geological conditions and formation environments of the deposits, as well as structural variations within the parent mica group (Bergaya and Lagaly, 2013).

2.3. Dehydration of water in vermiculite structure

The expansion behavior of vermiculite depends on its interlayer water retention capacity and the cation exchange processes occurring between these layers (Bergaya and Lagaly, 2013; Mouzdahir et al., 2009; Zhao et al., 2010). However, the thermal expansion characteristics of vermiculite have not yet been fully clarified. The main reason for this is that vermiculite samples with similar water content exhibit different expansion ratios. Thermal treatment of vermiculite samples from various geological sources around the world has shown that expansion can vary between 10-fold and 30-fold. Generally, hydration is thought to depend on interlayer water content, temperature, and relative humidity (Harraz and Hamdy, 2010). It remains uncertain whether thermal and chemical exfoliation processes share common mechanical factors.

There are three main hypotheses regarding the mechanism of exfoliation: (i) expansion induced by sudden heating, (ii) the effect of particle size, and (iii) the greater expansion observed in mica–vermiculite mixtures compared to pure vermiculite. According to the first hypothesis, slow heating does not cause expansion. The second suggests that smaller particles exhibit lower expansion rates, while the third emphasizes that vermiculites containing mica layers expand more readily than pure ones (Li, et.al., 2021).

The nature of interlayer cations also plays a crucial role in water retention and expansion behavior. Since different cations possess distinct hydrated ionic radii, the structure of exchangeable interlayer cations significantly influences the state of interlayer water. Proton nuclear magnetic resonance (^{1}H NMR) spectroscopy studies have shown that Ca-V and Mg-V vermiculites contain the highest water content (Sanz, Herrero, and Serratosa, 2006). Because the rotational time of interlayer water depends on its content, the mobility of water is controlled by the amount of interlayer spacing. Consequently, Ca-V exhibits greater expansion capability due to its higher water content (Sanz et al., 2006).

The dehydration of water within the vermiculite structure is typically determined by thermogravimetric (TGA/DTA) analysis. The temperature required for dehydration varies depending on the mineral composition (Grim, 1953). When heated to 115–120 °C, vermiculite loses its physically adsorbed water. As the temperature increases to 300 °C, water bound by Van der Waals forces is released from the interlayers. At around 600 °C, chemically bound water begins to decompose, leading to expansion of the structure. This dehydration process continues up to approximately 850 °C, by which point the hydroxyl water is almost completely removed.

If heating occurs gradually, the water vapor between the layers cannot generate sufficient pressure for expansion. Therefore, exfoliation is typically achieved by rapid heating (Mouzdahir et al., 2009). Additionally, the onset temperature of expansion can be reduced through Na^+ and NH_4^+ cation exchange (Huo, et al., 2012).

3. VERMICULITE RESERVES IN THE WORD AND TURKEY

The major vermiculite deposits worldwide are located in the United States (USA), South Africa, Zimbabwe, Russia, Australia, China, and Brazil. Although the total global vermiculite reserves are not precisely known, they are estimated to be approximately 60 million tonnes. The USA, which holds about half of the world's total reserves, ranks second globally in production. Approximately 40% of the world's vermiculite reserves are found in South Africa. The Palabora deposit in South Africa represents the world's largest known vermiculite reserve, making the country second in reserves but first in global production.

Over the past five years, a significant increase has been observed in global vermiculite production. The USA, which previously produced around 100,000 tonnes annually, increased its output to 200,000 tonnes by 2019, representing a 100% growth. South Africa, which maintained the leading position for many years with an annual production of about 160,000 tonnes, fell to second place behind the USA in 2019. Brazil follows these two countries, with a production level approaching 70,000 tonnes per year (World Mineral Production, British Geological Survey [WMPBGS], 2020). Argentina ceased vermiculite production after 2016, while Egypt, which produced nearly 10,000 tonnes annually, halted its operations after 2015 due to internal

instability. In contrast, Turkey and Russia have increased their vermiculite production approximately sixfold over the last five years. Overall, global annual vermiculite production is estimated at around 531,000 tonnes (WMPBGS, 2020). Table 3. presents data on worldwide vermiculite production between 2015 and 2019 (WMPBGS, 2020).

Table 3. Vermiculite Production by Country, 2015–2019 (tons) (WMPBGS, 2020)

Country	2015	2016	2017	2018	2019
Bulgaria	10000	10000	10000	10000	10000
Russia	8282	12363	9262	25904	29266
Turkey	425	1050	1618	18183	18000
Egypt	8190	-	-	-	-
Kenya	410	410	400	400	400
South Africa	138290	166483	166084	141346	158013
Uganda	801	3295	4119	10413	9674
Zimbabwe	30868	29020	23302	33161	30000
Mexico	299	310	464	244	240
ABD	100000	100000	100000	100000	200000
Argentina	90	60	-	-	-
Brazil	70000	55000	55000	50000	60000
China	15000	15000	15000	15000	15000
India	23279	9042	6054	3161	2960

Geological investigations conducted in Turkey have revealed the presence of vermiculite formations within the ophiolitic belts of the Sivas and Elazığ regions (Toksoy-Köksal, Türkmenoğlu, & Göncüoğlu, 2001). Significant vermiculite deposits have also been identified in the Malatya–Darende, Sivas–Yıldızeli, Eskişehir–Sarıcakaya, and Elazığ–Harput areas (DPT, 2019). The total vermiculite reserves in Turkey are estimated to be approximately 6–7 million tonnes (Toksoy-Köksal et al., 2001).

The largest known vermiculite deposit in Turkey is located in the Sivas–Yıldızeli region. According to investigations conducted by the General Directorate of Mineral Research and Exploration (MTA), the area hosts approximately 2.75 million

tonnes of vermiculite with high expansion capacity and 2.475 million tonnes of lower-expansion raw vermiculite. Laboratory analyses of samples obtained from this deposit revealed that the material exhibits an expansion ratio between 13 and 18 times and is classified as second-grade vermiculite based on bulk density.

Exploration activities carried out by licensed operators have expanded the known boundaries of the deposits, and as of 2020, Turkey's identified vermiculite reserves have reached approximately 35 million tonnes, as reported by the operating companies (MTA, 2019). In the Sivas–Karakoç vermiculite deposits, the operating company extracts primarily medium- and coarse-grained material, with an annual production of about 20,000 tonnes of raw vermiculite. According to World Mineral Production, British Geological Survey (WMPBGS, 2020), Turkey increased its vermiculite production from 425 tonnes in 2015 to 18,000 tonnes in 2019. The General Directorate of Mining and Petroleum Affairs (MAPEG, 2020) provides detailed data on Turkey's annual vermiculite production in Table 4.

Table 4. Vermiculite Production in Turkey between 2018–2020. (MAPEG, 2020).

Year	Production Volume (tons)
2018	15042
2019	21083
2020	19230

4. EXPANDED VERMICULITE

4.1. Production method of expanded vermiculite

The expansion of vermiculite is achieved by two main methods: chemical expansion and thermal (heating) expansion. Among these, thermal heating is the most traditional and widely used technique on an industrial scale. In the chemical expansion process, hydrogen peroxide, weak acids, and electrolyte solutions

are typically employed (The Vermiculite Association, 2011). Because vermiculite deposits are generally located near the surface, the mineral is commercially extracted using open-pit mining techniques. The raw vermiculite ore obtained from the mine first undergoes ore beneficiation, and the upgraded ore is then subjected to the expansion process. Initially, the raw vermiculite is crushed and then sieved to classify it according to particle size (Toksoy-Köksal et al., 2001). The classified material must be stored in dry, closed facilities, since vermiculite is a hygroscopic material. Improper storage conditions allow the mineral to absorb moisture from the air, which increases its internal water content and consequently raises both the energy requirements and the production cost during expansion.

The thermal heating method is the primary industrial approach for vermiculite expansion. In this process, vertical, inclined, rotary, and fluidized-bed furnaces are used, with vertical furnaces being the most common. The raw vermiculite is transferred from storage to the furnace via a conveyor system, and the furnace interior is lined with heat-resistant refractory bricks. Inside the furnace, the vermiculite is exposed to temperatures between 850 °C and 1100 °C for approximately 4–8 seconds. Under these conditions, the interlayer water vaporizes rapidly, generating internal pressure that causes the vermiculite to expand (exfoliate). The expanded material is then quickly removed from the furnace by means of a high-capacity fan system (Kogel et al., 2006; Toksoy-Köksal et al., 2001).

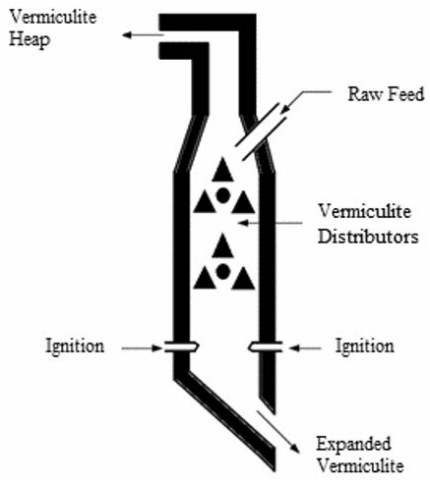

Figure 2. Production of Expanded Vermiculite by Thermal Heating

In the chemical expansion method, various chemical agents are used to enable vermiculite to expand perpendicular to its interlayer planes at temperatures below 100 °C. These agents include hydrogen peroxide (H_2O_2) solution, sulfuric acid (H_2SO_4), nitric acid (HNO_3), hydrochloric acid (HCl), and phosphoric acid (H_3PO_4).

Among these, the hydrogen peroxide (H_2O_2) solution has been identified as the most effective agent in terms of expansion efficiency. The expansion mechanism with hydrogen peroxide is based on its decomposition into H_2O and O_2 gases within the interlayer voids of vermiculite. The released gases disrupt the cationic balance between adjacent layers, causing the layers to separate and resulting in the expansion of the mineral (Huo et al., 2012; Kehal, et al., 2010; Obut and Girgin, 2002).

However, the chemical expansion method has certain limitations. Due to its prolonged reaction time and the high consumption of chemical reagents, it is not suitable for large-scale industrial applications.

4.2. Applications of expanded vermiculite

Expanded vermiculite has become a versatile industrial material due to its lightweight nature, excellent thermal and acoustic insulation, and chemical inertness. For this reason, the raw form of vermiculite is rarely used directly, and its expanded form is generally preferred.

Until the first half of the 20th century, expanded vermiculite was primarily utilized as a filler and insulation material in the construction industry. However, during the second half of the century, with the advancement of research on its structural, chemical, and physical properties, its use expanded into various other fields (Toksoy-Köksal et al., 2001).

Today, expanded vermiculite is widely used in construction, industrial production, agriculture, insulation, packaging, chemical applications, and environmental technologies. The various application areas and types of vermiculite are presented in Table 5., while its uses based on particle size are shown in Table 6. The distribution of vermiculite applications across sectors is illustrated in Figure 3.(USGS, 2019).

Table 5. Applications of expanded vermiculite in different sectors

Sector	Application Area	Sector	Application Area
Construction Sector	Air-hardening binder	**Industrial Sector**	Brake linings
	Plaster and rendering materials		Industrial furnaces
	Flooring and ceiling systems		Drilling mud formulations
	Vermiculite boards		Paints and coatings
	Acoustic and thermal insulation		Insulating materials
Agricultural Sector	Organic fertilizer	**Agricultural Sector**	Pesticides
	Anti-caking agent		Animal feed additive
	Soil conditioner		Potting mixtures
	Seed germination medium		Bulking agent
	Soil aeration improver		Fertilizer additive

Table 6. Usage areas of expanded vermiculite according to particle size

Particle Size (mm)	Application Area
12.5 – 0.74	Insulation materials, acoustic plasters, coatings, and cements
0.74 – 0.37	Insulation materials for refrigerators and vehicles, fire extinguisher filters, and storage tanks
0.37 – 0.12	Linoleum and roofing materials
0.12 – 0.074	Engine oils and plastics
0.074 – 0.054	Wallpaper and exterior paints

The particle size of expanded vermiculite significantly influences its physical properties and application areas. Coarser particles (12.5–0.74 mm) are primarily used in construction as insulation and coating materials, while medium-sized fractions (0.74–0.37 mm) are preferred in thermal insulation systems for appliances and vehicles. Finer particles (below 0.12 mm) are commonly utilized in chemical formulations such as lubricants, plastics, and paints due to their high surface area and adsorption capacity.

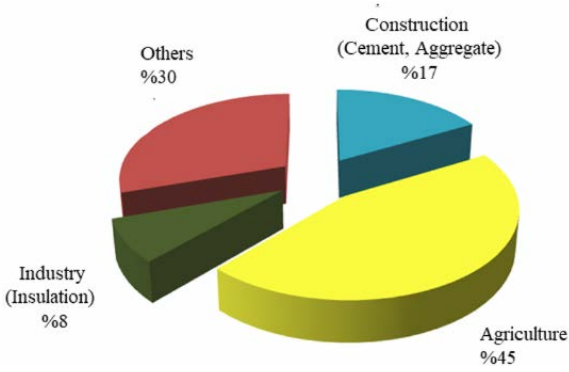

Figure 3. Usage ratio of expanded vermiculite by sector (USGS, 2019).

5. SUMMARY

Vermiculite is widely found in the United States, China, Russia, South Africa, Australia, and Brazil, in Turkey it has been

identified only in the Sivas region and its surroundings. Despite its broad global occurrence, vermiculite is not considered one of the major mineral types commonly found in soils. Nevertheless, due to its structural and chemical characteristics, vermiculite plays a significant role in numerous geochemical reactions occurring in rocks. Its unique structural and chemical features, generally inert behavior, and non-toxic nature make it a valuable material for industrial applications. In particular, in its expanded form, the large interlayer voids within its structure provide excellent insulation and make it a key raw material in the production of sustainable products.

The NH_4^+ and K^+ ions present within the structure of vermiculite contribute to effective soil aeration, thereby broadening its range of applications in agriculture. With the advancement of nuclear technologies, the disposal of radioactive waste materials has become increasingly important worldwide. The presence of Cs^+ ions within vermiculite makes this mineral a promising material for the immobilization and safe containment of radioactive wastes. Furthermore, due to the continuous expansion of industrial production, vermiculite is also considered a suitable adsorbent and ion-exchange medium for the removal and neutralization of heavy metal cations from waste streams, minimizing their environmental impact.

Vermiculite expands by 10 to 30 times its original volume when heated to 600 °C, depending on its mineralogical structure and chemical composition. This expansion property has enabled vermiculite to find broad applications in both industrial and agricultural sectors. The porous structure formed as a result of exfoliation renders vermiculite a lightweight material with unique thermal insulation characteristics. Its low bulk density and low thermal conductivity make it a valuable raw material for the production of fire-resistant building materials that reduce structural weight and enhance energy efficiency.

The commercial utilization of vermiculite largely depends on a comprehensive understanding of its structural properties and formation mechanisms. Therefore, detailed investigations into the natural formation, physicochemical behavior, and structural characteristics of vermiculite will facilitate its more efficient and widespread use in applications such as waste treatment, agricultural enhancement, and the development of advanced insulating materials.

REFERENCES

Addison, J. (1995). Vermiculite: A Review of The Mineralogy and Health Effects of Vermiculite Exploitation. Regulatory Toxicology and Pharmacology, 21(3), 397-405.

Bergaya, F. and Lagaly, G. (2013). General Introduction: Clays, Clay Minerals, And Clay Science. Developments in Clay Science, 1, 1-18.

Devlet Planlama Teşkilatı Müsteşarlığı (DPT). (2019). T.C. Kalkınma Bakanlığı Devlet Planlama Teşkilatı Müsteşarlığı, 11. Kalkınma Planı Madencilik Özel İhtisas Komisyonu Raporu, https://www.sbb.gov.tr/ozel-ihtisas-komisyonu-raporlari/#1540024439304-a1816e9a-4191

El-Mouzdahir, Y., Elmchaouri, A., Mahboub, R., Gil, A. and Korili, S.A. (2009). Synthesis of Nano-Layered Vermiculite of Low Density by Thermal Treatment. Powder Technology, 189(1), 2-5.

Grim, R.E. (1953). Soil Science, Clay Mineralogy, (1. basım), 317, Newtork: Williams & Wilkins.

Harraz, H.Z. and Hamdy, M.M. (2010). Interstratified Vermiculite-Mica in The Gneiss-Metapelite-Serpentinite Rocks at Hafafit Area, Southern Eastern Desert, Egypt: From Metasomatism to Weathering. Journal of African Earth Sciences, 58, 305-320.

Huo, X., Wu, L., Liao, L., Xia, Z. and Wang, L. (2012). The Effect of Interlayer Cations on The Expansion of Vermiculite. Powder Technology, 224, 241-246.

Kehal, M., Reinert, L. and Duclaux, L. (2010). Characterization and Boron Adsorption Capacity of Vermiculite Modified

by Thermal Shock or H2O2 Reaction and/or Sonication. Applied Clay Science, 48, 561-568.

Kogel, J.E., Trivedi, N.C., Barker, J.M. and Krukowski, S.T. (2006). Industrial Minerals & Rocks: Commodities, Markets, and Uses, 1015-1027, Colorado: Society for Mining, Metallurgy and Exploration.

Li, W., Zhao, Y., Ai, Z., Bai, H., Zhang, T., and Song, S., (2021) Preparation and application of expanded and exfoliated vermiculite: A critical review. Chemical Physics, 550, 111313.

Maden Tetkik ve Arama Genel Müdürlüğü (MTA). (2019). 2019 Faaliyet Raporu, https://www.mta.gov.tr/v3.0/kurumsal/faaliyet-raporlari

Maden ve Petrol İşleri Genel Müdürlüğü (MAPEG). (2020). Maden Üretim Değerleri, https://www.mapeg.gov.tr/Custom/Madenistatistik

Mysore, D., Viraraghavan, T. and Jin, Y.C. (2005). Treatment of Oily Waters Using Vermiculite. Water Research, 39, 2643-2653.

Rabello, L.G. and Conceição Ribeiro, R.C. (2021). A Novel Vermiculite/Vegetable Polyurethane Resin-Composite for Thermal Insulation Eco-Brick Production. Composites Part B: Engineering, 221, 109035, 1-11.

Rashad, A.M., (2016). Vermiculite as a construction material – A short guide for Civil Engineer. Construction and Building Materials, 125, 53-62.

Obut, A. and Girgin, I. (2002). Hydrogen Peroxide Exfoliation of Vermiculite and Phlogopite. Minerals Engineering, 15, 683-687.

Sanz, J., Herrero, C.P. and Serratosa, J.M. (2006). Arrangement and Mobility of Water in Vermiculite Hydrates Followed By 'H NMR Spectroscopy. The Journal of Physical Chemistry B, 110, 7813-7819.

Sutçu, M. (2015). Influence of Expanded Vermiculite on Physical Properties and Thermal Conductivity of Clay Bricks. Ceramics International, 41(2), Part B, 2819-2827.

Suvorov, S.A. and Skurikhin, V.V.(2003). Vermiculite—A Promising Material for High-Temperature Heat Insulators. Refractories and Industrial Ceramics, 44, 186–193.

The Vermiculite Association. (2011). The World of Vermiculite. Hampshire, GU35 9LU, United Kingdom. http://www.vermiculite.org/

Toksoy-Köksal, F., Türkmenoğlu, A.G. and M. Cemal Göncüoğlu, M.C. (2001). Vermiculitization of Phlogopite in Metagabbro, Central Turkey. Clays and Clay Minerals, 49, 81–91.

U.S. Geological Survey, (2019). Mineral Commodity Summaries 2019, Washington: United State Goverment Printing Office.

Wang, S., Gainey, L., Marinelli, J. et al. (2022). Effects of Vermiculite on In-Situ Thermal Behaviour, Microstructure, Physical and Mechanical Properties of Fired Clay Bricks. Construction and Building Materials, 316, 125828, 1-11.

World Mineral Production British Geological Survey (WMPBGS). (2020). World Mineral Production 2015–19, https://www2.bgs.ac.uk/mineralsUK/statistics/worldStatistics.html

Zhao, M., Tongjıang, P., Yongguang, X. and Wei, Y. (2010). Preparation of Expanding Vermiculite by Chemical and Microwave Methods. Advanced Material Research, 96, 155-160.

DETECTION AND MEASUREMENT TECHNIQUES OF RADIATION IN INDUSTRIAL AND ENVIRONMENTAL APPLICATIONS: FUNDAMENTAL PRINCIPLES AND CURRENT APPROACHES

Ahmet TURŞUCU[1]

1. INTRODUCTION

We can cite mass and energy as the two fundamental parameters constituting our universe. These two terms, as defined in this context, manifest in each other's form under varying conditions and temporal contexts. This profound interrelationship is elucidated by the globally recognized formula contributed to science by Einstein: $E = mc^2$.

Analogous to the transport of matter, the propagation of energy between disparate points in space is facilitated by means of both particles and waves. These carrier sources invariably originate from a specific source and sustain their trajectory through space until they are either absorbed or annihilated by another medium.

The requisite term for explaining all these aforementioned phenomena is "Radiation," which holds its established position within the scientific literature. The carrier sources invariably originate from a specific source and sustain their trajectory through space until they are either absorbed or annihilated by another medium. The requisite term for explaining all these

[1] Prof. Dr., Şırnak University, Engineering Faculty, Electric-Electronic Engineering Dep., ORCID: 0000-0002-4963-697X.

aforementioned phenomena is "Radiation," which holds its established position within the scientific literature.

Initially (up until the 1900s), the concept of Radiation had a narrow meaning, encompassing only electromagnetic waves. However, the scope of the definition expanded with discoveries at the turn of the century, such as the electron, X-rays, and natural radioactivity. These new discoveries exhibited particulate characteristics, unlike the wave-based electromagnetic radiation. With the development of quantum physics, particularly De Broglie's theory of matter-wave duality in the 1920s and its confirmation through electron diffraction experiments, the strict distinction between particle and wave was eliminated.

As a result of this evolution, the term radiation has achieved its broadest current meaning, encompassing both the entire electromagnetic spectrum and all known atomic and subatomic particles.

Ever since the possibilities offered by Radiation were discovered, this phenomenon has been central to our technological advancements across numerous fields. For instance, the benefits provided by radiation are widely utilized in modern medicine for both diagnostic and therapeutic processes. Simultaneously, however, humanity has painfully experienced the dangerous aspects of radiation through events like atomic explosions and instances of radiation exposure. Whether we consider radiation a threat or a blessing, its study is of paramount importance for the survival and progress of humanity (Turner, 2007). When we carefully analyze the effects resulting from the correct or incorrect use of radiation, its benefits clearly outweigh the harm. When properly harnessed, radiation possesses limitless potential to open new frontiers for humankind.

In this book chapter, information regarding the types and formation of radiation, its detection, measurement, and industrial applications will be presented to the reader.

2. INTERACTION OF MATTER WITH RADIATION

The answer to the question of how we can measure radiation, which is invisible to our eyes, lies in a fundamental scientific truth: to measure something, we must enable it to leave a trace.

Just as sound waves strike our eardrum and create vibrations that form the perception of hearing, radiation only reveals its existence when it collides with matter and creates a physical or chemical change. For this reason, radiation detectors do not measure the radiation itself, but rather the effect it leaves behind.

Every detector, from the condensation tracks followed by particles in the old cloud chambers which revealed the presence of radon gas to the bright flashes of light in modern scintillation detectors used in airport security screening, records how the radiation transfers its energy to matter (Knoll, 2010).

These modern electronic systems operate using gases, semiconductors, or special crystals. For example, a Geiger counter produces a "click" sound by counting the electrical current generated when radiation enters a gas environment and ionizes the atoms. By collecting the signals released by ionization, these detectors provide detailed information about the radiation's identity, energy, and direction. In short, the secret to designing an effective detector lies in precisely resolving the interaction mechanisms of the invisible phenomenon on matter (Attix, 2008).

However, for these measurements to be meaningful, we require a standard language. Multiple units are used in radiation measurement. The fundamental unit used to express how much radiation a material has absorbed is the Gray (Gy). This unit shows how much energy (Joule) the material has received per kilogram of mass. When we want to measure the potential biological effect on human health, the Sievert (Sv) comes into play. Sievert applies a weighting factor to the Gray value, adjusting it according to the type of radiation. This allows us to compare the potential damage of different types of radiation at the same absorbed dose (ICRP, 2007).

Thus, the raw data collected by our detectors (ionization signals) are ultimately converted into these standard Gray and Sievert units to be interpreted for the sake of our safety and health.

3. BASIC RADIATION DETECTION PRINCIPLES

The detection of radiation fundamentally relies on measuring the secondary effects that arise from the interaction of radiation with matter; this is the indirect characterization of a quantity that cannot be observed directly. When radiation (photons or charged/uncharged particles) enters a sensing medium, it transfers its energy to the atoms of the medium via three main mechanisms: ionization, excitation, radiative loss (Knoll, 2010). An effective detector must be able to sensitively measure the electrical, optical, or chemical change resulting from this energy transfer.

3.1. Basic Radiation Detector Types

Modern detector systems are categorized into three main groups based on the methods used to collect the signal resulting from the interaction of radiation with matter (Knoll, 2010):

Gas Filled Detectors: These detectors collect the electron-ion pairs liberated by the ionization of the gas medium caused by radiation. They operate under different regimes based on the strength of the applied electric field: Ionization Chamber, Proportional Counter, and Geiger-Müller (GM) Counter. They are generally utilized to measure the dose rate of the radiation field and the number of particles.

Scintillation Detectors: These detectors utilize flashes of light emitted when radiation excites the atoms in special crystal or organic materials called scintillators. This emitted light is then converted into an electrical signal via a photomultiplier tube (PMT) (Gershey, 2007). The direct proportionality between the signal amplitude and the radiation energy makes these detectors ideal for gamma spectroscopy.

Semiconductor Detectors: Semiconductor materials, such as High-Purity Germanium (HPGe) or Silicon, collect the electron-hole pairs generated by ionization.

Due to the low energy required for ionization (approximately 3 eV) these detectors possess a significantly higher energy resolution compared to scintillators, making them the preferred choice for nuclear analysis (Ziock & Cooper, 2009).

3.2. Spectrum of Applications

These fundamental detection principles are not limited only to biology and medicine (e.g., PET and SPECT imaging), but are used across a wide spectrum of science and engineering. For example:

- Geophysics and Environmental Sciences: Detection and analysis of natural radioactivity in soil and water resources.

- Physics and Space Sciences: Discovery of new particles in particle accelerator experiments and the study of cosmic rays from space.
- Security and Industrial Applications: Radiation safety monitoring in nuclear power plants and the detection of radioactive contraband at airports.

Therefore, a deep understanding of the radiation-matter interaction mechanisms that form the basis of these detector systems is critically important for making reliable and accurate measurements across a wide range, from scientific research to industrial control.

3.3. Industrial Applications

Radiation detection and measurement techniques play a critical role in improving the efficiency, quality, and safety of industrial processes. Non-contact, high-precision measurement and analysis systems have been developed using the principles of how ionizing radiation emitted by radioisotopes interacts with matter (Knoll, 2010). These applications are generally based on the principle of a source (radioisotope) and detector pair.

3.3.1. Level, Thickness and Density Measurements

One of the most widely used radiometric techniques in industry is based on measuring the attenuation (μ) of radiation passing through a material. Radiation attenuation is related to derivatives of the Beer-Lambert Law and depends on the material's thickness, density, and atomic number.

- Thickness Measurement (Gauging): Especially in continuous production lines (e.g., sheet metal, paper, and plastic film production), the material's thickness is monitored non-contact with a gamma or beta source (e.g., Strontium-90 or Cesium-137). The thicker the material, the less radiation reaching the detector (usually an

ionization chamber or scintillator). This method, integrated with feedback control systems, minimizes production errors.

- Level Measurement: Used for non-contact determination of liquid, powder, or granular material levels in closed tanks or furnaces. The source is mounted on one side of the tank, and the detector on the opposite side. As the level changes, the distance the radiation travels through the material, and therefore the amount of attenuation, changes. This ensures safety and efficiency by preventing overfilling or over-discharging.
- Density Measurement: Attenuation of gamma radiation is used to instantly measure the density of liquids or slurries in pipelines. It is a critical quality control tool in the chemical, mining, and petroleum industries, where concentration monitoring is required.

3.3.2. X-Ray Fluorescence Spectrometry (XRF)

XRF is a spectroscopic technique used to non-destructively analyze the elemental composition of materials. The principle is that when a sample is bombarded with primary x-rays or gamma rays, the atoms in the sample are excited. As the excited atoms return to their ground state, they emit secondary (fluorescence) x-rays with characteristic energy specific to each element.

- Quality Control: XRF is widely used to verify the correct composition of metal alloys, analyze raw materials in cement production, or detect the presence of toxic elements (RoHS compliance) in the electronics industry. Semiconductor detectors (e.g., Silicon Drift Detectors (SDDs) are preferred in these applications because they provide high energy resolution.

3.3.3. Automated Nuclear Assay (Prompt Gamma Neutron Activation Analysis - PGNAA)

PGNAA is an advanced technique used to measure the composition of large volumes of material (coal, cement raw materials, or ore) in real time (Heal & Johnson, 2018).

- Principle: Neutrons emitted from a source (usually a neutron-emitting isotope such as ^{252}Cf) are captured by the atomic nuclei of the sample. This neutron capture process causes the atomic nuclei to become excited and immediately emit "snapshot gamma rays" with characteristic energies. The emitted gamma ray energies are analyzed by high-resolution HPGe detectors to determine the elements contained in the material and their concentrations. This is a vital technique for ore separation in mining and for real-time fuel quality control in coal power plants.

3.3.4. Radiographic Examination (Industrial Radiography)

Similar to medical imaging, industrial radiography uses high-energy x-rays or gamma rays (especially Iridium-192 and Cobalt-60) to non-contactly detect defects in the internal structure of solid materials (weld cracks, voids, and corrosion). This is a fundamental method in non-destructive testing (NDT) to ensure the integrity of pipelines, pressure vessels, and structural components. Modern techniques such as Digital Radiography (DR) and Computed Radiography (CR) have reduced the use of traditional film, allowing for faster image acquisition and processing.

These techniques are essential for ensuring the continued safety and economic efficiency of industrial processes and continue to evolve with continuous advances in radiation physics and detector technology.

3.4. Environmental Applications

Radiation detection and measurement techniques are indispensable for environmental monitoring, pollution analysis, and ecosystem health assessment (Cember & Johnson, 2009). Detecting natural and artificial radioactivity is vital for assessing water, soil, and air quality and identifying potential risks to human health.

3.4.1. Environmental Radioactivity Monitoring and Dosimetry

Environmental dosimetry aims to continuously monitor the changes in ionizing radiation levels in a region over time. This monitoring is fundamental for assessing the environmental impacts of nuclear facilities and understanding natural background radiation (terrestrial and cosmic) (EPA, 2000).

Detection Technology: High-sensitivity Thermoluminescence Dosimeters (TLD) or Optically Stimulated Luminescence (OSL) dosimeters are typically used (Delgado, 2012). These passive detectors store the radiation energy they are exposed to within their crystal structures. After a certain period (e.g., three months), the stored energy is released as a measurable light signal by heating (TLD) or photoexcitation (OSL). This signal accurately reflects the cumulative radiation dose accumulated in the region.

Air Monitoring: Radioactive aerosols and gases (e.g., ^{131}I, ^{137}Cs, ^{40}Ar) in the atmosphere are continuously monitored by filtration and spectroscopic analysis. This typically involves subjecting samples collected with filter collectors to gamma spectroscopy with in-situ HPGe detectors.

3.4.2. Geochronology and Environmental Isotope Analysis

Radioactive decay processes are used as precise "nuclear clocks" to determine the age and dynamics of environmental systems (Wang et al., 1975).

- Radiocarbon Dating: The measurement of the 14C isotope, used to determine the age of organic materials, is a classic example of environmental applications. It is typically performed with Accelerator Mass Spectrometry (AMS). By directly counting the 14C atoms in the sample, AMS allows for more precise results with much smaller sample sizes than traditional counting methods.
- Sedimentation Rates: Isotopes such as lead-210 (^{210}Pb) are used to determine rates of sediment accumulation in lake and seabeds and, therefore, the history of pollution. This is critical for understanding past environmental changes.

3.4.3. Biological Monitoring (Bioindicators) and Ecotoxicity

Radiation detection techniques are a fundamental tool in ecotoxicity studies, which examine the transfer of radionuclides in the ecological chain and their effects on living organisms (IAEA, 2014). Biological materials are used as natural detectors (bioindicators) to monitor the accumulation of environmental radioactivity.

- Bioaccumulation Studies: Plants, lichens, mosses, and aquatic organisms accumulate radionuclides (e.g., 137Cs, 90Sr) in their tissues from the environment. These bioaccumulation rates are important for modeling the movement of radionuclides through the food chain. Collected biological samples are dried, incinerated, and

then analyzed using low-background gamma spectrometry or alpha/beta counting techniques. Such bioaccumulation studies, combined with plant biotechnology applications (Ulgen et al., 2021; Ulgen et al., 2020), contribute to the understanding of the effects of radioactivity at the cellular and genetic levels.

- Radioecology: These studies map radionuclide concentrations in different components of ecosystems (water, soil, plants, animals). These data provide input to Dose Assessment processes to assess the potential effects of radionuclides on living organisms and, ultimately, on humans. Biological monitoring is essential for understanding the distribution of not only artificial radionuclides but also naturally occurring radioactive elements (e.g., the uranium and thorium series). These applications demonstrate the indispensable role radiation detection plays in environmental sustainability and long-term ecological health monitoring.

4. RADIATION SAFETY AND REGULATORY COMPLIANCE

The most critical use of data from environmental applications is to ensure compliance with public and occupational radiation safety standards. Radiation detection and measurement systems not only determine environmental contamination levels but also serve as the primary means of consistently demonstrating compliance with dose limits established by national and international regulatory frameworks (e.g., ICRP 2007, IAEA).

4.1. Dose Assessment and Risk Management

Environmental monitoring programs are essential for assessing radiological risks to humans and biodiversity.

- Exposure Pathway Analysis: Radionuclide concentrations in soil, water, and air are combined with mathematical transfer models to calculate potential human doses across different exposure routes (inhalation, ingestion, external exposure). These calculations integrate accumulated activity levels with dose rate data collected by environmental monitoring devices.
- ALARA Principle Application: The resulting environmental dosimetry data are translated into operational decisions to manage radiation exposure according to the As Low As Reasonably Achievable (ALARA) principle (Cember & Johnson, 2009). For example, if established limits are exceeded, the frequency of environmental sampling is increased or waste management procedures are revised.

4.2. Cross-Border Monitoring and Emergency Preparedness

Because radioactive emissions do not recognize geographical boundaries, radiation detection networks operate on a global scale.

- Early Warning Systems: Real-time detector networks installed in the immediate vicinity of nuclear facilities or unexpected events (accidents, terrorist acts) detect instantaneous dose rate increases and immediately alert national and international authorities. These systems typically operate with high-sensitivity NaI(Tl) scintillation detectors or ionization chambers and transmit data to a central control system.
- Compliance and Reporting: Environmental assessment results are regularly reported to national regulatory bodies and audited as part of environmental management

systems (e.g., ISO 14001). This process is essential for maintaining public confidence and verifying that all relevant regulatory requirements are met.

The subheading "Radiation Safety" emphasizes that detection and measurement techniques are not merely academic or industrial tools but also a fundamental necessity for fulfilling ethical and legal responsibilities.

5. CURRENT APPROACHES AND CONCLUSION

Radiation detection and measurement techniques have served as a critical information technology infrastructure in applications ranging from industrial efficiency to environmental sustainability. The non-contact, non-destructive, and high-precision analysis capabilities of these techniques are essential for modern industrial control and global radiation safety commitments.

5.1. Current Technological Approaches and Trends

Recent technological advances have significantly improved the performance, portability, and cost-effectiveness of radiation detection systems:

1. Advanced Semiconductor Technologies: The development of next-generation semiconductor detectors, such as Cadmium Zinc Telluride (CZT), which do not require cooling, has brought high-energy resolution spectroscopic analysis capabilities to the field. This has increased speed and accuracy in nuclear material identification and field safety applications (Ziock & Cooper, 2009).
2. Integration of Artificial Intelligence (AI) and Machine Learning (ML): ML algorithms are critical for analyzing large and complex data sets. These models

offer the ability to distinguish subtle energy differences between natural background radiation and threatening radionuclides, predict detector failures, and more accurately model radioactive spills in emergency situations.

3. Distributed Radiation Sensor Networks (DRSN): Traditional centralized systems have been replaced by low-power, miniature sensor arrays integrated with wireless networks. These networks enable continuous and cost-effective monitoring of large areas, such as nuclear waste sites and critical infrastructure (Smetana & Dron, 2020).

5.2. Universal Nuclear Energy Development and Radiation Detection

Global energy demand and net-zero carbon targets have redefined the role of nuclear energy. This development creates new challenges and opportunities for radiation detection technologies:

- Detector Requirements in Next-Generation Reactors: Fourth-Generation reactors (WNA, 2021) operate in higher temperature and neutron flux environments. This necessitates the development of new detectors that are resistant to high temperatures and capable of monitoring nuclear fluxes in real time (e.g., miniature high-temperature ionization chambers).
- Small Modular Reactors (SMRs): The potential for SMRs to be located near residential areas has necessitated increasing the density and sensitivity of environmental monitoring networks. To support the passive safety philosophy of SMRs, the integration of on-site and remote, AI-powered environmental monitoring systems has become critical.

- Nuclear Waste Management: Ultra-stable and long-lived environmental radiation sensors are needed to monitor the environmental impact of nuclear waste disposal facilities for tens of thousands of years. These detectors must provide consistent data over long periods without human intervention (OECD, 2019).

6. CONCLUSION

The future of radiation detection techniques will be shaped by the integration of sensor fusion and autonomous decision-making capabilities. As speed and accuracy standards for industrial quality control (XRF, PGNAA) rise, the integration of biological monitoring (bioindicator) data with physical data in environmental monitoring will deepen. Radiation detection systems are no longer simply measurement tools but are positioned as fundamental information technology infrastructures that optimize complex processes, ensure compliance with global regulations, and ensure the reliability of future energy infrastructures. Continuous advances in these technologies will continue to benefit a wide range of areas, from scientific research to global risk management.

Acknowledgments

This work was supported by Şırnak University Research Fund (BAP): [Grant Number 2025.FNAP.06.02.02].

REFERENCES

Attix, F. H. (2008). *Introduction to radiological physics and radiation dosimetry*. Wiley-VCH. (Provides in-depth information on dosimetry and radiological physics.)

Cember, H., & Johnson, T. E. (2009). *Introduction to health physics: Fourth edition*. McGraw-Hill Education. (Covers radiation safety and environmental health physics principles in detail.)

Delgado, A. (2012). Environmental applications of passive radiation detection techniques. *Radiation Measurements, 47*(7), 543–551. (Addresses the use of passive dosimeters like TLD and OSL in environmental monitoring.)

Gershey, R. M. (2007). Advances in scintillation detection. *Journal of Radioanalytical and Nuclear Chemistry, 273*(1), 165–170. (Covers current technological developments and applications in scintillation detectors.)

Heal, J. M., & Johnson, E. L. (2018). The role of prompt gamma neutron activation analysis in modern industrial quality control. *Applied Radiation and Isotopes*, *142*, 19-24. (Presents a scientific analysis of the use of PGNAA in industrial processes.)

International Atomic Energy Agency (IAEA). (2014). *Remediation process for areas affected by past activities and accidents*. (Safety Reports Series No. 78). Vienna: IAEA. (Addresses topics such as the environmental effects of radioactivity and bioaccumulation.)

International Commission on Radiological Protection (ICRP). (2007). *The 2007 recommendations of the International Commission on Radiological Protection* (ICRP Publication 103). Elsevier. (The scientific basis of

radiation safety regulations, which form the foundation of Sievert and Gray units and the ALARA principle.)

Knoll, G. F. (2010). *Radiation detection and measurement* (4th ed.). Wiley. (Classic reference for the fundamental principles of radiation detection and detector technologies.)

Organisation for Economic Co-operation and Development (OECD). (2019). *Nuclear waste management: Addressing the environmental and safety challenges*. Paris: OECD Publishing. (Contains information on nuclear waste management and long-term monitoring requirements.)

Smetana, J., & Dron, J. (2020). Applications of distributed sensor networks for radiation monitoring in nuclear facilities and the environment. *Nuclear Engineering and Design, 360,* 110534. (Examines current approaches to DRSN technology and distributed sensor networks.)

Turner, J. E. (2007). *Atoms, radiation, and radiation protection* (3rd ed.). Wiley-VCH. (A fundamental work for radiation-matter interaction, dosimetry, and protection principles.)

Ulgen, C., & Turker, A. (2024). Impacts of three different magnetic field applications on *M. offininalis* seed germination and seedling growth. *Biological Diversity and Conservation*. (Additional information on volume, issue, and page range is required as the publishing details were retrieved from the YÖK Academic system.)

Ulgen, C., Birinci Yildirim, A., Sahin, G., & Ucar Turker, A. (2021). Isolation, characterization, and antioxidant properties of pectin from unripe fig (*Ficus carica L.*). *Industrial Crops and Products, 173*, 113624. https://doi.org/10.1016/j.indcrop.2021.113624

Ulgen, C., Yildirim, A., & Turker, A. (2020). Enhancement of plant regeneration in lemon balm (*Melissa officinalis L.*) with different magnetic field applications. *International Journal of Secondary Metabolite, 7*(4), 133-144. https://doi.org/10.2174/138920101866617112010531 5

Ulgen, C., Yildirim, A., & Turker, A. (2023). *Melissa officinalis*: Antibacterial and antioxidant potential, phenolic profile and enzyme activities. *KSU Journal of Agriculture and Nature, 27*(4), 1146-1153.

Ulgen, C., Yildirim, A., Şahin, G., & Turker, A. (2021). Do magnetic field applications affect *in vitro* regeneration, growth, phenolic profiles, antioxidant potential and defense enzyme activities (SOD, CAT and PAL) in lemon balm (*Melissa officinalis L.*)? *Industrial Crops and Products, 173*, 113624. https://doi.org/10.1016/j.indcrop.2021.113624

United States Environmental Protection Agency (EPA). (2000). *Radiological monitoring plan for the environment*. Washington D.C.: EPA. (A technical guide on environmental radiation monitoring methodologies and standards.)

Wang, C. H., Willis, J. O., & Kester, D. A. (1975). *Radiotracer methodology in the biological, environmental, and physical sciences*. Prentice-Hall. (A foundational source for isotope applications and environmental monitoring methodology.)

World Nuclear Association (WNA). (2021). *Advanced nuclear power reactors*. (Covers the latest developments in nuclear energy technology, including SMRs and Fourth Generation reactors.)

Ziock, H. J., & Cooper, R. K. (2009). Semiconductor detectors for nuclear non-proliferation and homeland security. *IEEE Transactions on Nuclear Science, 56*(3), 1146–1152. (Focuses on the importance of new-generation semiconductors like CZT in security and portable applications.)

INVESTIGATION OF MoS_2 APPLICATIONS AS BIOSENSORS FOR CANCER DETECTION

Hamit ÖZTÜRK[1]

1. INTRODUCTION

Biosensor technologies, in particular, offer practical and rapid healthcare applications at the point of care, attracting researchers' attention for early disease diagnosis. They are also finding a place in various sectors such as the environment and the food industry. Considering that cancer is the second leading cause of male death, the importance of early and practical identification of disease pathogens becomes clearer. Biosensors are crucial for the detection of diseases such as Down syndrome, which offer early diagnosis to pregnant mothers. Another application area, for example, is the prostate-specific antigen (PSA) test, which detects prostate cancer in approximately 1.3 million male patients each year using blood serum. Therefore, the rapid, inexpensive, and practical production of disposable biosensors, particularly in the healthcare field mentioned here, is of great importance. Due to its high surface-to-volume ratio,

Here, we aim to provide the reader with some examples of how MoS_2 can be used in various cancer diagnosis methods in biosensor applications. This study can be considered as a mini review study.

[1] Assist. Prof. Dr., Isparta University of Applied Sciences, Technology Faculty, Basic Sciences, Isparta/Turkey, ORCID: 0000-0002-9968-6377.

2. THE ROLE OF MoS_2 IN CANCER DIAGNOSIS

MoS_2 can interact strongly with biomolecules, making it a promising candidate for biosensor applications. These properties of MoS_2 Biosensors enable the investigated biomolecules to easily adsorb onto the sensor surface, resulting in a significant increase in the output signal.

2.1. Detecting of Lung Cancer Cell Types in Hydroplegia

In a 2022 study, Mukundan et al. produced a single-layer MoS_2 structure exhibiting n-type semiconductor properties using chemical vapor deposition (CVD). The MoS_2 structure was then examined using Raman spectroscopy, atomic force microscopy, and photoluminescence measurements. Transmission electron microscopy was also used. The sensor configuration then required a p-n junction structure, so the MoS_2 structure was transferred to an electrochemically produced Cu_2O structure exhibiting p-type semiconductor properties. This created a p-n junction structure. They demonstrated the sensor's hydrological utility for identifying lung cancer cell types. Because the number of cells examined significantly affects the photocurrent, they demonstrated that three different cell types and numbers can be identified using the slope of this photocurrent. Consequently, they reported in the literature that the current system reduces the long waiting time required for disease detection (Mukundan et al., 2025).

The electrochemical deposition method used in this study for the synthesis of Cu_2O was chosen because it is simple, low-cost, and offers homogeneity across a wide range of application surfaces. Furthermore, this method allows for the formation of crystal shapes and the orientation of the crystal lattice by controlling the pH of the solution. This provides flexibility for researchers' work. The electrolyte properties used in the synthesis

of Cu_2O are given as follows: the electrolyte is a 1000 cc aqueous solution, the mixture of which contains 0.4 M copper sulphate powder ($CuSO_4$), 85% lactic acid and 5 M sodium hydroxide (NaOH) as reported in the relevant study. In this experiment, one of the electrodes during electrochemical deposition was an ITO glass substrate, while the other was a graphite rod. Both electrodes were connected to a DC power supply, and the coating process was carried out at 60 degrees Celsius for 30 minutes.

In addition, it was also stated in this study that the Cu_2O surface was subjected to grinding for 1 hour in order to smooth the Cu_2O surface and facilitate the Mos_2 transfer.

Table 1. List of chemicals used for Cu_2O (Mukundan et al., 2025).

Drug Name	Specification	Manufacturer	Agent Vendor
ITO Substrate	Size: 2cm*2cm	Ruilong Optoelectronics	Ruilong Optoelectronics
Methanol	Purity: 99.9%	Shimajiu Pharmaceutical	Rishun Instruments
Acetone	Purity: 99.9%	Shimajiu Pharmaceutical	Rishun Instruments
Isopropanol	Purity: 99.9%	Sigma-Aldrich	Youhe Trading
Pentahydrate and copper sulfate	Purity: 98+%	Alfa Aesar	Jingming Chemical
DL-Lactic acid	Purity: 85%	TEDIA	Jingming Chemical
Sodium Hydroxide	Purity: 98+%	Sigma-Aldrich	Youhe Trading
De-ionized water	Purity: 99.9%	Rephile	Yushun Instruments
High Pressure Nitrogen	Purity: 99.9%	Lianhua Gas	Lianhua Gas

In this study, silicon dioxide (SiO_2) with (100) crystal planes was used to grow MoS_2 by the CVD method. Sulfur powder with 99.98% impurity and (MoO_3) powder with 99.95% impurity were used as starting chemicals. In the current experiment, the SiO_2 silicon layer was cleaned by ultrasonication in acetone for 10 minutes; then, deionized water was used. Argon inert gas was used to grow MoS_2 in the CVD. The growth process was set to remain at 650°C for 30 minutes, and the rate of increase to this temperature was chosen as 20°C per minute. When the sample temperature dropped until the 400°C, the CVD lid was opened, and the experiment was terminated. The distance was set at 46 cm which is related to the molybdenum trioxide (MoO_3) and sulfur powder (S) distance between each other. Temperatures of the MoO_3 and S locations were adjusted at 650°C and 200°C,

respectively. The purpose of choosing this distance between the two crucibles is to ensure that the sulfur gradient in the MoO_3 medium is much lower.

Table 2. List of chemicals used to grow MoS_2 (Mukundan et al., 2025).

Drug Name	Specification	Manufacturer	Agent Vendor
SiO_2	Size: 4 inches	Yimei Materials	Yimei Materials
S powder	99.98%	Weiss Enterprise	Weiss Enterprise
MoO_3 Powder	99.95%	Weiss Enterprise	Weiss Enterprise
Acetone	Purity: 99.9%	Shimajiu Pharmaceutical	Rishun Instruments
Sodium Hydroxide	Purity: 98+%	Sigma-Aldrich	Youhe Trading
PMMA A5	molecular weight:950	Asia Pacific International Electronics	Asia Pacific International Electronics
Nitric acid	Purity:68-69%	CHONEYE	Yushun Instruments
HCl	Purity: 37%	FLUKA	Jingming Chemical
De-ionized water	Purity: 99.9%	Rephile	Yushun Instruments
High Pressure Nitrogen	Purity: 99.9%	Lianhua Gas	Lianhua Gas

The transfer process of MoS_2 to the Cu_2O surface with the spin coater system is as shown in Figure 1.

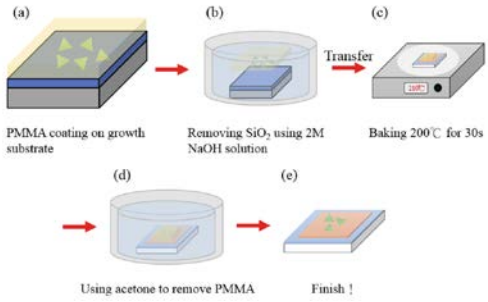

Fig.1. The transfer process of MoS_2 to the Cu_2O surface (Mukundan et al., 2025).

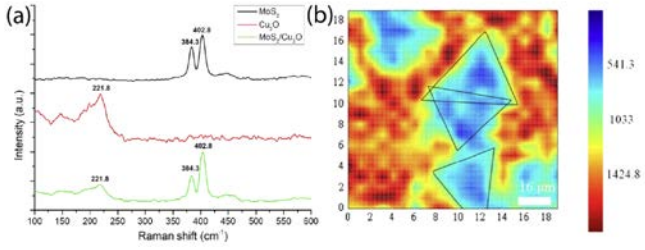

Fig. 2. a) Raman spectrum of MoS_2/Cu_2O. b) Raman mapping of MoS_2/Cu_2O (Mukundan et al., 2025).

In this study, glutathione (GSH) and glutathione disulfide (GSSG) were used to validate biosensor parameters. The sensor's basic detection mechanism is that the GSH/GSSG ratio in healthy cells is greater than 10:1, while this ratio decreases in cancer cells. In PEC devices used as sensors, GSSG recombines with photoelectrons upon irradiation of n-type PEC. Therefore, an increase in the measured photocurrent is observed, directly related to increasing cancer severity (Hammond et al., 2001). If the PEC sensor used is a p-type sensor, the more intense the carniogenesis of the structure to be examined, the lower the GSH concentration. Consequently, lower GSH results in lower photocurrent (Kang et al., 2001).

In this study, three different cell types (A549, NCI-H460, and NCI-H520) were studied, and the photocurrent slopes corresponding to each cell were determined as 0.000452, 0.000749, and 0.000174, respectively (Figure 3). The type of cell used can also be determined by considering the regression curve equation and photocurrent intensity. Additionally, the optimal working thickness of the sensor was reported as 0.7 nm for MoS_2 and 2 μm for Cu_2O. In this study, white light was used as the light source.

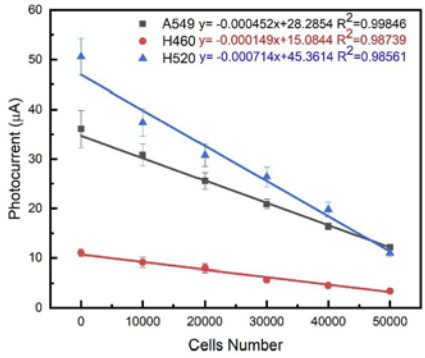

Fig. 3. Linear relationship between the photocurrent changes produced by three lung cancer cells on the sensor and the cell number (Mukundan et al., 2025).

2.2. Usability of the MoS_2 Biosensor in Cancer Type Detection by Glutathione Determination

Glutathione (GSH), the most abundant thiol in biological systems but not found in proteins structure, is essential for regulating thiol levels, controlling cell proliferation, and protecting cells from toxic substances and free radicals. In this study, Rawat and colleagues reported the development of a MoS_2-based electrochemical sensor and used glutathione (GSH) measurement as the sensor's operating principle (Rawat et al., 2020). GSH plays a crucial role in the detection of cancer and several other diseases and is considered a critical biomarker in healthcare. In this study, they measured GSH in the presence of Glutathione-S-transferase (GST) and investigated the electrochemical activity of the 1-chloro-2,4-dinitrobenzene (CDNB) structure by measuring GSH after GST was immobilized on the MoS_2 surface. According to this study, the MoS_2-based sensor demonstrated exceptional stability and reproducibility, making it suitable for cancer detection and measurement. Numerous clinical studies in the literature have shown that GSH levels are directly linked to many human diseases, such as Alzheimer's, cancer, HIV-AIDS, and liver damage. This has been documented in the literature by monitoring increases and decreases in GSH levels (Gamcsik et al., 2012; Bansal et al., 2012; Ballatori et al., 2012). This is detailed in Table 3.

Table 3. The relationship between some different diseases and Glutathione (GSH) concentration

Diseases	Ratio of tumor glutathione to control tissue level
Brain Cancers	0.3-0.6
Breast Cancer	2-8.4
Gastrointestinal cancer	1.3-1.9
Gynecological Cancers	1-2.6
Head and Neck Cancer	1-2.6
Lung Cancer	2-4.6
Parkinson/Alzheimer/ AIDS	Lower

In live cells, GSH concentrations range from 0.5 to 10 mM, whereas in healthy persons' physiological fluids, they range from 2 to 12 µM (Gamcsik et al., 2012; Hanko et al., 2019). Less than 10% of glutathione is found in its oxidized state, whereas over 90% is found in its reduced form (Slivka et al., 1987).

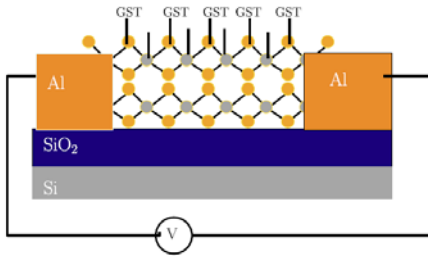

Fig. 4. Schematic representation of the fabricated sensor (Rawat et al., 2020).

According to this study reported in the literatüre, after immobilizing glutathione-S-transferase (GST) on the MoS_2 surface, GSH was detected using the electrochemical activity of GSH and 1-chloro-2,4-dinitrobenzene (CDNB) in the presence of GST. When compared to a blank test, the MoS_2-based sensor demonstrated a 535-fold greater current and good selectivity (Rawat et al., 2020) shown as in Figure 5.

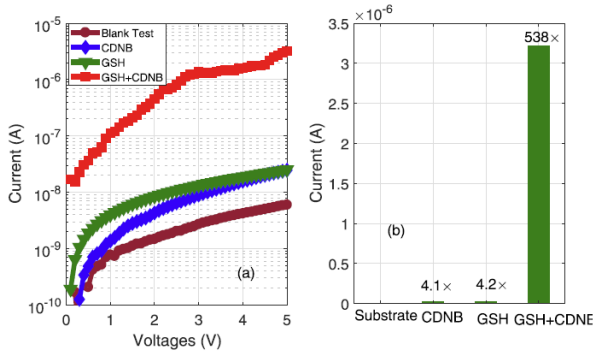

Fig. 5. The current-voltage graph (a) and the current change at 5 V under four distinct situations (b) are displayed. The current-voltage measurement of the sensor was carried out at a concentration of 100 µM (Rawat et al., 2020).

In this work, liquid phase exfoliation was used to create multilayered MoS_2 nanosheets from MoS_2 powder (Gupta et al., 2018). First, an aqueous solution of cetyltrimethylammonium bromide (CTAB) was mixed with 30 mg of MoS_2 powder. The aqueous solution was sonicated for four hours at 80 W as a second step, followed by probe sonication at a constant temperature of 250°C for 15 minutes at a power output of 127.5 W, with a cycle of 7 seconds on and 5 seconds off. The dispersed solution was then centrifuged at 7,000 rpm for 30 minutes to allow large particles to settle to the bottom of the Eppendorf tube.

The GST protein was first incubated in a phosphate-buffered saline (PBS) buffer solution containing a 1:1 ratio of MoS_2 and CTAB powder. This process was carried out at room temperature using a rotary shaker. This process, which lasted a total of three hours, aimed to improve electrostatic interactions.

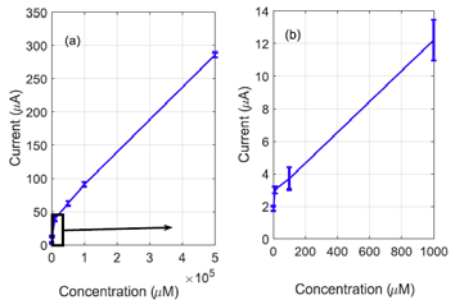

Fig. 6. Current graphs (executed at 5V) versus GSH concentrations (a) show the full GSH concentration range and (b) show low GSH concentration (Rawat et al., 2020).

In this research, the suspension was centrifuged at 8,000 rpm for 30 minutes. This process allows that the bound protein to settle to the bottom of the Eppendorf tube. Because unbound protein was also present in the supernatant, the binding efficiency was measured. For this purpose, a UV spectrophotometer was used in this study to assess the amount of free protein (Rawat et al., 2020). Moreover, UV lithography and thermal evaporation

methods were executed to fabricate the electrodes (source and drain) of the biosensor chip. This process resulted in 50 nm thick Al electrodes with a 25 μm interval. A combination of diluted MoS_2 and GST was used for the drop casting process. The sample was sonicated for 30 seconds to distribute the MoS_2 nanoplatelets with a sliding structure evenly across each layer (Rawat et al., 2020). The reproducibility and time-dependent stability of the produced biosensor with other sensors produced by the same method are presented in detail in Figure 7.

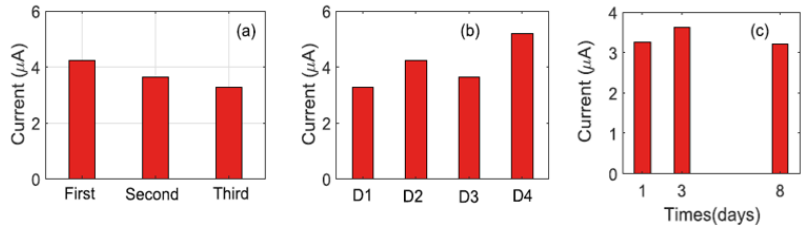

Fig. 7. The stability tests of the sensor regarding the detection of 100 μM GSH+CDNB at 5 V of the produced sensor are presented in the study as follows: a) Different measurements made using the same sensor b) Measurement results taken at the same concentration with 4 different sensors produced with the methods specified in this study c) Measurement results taken at the same concentration with the same sensor at different times (Rawat et al., 2020).

2.3. Detection of TNF Alpha in Cancer Patients with MoS_2 Biosensor

Tumor Necrosis Factor (TNF) is a critical factor in apoptosis and cancer diagnosis. This study also reported that the biosensor reported in this study is the first biosensor produced to detect TNF in cancer patients.Sri and colleagues reported in the literature the development of a MoS_2-based nanosensor for detecting TNF in cancer patients using electrophoretic deposition (Sri et al., 2022). In this study, the biosensor used indium tin oxide (ITO)-coated glass as a substrate, and MoS_2 was deposited on this

substrate using electrophoretic deposition, following the specified processes.

In this study, the MoS_2 nanoflower (MoS_2nf) structure was produced using a known hydrothermal method. Initially, the chemicals used were sodium molybdate Na2MoO4 2H2O (1.0 g) and thiourea (1.2 g) as Mo and S sources, respectively. These chemicals were dissolved in 80 ml of deionized water in a beaker.

An acidic environment was created using oxalic acid (0.4 g). The resulting solution was transferred to a 100 ml stainless steel, Teflon-lined autoclave. MoS_2nf was formed in this autoclave by heating at 200 °C for 24 hours. The resulting MoS_2nf was observed as a black precipitate. The MoS_2nf material was then rinsed with an ethanol-water mixture. It was reported that it was crushed with a mortar and pestle to ensure homogeneity (Sri et al., 2022).

ITO-coated glass material (1.5 cm x 0.5 cm) to hydrolyze, a 1:1:5 solution of ammonia, hydrogen peroxide, and water was prepared to hydrolyze the used in this study. After applying it to the conductive surface of the electrodes, this solution was held at 80 °C for one hour. MoS_2nf (2 mg ml-1) was then fabricated as a colloidal solution in the acetonitrile. 100 μL of the previously produced colloidal solution was dispersed in 3 ml of acetonitrile and sonicated for a period of time. A two-electrode system (platinum plate as cathode and ITO as anode) was then submissive to a 50 V potential for 3 minutes. The aim of this study was to form a homogeneous MoS_2nf layer onto the ITO surface.

Used in this research materail which is monoclonal anti-TNF-α and Tumor Necrosis Factor-α (TNF-α) were obtained from MyBio. For immobilization, three distinct doses of monoclonal anti-TNF-α (1, 5, and 10 μg ml-1) were produced in phosphate-buffered saline (PBS). Figure 8 shows a schematic illustration of the BSA/anti-TNF-α/MoS_2nf/ITO

immunoelectrode fabrication after 10 μL of the solution was adsorbed onto MoS_2nf/ITO electrodes and Figure 9 shows spectroscopic response of immunosensor impedance (Sri et al., 2022).

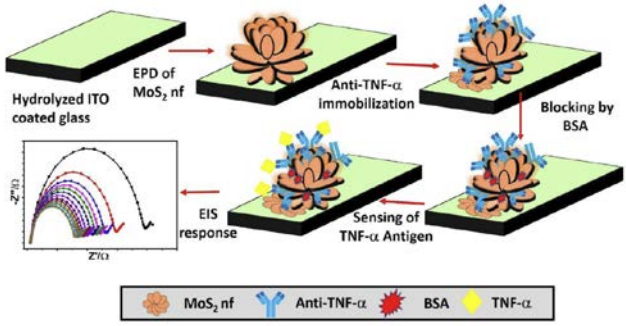

Fig. 8. Schematic representation of the fabrication process of the BSA/anti-TNF-α/MoS_2 nf/ITO immunoelectrode.

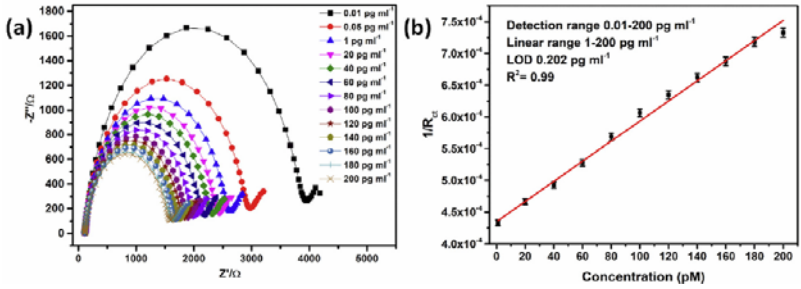

Fig. 9. (a) Spectroscopic response of immunosensor impedance dependent on TNF-α concentration, (b) calibration curve R ct −1 versus TNF-α concentration (Sri et al., 2022).

3. CONCLUTION AND FUTURE PERSPECTIVE

MoS_2's electronic, optical, and mechanical properties make it a prime candidate for a fundamental material for various future applications. These properties are already attracting the attention of researchers for various industrial, healthcare, and

scientific applications. While graphene is also a promising candidate in this field, MoS_2's unique optical and electronic properties, due to its semiconductor properties, can be considered a step ahead of graphene.

Future goals could be presented to the readers, improving MoS_2's time-dependent reproducibility, ensuring its longer-term stability and exploring hybrid versions of MoS_2 with other recently emerging materials science structures, such as polymers and carbon nanotubes. A future vision for this material is presented. This could lead to the development of disposable chip versions that can be embedded in devices in hospitals or laboratories for early disease diagnosis, and their potential use in healthcare applications that benefit human health.

REFERENCES

Ballatori, N., Krance, S. M., Notenboom, S., Shi, S., Tieu, K., & Hammond, C. L. (2009). Glutathione dysregulation and the etiology and progression of human diseases. *Biological chemistry*, *390*(3), 191.

Bansal, A., & Simon, M. C. (2018). Glutathione metabolism in cancer progression and treatment resistance. *Journal of Cell Biology*, *217*(7), 2291-2298.

Gamcsik, M. P., Kasibhatla, M. S., Teeter, S. D., & Colvin, O. M. (2012). Glutathione levels in human tumors. *Biomarkers*, *17*(8), 671-691.

Gupta, A., & Vasudevan, S. (2018). Understanding surfactant stabilization of MoS_2 nanosheets in aqueous dispersions from zeta potential measurements and molecular dynamics simulations. *The Journal of Physical Chemistry C*, *122*(33), 19243-19250.

Hammond, C. L., Lee, T. K., & Ballatori, N. (2001). Novel roles for glutathione in gene expression, cell death, and membrane transport of organic solutes. *Journal of hepatology*, *34*(6), 946-954.

Hanko, M., Švorc, Ľ., Planková, A., & Mikuš, P. (2019). Overview and recent advances in electrochemical sensing of glutathione–A review. *Analytica chimica acta*, *1062*, 1-27.

Kang, Z., Yan, X., Wang, Y., Bai, Z., Liu, Y., Zhang, Z., ... & Zhang, Y. (2015). Electronic structure engineering of Cu2O film/ZnO nanorods array all-oxide pn heterostructure for enhanced photoelectrochemical property and self-powered biosensing application. *Scientific Reports*, *5*(1), 7882.

Mukundan, A.; Feng, S.-W.; Weng, Y.-H.; Tsao, Y.-M.; Artemkina, S.B.; Fedorov, V.E.; Lin, Y.-S.; Huang, Y.-C.; Wang, H.-C. Optical and Material Characteristics of MoS_2/Cu2O Sensor for Detection of Lung Cancer Cell Types in Hydroplegia. Int. J. Mol. Sci. 2022, 23, 4745.

Rawat, B.; Mishra, K.K.; Barman, U.; Arora, L.; Pal, D.; Paily, R.P. Two-Dimensional MoS_2-Based Electrochemical Biosensor for Highly Selective Detection of Glutathione. IEEE Sens. J. 2020, 20, 6937–6944.

Slivka, A., Spina, M. B., & Cohen, G. (1987). Reduced and oxidized glutathione in human and monkey brain. *Neuroscience letters*, *74*(1), 112-118.

Sri, S.; Chauhan, D.; Lakshmi, G.; Thakar, A.; Solanki, P.R. MoS_2 nanoflower based electrochemical biosensor for TNF alpha detection in cancer patients. Electrochim. Acta 2022, 405, 139736.

IMPACT OF ELECTRODE DENSITY AND WINDOW DURATION ON EEG DYNAMICS

Hazret TEKİN[1]

1. INTRODUCTION

Electroencephalography (EEG) has emerged as one of the most informative and widely used non-invasive neurophysiological tools for capturing and decoding brain activity. By measuring voltage fluctuations produced by synchronous neuronal firing across the cerebral cortex, EEG provides a high-temporal-resolution view of neural dynamics underlying perception, cognition, and motor control (Patel et al., 2021). Owing to its millisecond-level precision and portability, EEG has become a key modality in a wide range of applications, including brain–computer interfaces (BCIs), mental workload estimation, emotion recognition, and clinical neurodiagnostics. Recent advances in sensor technology and signal analytics have enabled the development of multi-channel, high-density EEG systems, which can record complex cortical patterns with improved spatial–temporal fidelity(Belcher et al., 2022).

In multi-channel EEG acquisition, electrodes are systematically positioned according to standardized montages such as the 10–20 or 10–10 system, ensuring consistent spatial coverage of cortical regions (Guttmann-Flury et al., 2023). The number, positioning, and distribution of electrodes critically determine the richness and discriminability of the captured brain signals. A smaller number of electrodes may fail to capture

[1] Asst. Prof. Dr., Şırnak University, Vocational School of Technical Sciences, ORCID: 0000-0002-9379-721X.

distributed neural activity or inter-regional synchronization, thereby limiting recognition accuracy and spatial resolution (R. Sharma & Meena, 2024). Conversely, dense electrode arrays can provide richer spatial information but often introduce signal redundancy, volume conduction effects, and computational overhead (Al-Nafjan & Aldayel, 2022). Determining an optimal channel configuration—one that captures sufficient spatial detail while maintaining computational efficiency—remains a fundamental challenge for EEG-based decoding systems. Understanding how channel count influences feature expressiveness, classifier generalization, and robustness is essential for optimizing both the analytical accuracy and real-time practicality of EEG-based recognition frameworks.

Equally important is the temporal segmentation of EEG signals, which defines the window length used for feature extraction and classification. Segment duration governs the temporal granularity of neural pattern analysis. Shorter windows can effectively capture transient changes in brain rhythms or cognitive states, yielding faster response times that are crucial in real-time BCI applications (L. D. Sharma et al., 2022). However, these short segments often provide limited statistical stability and higher susceptibility to noise. In contrast, longer windows yield more stable and smoother features by averaging temporal fluctuations, but they compromise responsiveness and temporal precision. This trade-off between temporal resolution and feature stability is particularly critical in EEG-based mental state and event-related classification, where rapid transitions between brain states demand both sensitivity and speed.

To examine these complementary dimensions—spatial resolution (channel count) and temporal resolution (segment length)—the present study conducts a systematic ablation analysis to evaluate their individual and combined influence on EEG classification performance. Unlike frequency- or wavelet-

based approaches, which focus on spectral power decomposition, this work emphasizes time-domain analytical methods that directly characterize the dynamic properties of EEG signals. Specifically, the framework employs Hjorth parameters (Activity, Mobility, and Complexity), statistical time-domain features (such as variance, skewness, and kurtosis) to comprehensively describe neural variability, regularity, and signal complexity. These descriptors provide interpretable insights into cortical dynamics while remaining computationally efficient for real-time analysis.

Three classical machine learning classifiers—Random Forest, k-Nearest Neighbors (KNN), and Logistic Regression—are utilized to ensure methodological transparency and cross-condition consistency. By applying identical preprocessing and evaluation settings across different spatial and temporal configurations, the study isolates the impact of channel count and segment length on recognition accuracy, feature robustness, and computational efficiency. The outcomes of this work are expected to establish practical guidelines for designing EEG-based recognition and BCI systems with optimized spatial–temporal configurations, bridging the gap between analytical rigor and real-time neurotechnology applications.

2. MATERIAL

The experimental data used in this study were obtained from the EEGMAT database (Zyma et al., 2019), a publicly available dataset hosted on PhysioNet. This benchmark collection includes EEG recordings captured before and during mental arithmetic tasks, providing a reliable source for studying cognitive workload and neural dynamics. Recordings were acquired using a 23-channel Neurocom system (XAI-MEDICA, Ukraine) with 21 active channels—including 20 EEG and 1

ECG—arranged according to the International 10–20 system and referenced to linked earlobes. Signals were filtered using a 30 Hz high-pass filter and a 50 Hz notch filter to suppress baseline drift and power-line interference. Each 60-second recording segment was verified to be artifact-free and preprocessed with Independent Component Analysis (ICA) to remove ocular, muscular, and cardiac components. During the mental arithmetic task, participants continuously performed serial subtractions of orally presented four-digit and two-digit numbers (e.g., 3141 − 42), maintaining accuracy and pace. This paradigm reliably elicits moderate cognitive load, typically reflected by increased theta and decreased alpha activity, serving as a clear contrast to the resting baseline. Figures 1 and 2 illustrate the EEG activity of the 20 active channels under the two experimental conditions—baseline (Label 1) and mental arithmetic (Label 2)—highlighting the distinct cortical activation patterns observed across the electrode network.

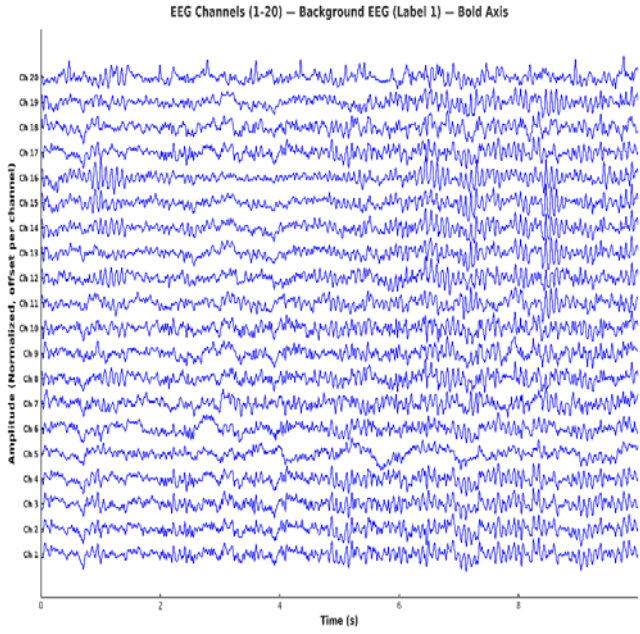

Figure 1. Baseline EEG activity across 20 channels (Label 1)

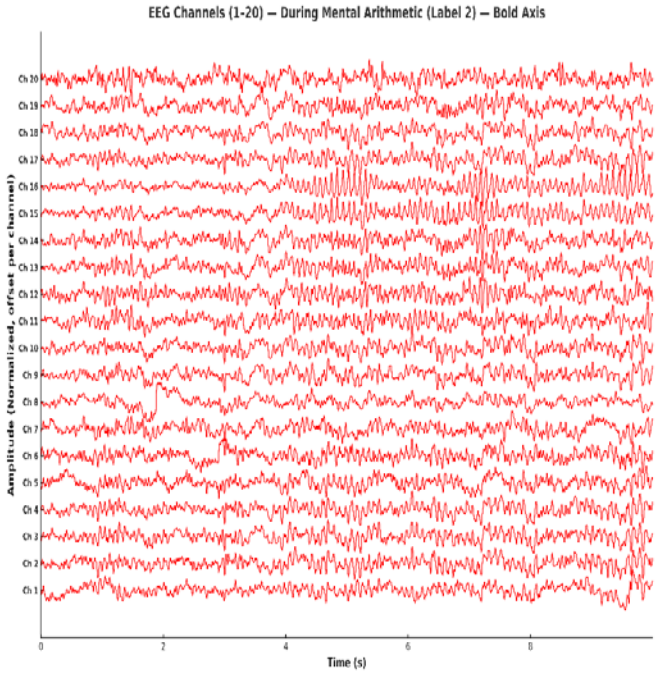

Figure 2. Mental arithmetic EEG activity across 20 channels (Label 2)

3. METHOD

The methodological framework of this study was designed to evaluate how variations in temporal and spatial parameters influence EEG-based cognitive state classification. The approach follows a structured sequence from raw data processing to model evaluation, ensuring reproducibility and interpretability.

As illustrated in Figure 3, the workflow begins with raw EEG data, which are segmented into multiple non-overlapping windows of 10–50 ms to assess the effect of temporal resolution. The dataset is divided using a stratified hold-out split (60% training, 40% testing) to maintain balanced class distributions. Subsequently, correlation-based channel selection is applied to

remove redundant spatial information, retaining the ten most informative channels. An ablation analysis is then conducted by gradually increasing the number of active channels (n = 1–10) to examine how spatial dimensionality affects classification metrics. From each segment, time-domain features—including mean, variance, waveform length, and Hjorth parameters (Activity, Mobility, and Complexity)—are extracted to characterize signal dynamics. Finally, KNN, Logistic Regression, and Random Forest classifiers are trained and evaluated using accuracy and F1-score to compare performance across different temporal and spatial configurations.

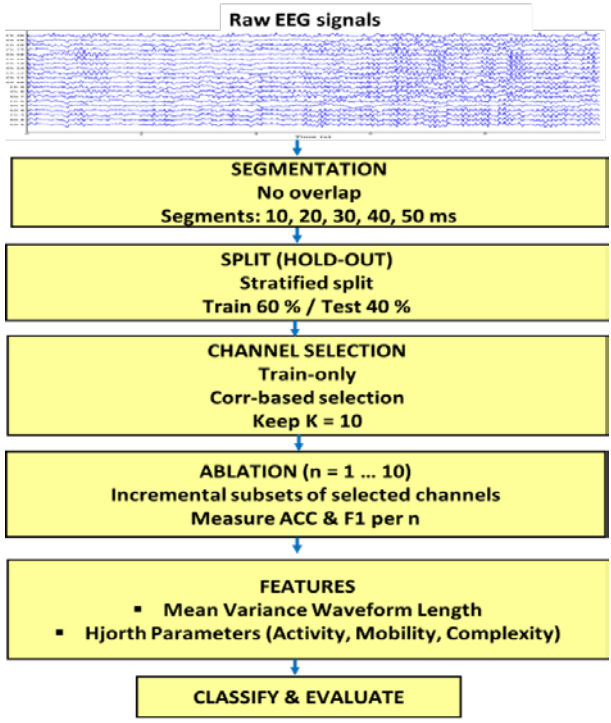

Figure 3. EEG signal classification workflow

3.1. Segmentation

Segmentation is a critical step in EEG signal processing, transforming continuous recordings into structured time windows

suitable for analysis and classification. The choice of window length determines the balance between temporal precision and signal stability. Short windows capture rapid cognitive transitions but may introduce noise, while longer ones improve statistical reliability at the cost of temporal detail.

In this study, fixed and non-overlapping windows of 10, 20, 30, 40, and 50 ms were used to systematically examine how temporal resolution affects model performance. This multi-scale segmentation enabled a clear assessment of classification sensitivity across different time spans. Each segment was normalized and labeled according to the dominant mental state (baseline or mental arithmetic), establishing a consistent foundation for subsequent channel selection, feature extraction, and classification stages..

3.2. Channel Selection

Channel selection plays a critical role in optimizing the spatial resolution and computational efficiency of EEG-based classification systems. In multi-channel EEG recordings, numerous electrodes capture overlapping neural activity, often introducing redundancy and noise. Therefore, selecting an optimal subset of electrodes is essential for improving both model interpretability and performance while reducing computational cost. In EEG analysis, channels are typically selected based on statistical or correlation-based criteria that identify electrodes carrying unique, non-redundant information. This process ensures that the retained channels provide maximal spatial coverage of relevant brain regions while minimizing the influence of highly correlated or noisy signals.

In the present study, a correlation-based redundancy elimination approach was applied exclusively to the training data to prevent information leakage. Initially, all 20 EEG channels were evaluated for inter-channel correlations, and highly

correlated pairs (above a threshold of 0.85) were pruned iteratively until a reduced set of 10 representative channels was obtained. This optimized subset preserved the most discriminative spatial information while enhancing computational efficiency. The selected channels were subsequently used in the ablation analysis to evaluate the impact of spatial dimensionality on classification performance.

3.3. Ablation Analysis

Ablation analysis serves as a systematic approach to evaluate how variations in model input parameters—such as the number of EEG channels or segment lengths—affect overall classification performance. In EEG-based cognitive state recognition, such analyses are essential for understanding the trade-offs between data dimensionality, computational cost, and model accuracy. By incrementally modifying one parameter while keeping others constant, ablation studies provide direct insight into the relative importance and contribution of different design choices within the signal processing pipeline.

In this study, two primary ablation procedures were conducted: channel ablation and segment-length ablation. Channel ablation progressively increased the number of channels used for classification (from 1 to 10) to quantify how spatial information contributes to recognition accuracy and F1-score. This analysis revealed the performance saturation point, beyond which additional channels offered diminishing returns. Conversely, segment-length ablation explored temporal sensitivity by evaluating multiple window durations (10, 20, 30, 40, and 50 ms), allowing assessment of how temporal granularity influences model robustness and responsiveness. Together, these ablation experiments provided an empirical understanding of how spatial and temporal configurations impact EEG classification

performance, enabling the identification of an optimal balance between accuracy and computational efficiency.

3.4. Feature Extraction

Feature extraction is a vital step in EEG signal analysis, aiming to transform raw time-series data into compact and discriminative representations suitable for machine learning. Because EEG signals are inherently non-stationary and highly variable, meaningful characterization requires the extraction of features that capture both statistical and dynamical properties of neural activity (Hag et al., 2021). The goal is to enhance class separability by encoding essential information about amplitude fluctuations, frequency composition, and signal complexity while reducing redundancy.

In this study, feature extraction was performed on each segmented EEG window to derive a set of time-domain descriptors known for their effectiveness in cognitive and mental workload recognition. Specifically, six features were computed per channel:

- Mean amplitude, representing the overall signal level;
- Variance, quantifying signal power and stability;
- Waveform Length (WL), expressing signal complexity through the cumulative absolute difference between consecutive samples;
- Hjorth parameters—Activity, Mobility, and Complexity—which describe the statistical variance, frequency content, and structural variability of the EEG waveform (Hadiyoso & Rizal, 2017).

These features collectively provide a balance between interpretability and discriminative strength, capturing both the amplitude-based and temporal dynamics of EEG signals. The extracted feature vectors from all channels were concatenated to

form the input space for subsequent classification, ensuring that each segment was represented by a consistent and physiologically meaningful feature set.

3.5. Machine Learning Classification

The final stage of the proposed EEG analysis framework involves classification, where the extracted feature vectors are mapped to their corresponding cognitive states using supervised machine learning algorithms (Cao et al., 2022). The objective of this stage is to evaluate how effectively the selected spatial–temporal configurations (i.e., channel count and segment length) contribute to the discriminative modeling of mental arithmetic versus baseline states.

In this study, three well-established algorithms were employed to ensure both interpretability and generalizability: Random Forest (RF), k-Nearest Neighbors (KNN), and Logistic Regression (LR). Random Forest, an ensemble of decision trees, was chosen for its robustness to noise and ability to model nonlinear relationships(Rahman et al., 2022). KNN, a distance-based method, was included to assess classification performance under local feature-space similarity assumptions. Logistic Regression, as a linear probabilistic model, provided a baseline for evaluating linear separability of the extracted features.

Each model was trained on the training subset and evaluated on the test data obtained from the hold-out procedure. The dataset was divided into training and testing subsets using a StratifiedShuffleSplit hold-out strategy, ensuring balanced class representation across both sets. Specifically, 60% of the data was used for training and 40% for testing, with the randomization process controlled by a fixed random state of 42 to guarantee reproducibility of the results. To evaluate the influence of spatial (channel count) and temporal (segment length) configurations, each model was trained and tested under identical preprocessing

and feature extraction conditions. Three classical machine learning algorithms—Random Forest (RF), k-Nearest Neighbors (KNN), and Logistic Regression (LR)—were employed to ensure interpretability and consistency. The hyperparameter settings for these classifiers are summarized in Table 1 below.

Table 1. Classifier hyperparameter settings

Method	Key Parameters (explicit)	Defaults (context)
Random Forest (RF)	n_estimators=300, random_state=42, n_jobs=-1	criterion='gini', max_depth=None, bootstrap=True
k-Nearest Neighbors (KNN)	n_neighbors=5, weights='distance', p=2	metric='minkowski' (p=2 → Euclidean)
Logistic Regression (LR)	max_iter=2000	solver='lbfgs', penalty='l2'

Model performance was assessed through multiple metrics—accuracy (ACC), F1-score, Receiver Operating Characteristic (ROC) curves, and confusion matrices—to capture both overall predictive power and class-specific balance. This combination of algorithms and evaluation criteria allowed for a comprehensive assessment of how different spatial and temporal factors influence EEG-based classification performance, highlighting the trade-off between feature richness and computational efficiency.

4. EXPERIMENTAL EVALUATION

This section presents the experimental results of the proposed EEG-based classification framework, evaluated across five subjects under identical preprocessing, segmentation, and feature extraction procedures. The analysis aims to examine how segment length and channel count affect classification performance across three machine learning models—KNN, Logistic Regression, and Random Forest. Tables 2 to 6 present the classification performance achieved at different segment

lengths. Figures 4 to 13 illustrate the ablation results showing how classification accuracy and F1-scores vary with segment length and the number of EEG channels.

Across all five subjects, classification accuracy consistently improved with longer segment durations. Short windows (10–20 ms) yielded lower stability and discriminative power, while windows of 40–50 ms provided optimal performance by capturing more complete temporal patterns. This trend indicates that moderate segment lengths balance temporal precision and feature robustness effectively in EEG-based cognitive state classification.

Across all five subjects, classification accuracy improved notably as the number of EEG channels increased. Performance gains were most prominent up to around 4–6 channels, beyond which improvements tended to plateau, indicating redundancy among additional electrodes. This suggests that a compact channel subset can achieve high accuracy, supporting the efficiency of correlation-based channel selection in reducing dimensionality without significant information loss..

Table 2. Classification performance of Subject 1 across different segment lengths (10–50 ms).

Classifier	10 ms (ACC/F1)	20 ms (ACC/F1)	30 ms (ACC/F1)	40 ms (ACC/F1)	50 ms (ACC/F1)
KNN	0.805 / 0.661	0.831 / 0.720	0.830 / 0.711	0.867 / 0.793	0.864 / 0.781
LogisticRegression	0.891 / 0.843	0.929 / 0.904	0.948 / 0.931	0.966 / 0.955	0.971 / 0.962
RandomForest	0.890 / 0.838	0.914 / 0.879	0.934 / 0.908	0.951 / 0.933	0.952 / 0.934

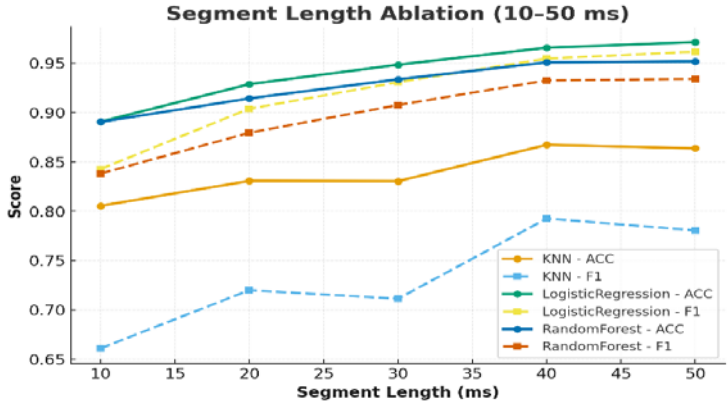

Figure 4. Segment length ablation results (10–50 ms) for Subject 1

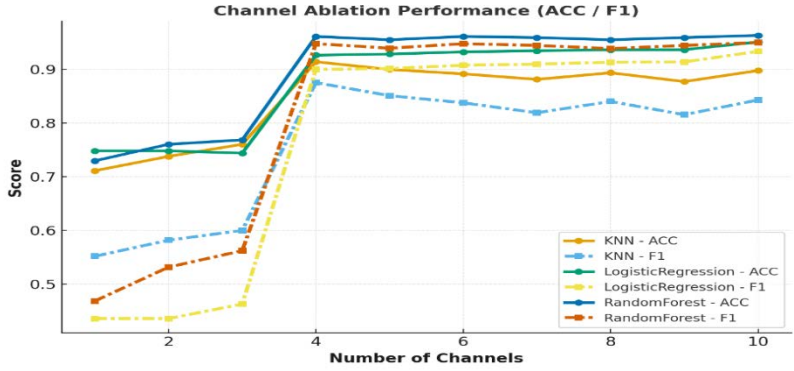

Figure 5. Channel ablation performance (1–10 channels) for Subject 1

Table 3. Classification performance of Subject 2 across different segment lengths (10–50 ms).

Classifier	10 ms (ACC/F1)	20 ms (ACC/F1)	30 ms (ACC/F1)	40 ms (ACC/F1)	50 ms (ACC/F1)
KNN	0.8 / 0.623	0.81 / 0.648	0.8 / 0.619	0.821 / 0.675	0.829 / 0.696
LogisticRegression	0.894 / 0.852	0.935 / 0.912	0.957 / 0.941	0.97 / 0.959	0.976 / 0.968
RandomForest	0.909 / 0.873	0.921 / 0.892	0.947 / 0.928	0.962 / 0.949	0.963 / 0.951

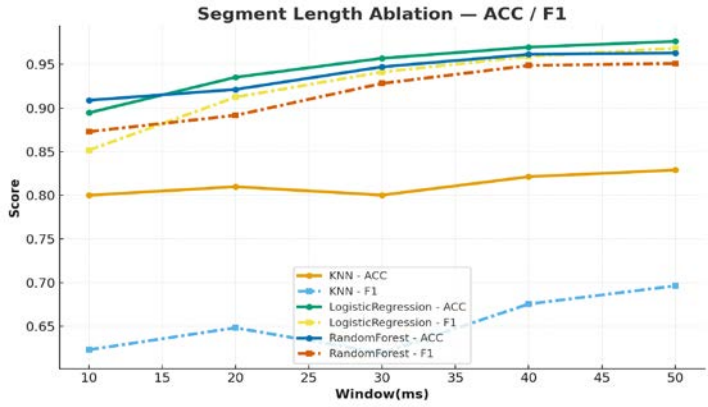

Figure 6. Segment length ablation results (10–50 ms) for Subject 2

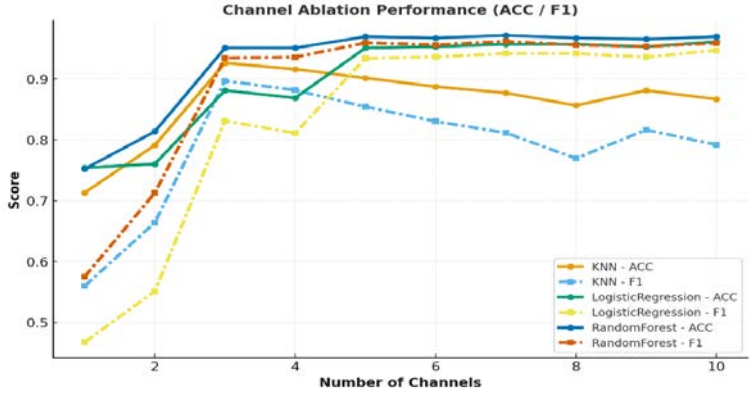

Figure 7. Channel ablation performance (1–10 channels) for Subject 2

Table 4. Classification performance of Subject 3 across different segment lengths (10–50 ms).

Classifier	**10 ms (ACC/F1)**	**20 ms (ACC/F1)**	**30 ms (ACC/F1)**	**40 ms (ACC/F1)**	**50 ms (ACC/F1)**
KNN	0.824 / 0.722	0.854 / 0.779	0.883 / 0.83	0.921 / 0.889	0.913 / 0.872
LogisticRegression	0.86 / 0.805	0.915 / 0.884	0.938 / 0.917	0.956 / 0.942	0.964 / 0.952
RandomForest	0.87 / 0.796	0.887 / 0.826	0.916 / 0.876	0.925 / 0.89	0.938 / 0.911

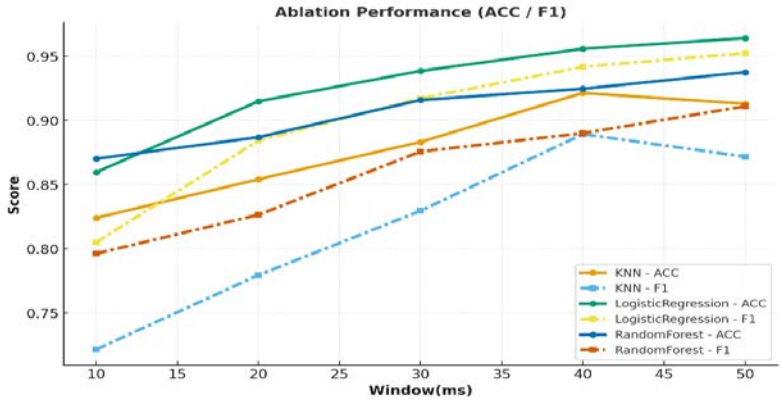

Figure 8. Segment length ablation results (10–50 ms) for Subject 3

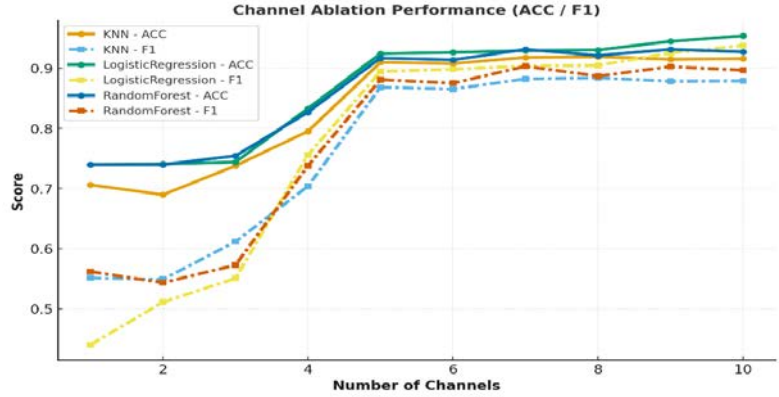

Figure 9. Channel ablation performance (1–10 channels) for Subject 3

Table 5. Classification performance of Subject 4 across different segment lengths (10–50 ms).

Classifier	10 ms (ACC/F1)	20 ms (ACC/F1)	30 ms (ACC/F1)	40 ms (ACC/F1)	50 ms (ACC/F1)
KNN	0.765 / 0.597	0.787 / 0.644	0.802 / 0.674	0.82 / 0.702	0.842 / 0.746
LogisticRegression	0.812 / 0.724	0.85 / 0.789	0.888 / 0.848	0.903 / 0.869	0.913 / 0.882
RandomForest	0.811 / 0.671	0.836 / 0.731	0.855 / 0.769	0.875 / 0.807	0.89 / 0.834

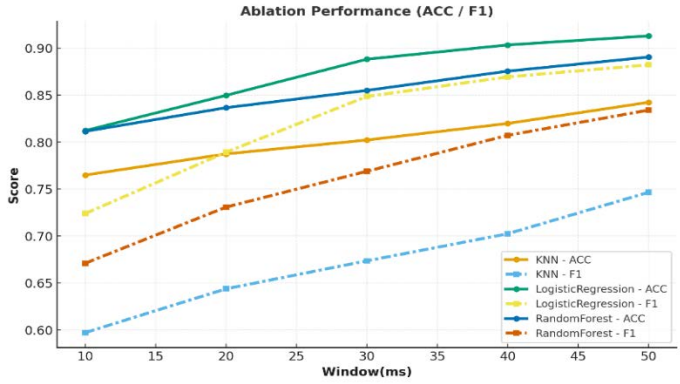

Figure 10. Segment length ablation results (10–50 ms) for Subject 4

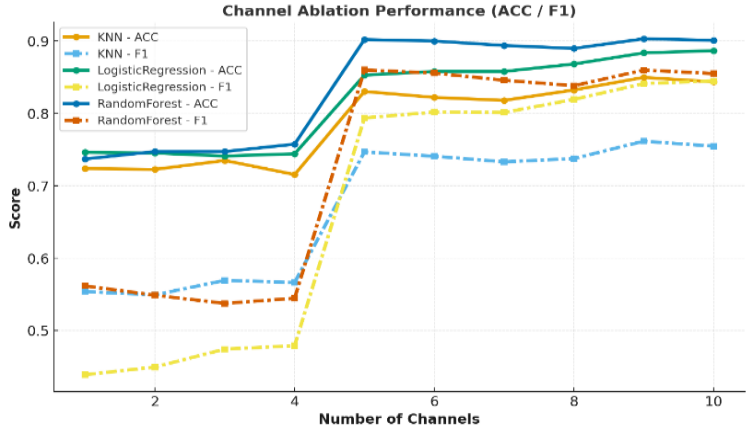

Figure 11. Channel ablation performance (1–10 channels) for Subject 4

Table 6. Classification performance of Subject 5 across different segment lengths (10–50 ms).

Classifier	10 ms (ACC/F1)	20 ms (ACC/F1)	30 ms (ACC/F1)	40 ms (ACC/F1)	50 ms (ACC/F1)
KNN	0.79 / 0.747	0.845 / 0.808	0.871 / 0.839	0.912 / 0.888	0.936 / 0.918
LogisticRegression	0.856 / 0.793	0.918 / 0.889	0.927 / 0.903	0.954 / 0.939	0.965 / 0.954
RandomForest	0.858 / 0.77	0.891 / 0.834	0.913 / 0.873	0.948 / 0.927	0.948 / 0.928

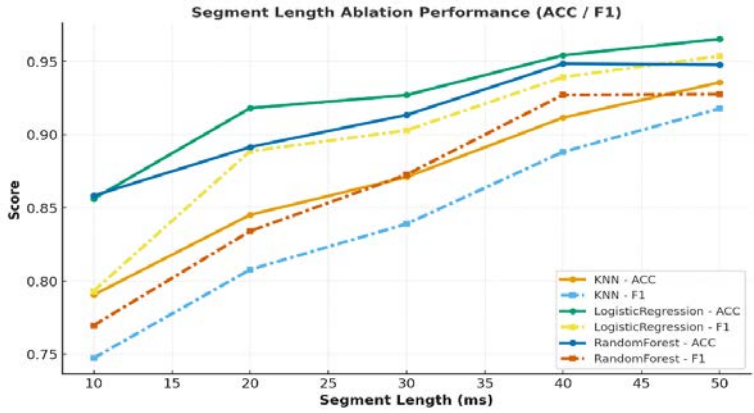

Figure 12. Segment length ablation results (10–50 ms) for Subject 5

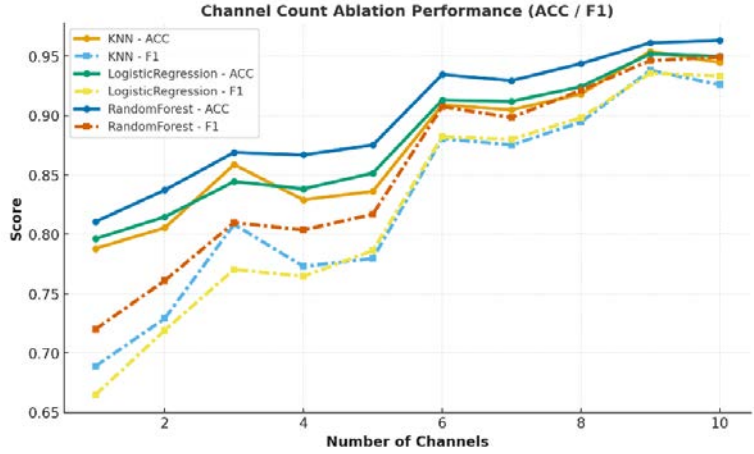

Figure 13. Channel ablation performance (1–10 channels) for Subject 5

5. CONCLUSION

The findings of this study clearly emphasize that the temporal and spatial configurations of EEG data—specifically segment length and channel count—are decisive factors in achieving high-performance cognitive state classification. The

systematic ablation analyses revealed that shorter segments provide better temporal sensitivity but may suffer from instability, whereas longer segments improve statistical reliability at the cost of reduced responsiveness. Among the tested configurations, window durations of 40–50 ms offered the most consistent balance between temporal resolution and feature robustness, producing the highest accuracy and F1-scores across classifiers.

Similarly, the channel ablation experiments demonstrated that classification accuracy rises sharply up to approximately six channels and then plateaus, indicating that a compact yet informative subset of electrodes is sufficient for robust EEG decoding. This result underscores the redundancy among neighboring channels and supports the use of correlation-based selection strategies for dimensionality reduction without compromising discriminative power.

Overall, the study highlights that optimizing both temporal segmentation and spatial channel configuration is essential for constructing efficient and generalizable EEG-based systems. Such an approach not only enhances computational efficiency but also provides practical benefits for real-time and wearable brain–computer interface (BCI) applications, where minimizing sensor count and processing overhead is as crucial as maintaining high classification accuracy.

REFERENCES

Al-Nafjan, A., & Aldayel, M. (2022). Predict Students' Attention in Online Learning Using EEG Data. *Sustainability 2022, Vol. 14, Page 6553*, *14*(11), 6553. https://doi.org/10.3390/SU14116553

Belcher, M. A., Hwang, I. C., Bhattacharya, S., Hairston, W. D., & Metcalfe, J. S. (2022). EEG-based prediction of driving events from passenger cognitive state using Morlet Wavelet and Evoked Responses. *Transportation Engineering*, *8*, 100107. https://doi.org/10.1016/J.TRENG.2022.100107

Cao, J., Garro, E. M., & Zhao, Y. (2022). EEG/fNIRS Based Workload Classification Using Functional Brain Connectivity and Machine Learning. *Sensors*, *22*(19), 7623. https://doi.org/10.3390/S22197623/S1

Guttmann-Flury, E., Sheng, X., & Zhu, X. (2023). Channel selection from source localization: A review of four EEG-based brain–computer interfaces paradigms. *Behavior Research Methods*, *55*(4), 1980–2003. https://doi.org/10.3758/S13428-022-01897-2/METRICS

Hadiyoso, S., & Rizal, A. (2017). Electrocardiogram signal classification using higher-order complexity of hjorth descriptor. *Advanced Science Letters*, *23*(5), 3972–3974.

Hag, A., Handayani, D., Pillai, T., Mantoro, T., Kit, M. H., & Al-Shargie, F. (2021). EEG Mental Stress Assessment Using Hybrid Multi-Domain Feature Sets of Functional Connectivity Network and Time-Frequency Features. *Sensors 2021, Vol. 21, Page 6300*, *21*(18), 6300. https://doi.org/10.3390/S21186300

Patel, P., Raghunandan, R., & Annavarapu, R. N. (2021). EEG-based human emotion recognition using entropy as a

feature extraction measure. *Brain Informatics*, *8*(1), 1–13. https://doi.org/10.1186/S40708-021-00141-5/FIGURES/4

Rahman, A. A., Siraji, M. I., Khalid, L. I., Faisal, F., Nishat, M. M., Islam, M. R., & Ibrahim Moubarak, N. N. (2022). Detection of Mental State from EEG Signal Data: An Investigation with Machine Learning Classifiers. *KST 2022 - 2022 14th International Conference on Knowledge and Smart Technology*, 152–166. https://doi.org/10.1109/KST53302.2022.9729084

Sharma, L. D., Bohat, V. K., Habib, M., Al-Zoubi, A. M., Faris, H., & Aljarah, I. (2022). Evolutionary inspired approach for mental stress detection using EEG signal. *Expert Systems with Applications*, *197*, 116634. https://doi.org/10.1016/J.ESWA.2022.116634

Sharma, R., & Meena, H. K. (2024). Emerging Trends in EEG Signal Processing: A Systematic Review. *SN Computer Science*, *5*(4), 1–14. https://doi.org/10.1007/S42979-024-02773-W/TABLES/5

Zyma, I., Tukaev, S., Seleznov, I., Kiyono, K., Popov, A., Chernykh, M., & Shpenkov, O. (2019). Electroencephalograms during Mental Arithmetic Task Performance. *Data 2019, Vol. 4, Page 14*, *4*(1), 14. https://doi.org/10.3390/DATA4010014

ENSURING THE SAFETY AND OPERATIONAL CONTINUITY OF TRANSPORTATION SYSTEMS AFTER EARTHQUAKES

Sedat OZCANAN[1]

1. INTRODUCTION

Earthquakes can generate significant and often devastating impacts on transportation systems, particularly in densely populated urban areas (Tierney & Bruneau, 2007). As a fundamental component of post-disaster emergency response and rescue operations, transportation infrastructure plays a critical role in ensuring effective intervention. Therefore, a seismically resilient and operational transportation network is vital for post-earthquake search-and-rescue activities and for enhancing community resilience.

Disruptions in transportation systems following an earthquake create severe interruptions not only for road users but also for logistics, healthcare, and emergency response services (Chang & Nojima, 2001). For instance, damage to critical links can delay evacuation procedures and restrict access for rescue teams. In this context, particularly in seismically active countries such as Turkey, the design of transportation systems must consider not only performance under normal operating conditions but also resilience under extreme events.

The literature presents various studies on seismic resilience and the continuity of transportation networks. Bruneau

[1] Assoc. Prof. Dr., Sirnak University, Faculty of Engineering, Department of Civil Engineering, ORCID: 0000-0002-8504-7611.

et al. (2003) proposed a quantitative framework for assessing the seismic resilience of communities. Tierney and Bruneau (2007) examined the resilience of transportation systems to disasters and analyzed their post-event recovery processes. However, a comprehensive and integrated approach specifically tailored to the Turkish context is still lacking; existing studies tend to focus on regional assessments or specific types of infrastructure.

Maintaining the functionality of transportation systems during and after an earthquake is crucial for the effectiveness of disaster management. As one of the most interconnected components of modern urban infrastructure, transportation networks hold a strategic position in both executing emergency response operations and meeting the essential needs of the public. Thus, the safety and continuity of transportation systems in the face of sudden and destructive hazards such as earthquakes constitute a central element of the contemporary "urban resilience" framework (Cimellaro, 2016). Cimellaro (2016) explains the performance of urban infrastructure during disasters through indicators such as "emergency response capacity" and "service continuity." In this framework, not only the physical robustness of transportation infrastructure but also the speed at which the network can be restored to service is identified as a determinant of overall system resilience. The study emphasizes that the uninterrupted operation of bridges, tunnels, and critical transportation corridors is essential for the success of search-and-rescue and evacuation operations. Boakye and Sobanjo (2018) analyzed the functional losses of regional transportation networks following earthquake-induced bridge damage. In their research, network resilience was evaluated based on performance loss, availability of alternative routes, and repair durations. Their findings reveal that the collapse of bridges with high centrality within the network dramatically reduces overall accessibility, highlighting the need to identify and prioritize the strengthening

of critical components at the network level. Liao et al. (2018) proposed resource allocation and repair prioritization algorithms that ensure the rapid restoration of transportation networks under earthquake scenarios. In these optimization-based approaches, network performance is enhanced through both structural (bridges, roads, tunnels) and operational (traffic rerouting, capacity management) strategies. The study underscores the necessity of integrating optimization-driven disaster management strategies into engineering infrastructures.

Cimellaro et al. (2018) demonstrated that, in seismic regions, both buildings and transportation infrastructure must be evaluated simultaneously. The authors emphasize that damage to transportation systems impacts not only physical mobility but also human movement, material flow, and emergency logistics. Accordingly, their system-based “disaster resilience assessment framework” proposes evaluating urban performance using integrated indicators such as average travel time, network connectivity ratio, and accessibility index. This approach can be used to identify which areas should receive priority funding to enhance transportation performance during emergency response operations. Lu et al. (2020) provided a comprehensive review of methods for quantifying resilience in engineering structures. Key indicators highlighted for transportation systems include functional continuity, service downtime, recovery rate, and minimization of economic losses. Their study emphasizes that developing digital, multi-disciplinary, data-integrated resilience metrics is critical for post-disaster decision-support systems.

The common conclusion emerging across the literature is that ensuring the safety and operational continuity of transportation systems during earthquakes cannot rely solely on structural retrofitting. It must also encompass network-level planning, preventive maintenance strategies, rapid repair protocols, and optimization-based disaster management

approaches. Future studies are encouraged to focus on AI-supported resilience modeling, data-driven damage prediction systems, and real-time transportation scenario analysis.

2. THE IMPACT OF EARTHQUAKES ON TRANSPORTATION SYSTEMS

Earthquakes can inflict damage on transportation infrastructure at varying levels, and these impacts are generally categorized into two main groups: structural and operational. Structural impacts refer to the direct physical damage sustained by bridges, tunnels, roadways, and railway lines. Operational impacts, on the other hand, encompass disruptions that affect system functionality and traffic flow (Ouyang, 2014). The common types of post-earthquake damage observed in transportation infrastructure are presented in Table 1.

Table 1. Common Types of Post-Earthquake Damage in Transportation Infrastructure

Infrastructure Type	Common Damage	Potential Impact
Roadway	Pavement cracking, landslides	Traffic disruption, delays in evacuation
Bridge/Viaduct	Pier damage, column cracking	Loss of critical connectivity, interruption of transport
Railway	Track deformation, bridge damage	Suspension of train operations
Port	Wharf and crane damage	Logistical disruptions
Airport	Runway and terminal damage	Delays in emergency evacuation and supply operations

2.1. Road Infrastructure

Road infrastructure is among the components that must be restored to operational use as quickly as possible following an earthquake. However, damage to bridges and viaducts can

significantly reduce the accessibility of critical routes. Analyses conducted after the Kobe earthquake in Japan reported that approximately 60% of bridges sustained partial damage, which in turn delayed the movement of emergency response vehicles (Chang & Shinozuka, 2004).

2.2. Railway Infrastructure

Railway systems are highly susceptible to disruptions during earthquakes, experiencing issues such as rail deformation and damage to bridges and tunnels. Such impacts lead to the suspension of train services and hinder the continuity of logistical flows. For instance, during the 2011 Van earthquake, damage along the railway corridor caused significant delays in the transportation of emergency relief supplies.

2.3. Airports and Seaports

Airports and seaports play a critical role in post-disaster supply and relief operations. Damage to runways and terminal facilities can disrupt aircraft operations, while impairment of port infrastructure can obstruct maritime transport. In particular, damage to port wharves, cranes, and storage areas can severely impede the delivery of food, medical supplies, and other essential goods.

2.4. Disruption Scenarios in Transportation Networks

Damage to critical junctions following an earthquake can disrupt the overall functionality of the transportation network. Therefore, the resilience of transportation systems should be evaluated not only based on the robustness of individual structural components but also through network-level flexibility and the availability of alternative routing options (FEMA, 2003). For example, Figure 1 illustrates the post-earthquake condition and accessibility structure of a representative transportation network composed of five critical nodes—North Bridge, West

Interchange, South Bridge, East Connector Road, and Central Interchange. These nodes hold strategic positions within the network and are essential for ensuring the continuity of vehicular traffic flow. In the figure, the functional states of the nodes are depicted using color codes: green nodes represent infrastructure elements operating at full capacity (“open”), yellow nodes indicate components functioning at reduced capacity (“restricted”), and red nodes denote elements that have become completely non-operational due to seismic impacts (“closed”). This visualization highlights how varying levels of damage across key nodes can significantly influence network-wide accessibility and operational performance.

The links within the network are depicted in two categories. Primary routes—shown with solid black lines—represent the major roadway connections that carry the majority of vehicular traffic under normal pre-earthquake operating conditions. These links ensure the main flow of traffic across the network and play a vital role in connecting critical bridges, interchanges, and arterial corridors. The loss of functionality in any of these primary links due to seismic impacts can lead to a substantial reduction in overall network performance and cause significant disruptions in traffic distribution.

Additionally, the figure illustrates alternative routes, marked with blue dashed lines, which serve to enhance post-disaster network resilience. These links represent secondary or backup pathways that become operational when primary routes are damaged or experience reduced capacity, thereby maintaining a certain level of transportation system functionality. For instance, even though the South Bridge is rendered non-operational (red node), alternative connections—such as the North Bridge–East Connector Road (A–D) and the West Interchange–Central Interchange (B–E)—enable the formation of a circulatory access route across the network. This example

underscores the importance of evaluating transportation systems within the broader framework of post-disaster recoverability and resilience.

Overall, the figure simultaneously highlights three fundamental components that influence transportation system performance following an earthquake:

(1). Structural integrity, reflected in the operational status of network nodes;

(2). Topological connectivity, representing the functional continuity of the primary road network; and

(3). Network flexibility and alternative routing capacity, demonstrated by the availability and effectiveness of backup links.

This analysis indicates that post-disaster accessibility assessments must extend beyond the damage states of individual structures and instead incorporate network-level functionality and the continuity of critical connections. Such network-based modeling approaches provide valuable decision-support tools, particularly for disaster management, emergency transportation planning, and the design of resilient infrastructure systems.

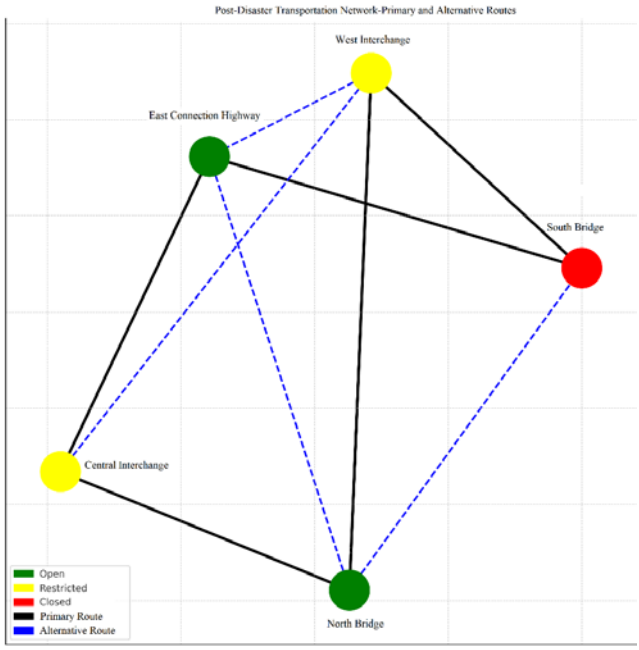

Figure 1. Post-Disaster Sample Transportation Network – Primary and Alternative Routes

3. DESIGN OF EARTHQUAKE-RESILIENT TRANSPORTATION SYSTEMS

The seismic resilience of transportation infrastructure is of critical importance both for ensuring the structural safety of physical assets and for maintaining continuous serviceability of the network. An earthquake-resilient design approach requires an integrated management framework that incorporates risk analysis, structural mitigation measures, appropriate material selection, and network-level planning (Bruneau et al., 2003).

3.1. Risk Analysis and Vulnerability Assessment

The first step in designing earthquake-resilient transportation systems is to identify the seismic hazards to which the infrastructure is exposed. This process involves conducting

seismic hazard analyses and evaluating site-specific factors such as soil conditions, topographic features, and the existing structural capacity of transportation assets. Through vulnerability assessment, critical corridors and structural components can be prioritized for mitigation or retrofitting interventions (Ouyang, 2014).

3.2. Structural Mitigation Measures

Structural mitigation is essential for enhancing the earthquake performance of critical infrastructure elements such as bridges, viaducts, and tunnels. Common measures include the use of seismic isolation devices, energy dissipation systems, flexible connections, and column retrofitting techniques. Kawashima (2004), in his evaluation of seismic isolation practices in Japanese highway bridges, highlights that following the 1995 Kobe Earthquake—during which steel bearings experienced severe damage—the widespread adoption of elastomeric isolation systems, including Lead Rubber Bearings (LRB) and High Damping Rubber Bearings (HDRB), significantly reduced seismic demands and bearing damage. An overview of seismic resilience measures for different types of transportation infrastructure is presented in Table 2.

Table 2. Seismic Resilience Measures for Different Types of Transportation Infrastructure

Infrastructure Type	Recommended Measures	Application Example
Bridge/Viaduct	Seismic isolation, energy dissipators, column retrofitting	Kobe, Japan
Highway/Roadway	Embankment stabilization, retaining wall reinforcement	Van, Turkey
Railway	Flexible rail connections, bridge strengthening	Tōhoku, Japan
Port	Wharf and crane foundation reinforcement	Port of Los Angeles, USA
Airport	Runway subbase reinforcement, flexible terminal connections	Sendai, Japan

3.3. Material and Technology Selection

The use of durable and high-performance materials significantly contributes to maintaining structural integrity during earthquakes. High-strength concrete, fiber-reinforced composites, and ductile steels should be preferred in bridge and roadway construction. In addition, the integration of smart sensor technologies and Structural Health Monitoring (SHM) systems is essential for real-time damage detection and effective maintenance planning (Lynch & Loh, 2006; Farrar & Worden, 2007).

3.4. Network Design and Flexibility

The resilience of a transportation system is not limited to the performance of individual structures; rather, it requires a network-based approach. Incorporating alternative routes, providing redundancy for critical links, and prioritizing essential connections enhance post-earthquake mobility and service continuity. Such an approach optimizes post-disaster logistics and evacuation capacity for affected communities (Bruneau et al., 2003).

4. DISASTER MANAGEMENT AND EMERGENCY PLANNING

The effective utilization of transportation systems following an earthquake constitutes a critical component of the disaster management process. Beyond structural resilience, the operational flexibility and crisis-management capacity of these systems are equally important (Coppola, 2015). Figure 2 illustrates the hierarchical structure depicting the coordinated functioning of transportation systems within the context of disaster management and emergency planning. In the diagram, an overarching disaster management framework is defined at the top

level, followed by two primary subcomponents: emergency response and evacuation planning, and operational and management strategies. Emergency response and evacuation planning guide the processes for identifying critical routes and prioritizing transportation corridors, whereas operational and management strategies encompass real-time traffic control, status monitoring, and team coordination supported by communication and information systems. Overall, the figure underscores the interconnected nature of strategic planning and operational management dimensions in ensuring the functionality of transportation infrastructure during the post-disaster period.

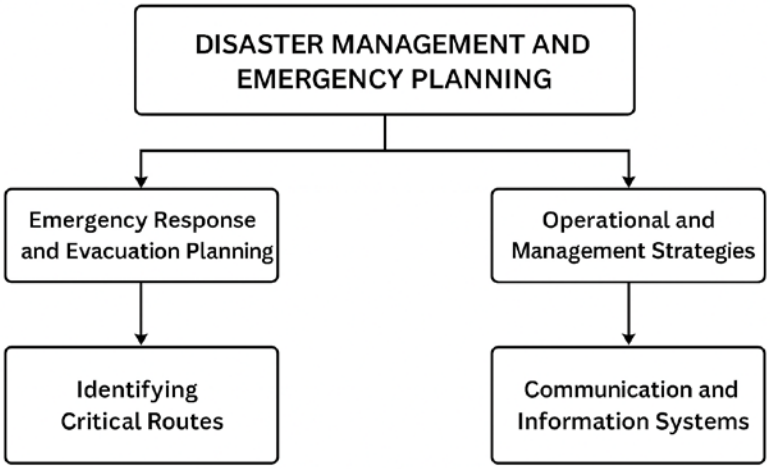

Figure 2. Disaster Management and Emergency Planning for Transportation Systems

4.1. Emergency Response and Evacuation Plans

Emergency planning ensures the effective use of transportation systems during and after a disaster. Evacuation routes, critical access points, and priority corridors for emergency service vehicles must be clearly identified. These plans should be coordinated by local authorities in collaboration with national disaster agencies.

4.2. Identification of Critical Routes

Priority roads and bridges used in emergency operations must maintain direct connectivity to hospitals, fire stations, and logistics hubs. In cases where these primary links are damaged, pre-designated alternative routes should be available. For instance, spatial analyses conducted after the 30 October 2020 Aegean Sea (Izmir) earthquake demonstrated that critical routes—such as pedestrian access paths to assembly areas and evacuation corridors—directly influence the effectiveness of post-disaster emergency logistics and evacuation operations (Partigöç & Erdin, 2024; Budak & Selçuk, 2025).

4.3. Operational and Management Strategies

Post-earthquake traffic management, temporary regulatory measures, and adaptive use of infrastructure are essential for maintaining system functionality. Strategies such as traffic signal adjustments, temporary one-way traffic operations, and the use of provisional bridges enhance operational continuity. Continuous monitoring of infrastructure usage and coordinated deployment of rapid-response teams are also of critical importance (Chang & Nojima, 2001; DesRoches et al., 2012; FHWA, 2013; Kermanshah & Derrible, 2017; FEMA, 2019).

4.4. Communication and Information Systems

Real-time communication and information systems play a vital role in crisis management. Smart-city technologies, GIS-based situational monitoring, and GPS data support the optimization of traffic flow and the effective deployment of emergency response teams. Public information dissemination and guidance also constitute key components that enhance overall system performance (Batty et al., 2012; Chen et al., 2008; Herrera et al., 2010; Kapucu, 2006; Perry & Lindell, 2003).

5. TECHNOLOGICAL AND INTELLIGENT SOLUTIONS

Technological innovations and intelligent systems play a critical role in enhancing post-earthquake accessibility and ensuring operational continuity within modern transportation networks (Chen et al., 2017; Batty et al., 2012; Zhang & Wang, 2016).

5.1. Intelligent Transportation Systems (ITS)

Intelligent Transportation Systems enable real-time monitoring and management of traffic flows. Following a disaster, ITS applications are particularly effective in assessing the accessibility of critical routes, preventing congestion, and guiding emergency response vehicles. For instance, during the Tōhoku earthquake in Japan, ITS infrastructure was actively utilized to optimize evacuation operations (Hara & Kuwahara, 2015; Zhou & Mahmassani, 2008).

5.2. Data-Driven Decision Support Systems

GIS-based platforms and simulation tools are widely used to analyze network performance and prioritize critical infrastructure components. These systems serve as essential decision-support mechanisms during both pre-disaster planning and real-time emergency management.

5.3. Future-Oriented Innovations

- **Autonomous Vehicles:** Enhance emergency response capacity through improved routing performance under traffic congestion and infrastructure damage conditions.
- **Drone Logistics:** Enable rapid and uninterrupted transport of critical supplies.

- **Blockchain-Based Supply Chain Management:** Ensures transparent and traceable logistics operations in the post-disaster environment.

A summary of contemporary technological innovations and their contributions to disaster management is presented in Table 3.

Table 3. Contributions of Technological Solutions to Disaster Management

Technology	Application Area	Contribution
ITS	Traffic management	Optimization of critical routes
GIS & Simulation	Decision support systems	Network resilience analysis
Autonomous Vehicles	Emergency logistics	Fast and safe delivery
Drone Logistics	Transport of critical goods	Continuity of transportation services
Blockchain	Supply chain management	Transparent and traceable logistics

6. CASE STUDIES AND SUCCESS EXAMPLES

6.1. Japan: The Kobe (1995) and Tōhoku (2011) Earthquakes

Japan is widely recognized as a global benchmark in the rapid restoration and functional continuity of transportation systems after major earthquakes. This success is largely attributed to pre-disaster multi-layered transportation plans, well-developed alternative route scenarios, and advanced monitoring technologies.

6.1.1. Kobe Earthquake (1995)

The 1995 Kobe Earthquake caused severe damage to the Hanshin Expressway and several critical bridges, significantly limiting the ability of emergency response teams to access

affected areas. However, Japan's strong maintenance programs, rapid structural retrofitting efforts, and activation of alternative routes enabled the quick restoration of logistical flows. Studies have confirmed that the post-disaster re-functionality of the transportation network reflects the effectiveness of the country's infrastructure management strategies (Chang & Shinozuka, 2004).

6.1.2. Tōhoku Earthquake (2011)

Following the 2011 Tōhoku Earthquake, Intelligent Transportation Systems (ITS), real-time monitoring technologies, and GPS-based traffic sensors played a critical role. These technologies facilitated real-time damage assessment, identification of road closures, and optimization of evacuation routes, enabling the transportation network to return to functional operation in a remarkably short time (Hara & Kuwahara, 2015). Japan's performance highlights the effectiveness of ITS-based strategies in enhancing post-disaster transportation resilience.

6.2. Turkey: The Van (2011) and İzmir (2020) Earthquakes

6.2.1. Van Earthquake (2011)

Structural damage to roads and bridges significantly hindered the access of search-and-rescue teams following the Van Earthquake. National reports indicate that prior identification of critical transportation corridors and planning of alternative access routes could have shortened emergency response times (FEMA, 2012). This case illustrates the importance of pre-disaster transportation planning in Turkey.

6.2.2. İzmir Earthquake (2020)

During the post-earthquake phase in İzmir, the rapid prioritization of critical links, deployment of temporary traffic management systems, and swift restoration of damaged road

components enhanced the effectiveness of evacuation and relief operations. Recent spatial analyses demonstrate that accurately identifying routes that provide access to assembly areas significantly improves post-disaster intervention capacity (Erdin & Partigöç, 2024).

6.3. International Comparisons

International literature consistently shows that the identification of pre-disaster resilience criteria, implementation of infrastructure retrofitting programs, and development of ITS-based traffic management systems directly influence post-earthquake response capacity. Systematic studies conducted in the United States, Japan, and several European countries reveal that the post-disaster performance of transportation networks largely depends on pre-disaster preparedness and technology-oriented management strategies (FHWA, 2013; Chang, 2000).

These international practices demonstrate that measures such as strengthening critical bridges, preparing alternative transport scenarios, expanding real-time monitoring systems, and implementing rapid damage assessment protocols significantly accelerate the restoration of transportation functionality after major disasters.

7. CONCLUSIONS AND RECOMMENDATIONS

Çalışmada Ensuring the safety and operability of transportation systems during an earthquake is crucial for enhancing societal resilience. Key findings derived from the analyses and case studies presented in this chapter include the following:

- **System safety is essential:** Earthquake-resistant infrastructure plays a vital role not only in maintaining

structural integrity but also in ensuring operational continuity.

- **Integrated planning is necessary:** Structural mitigation, network flexibility, technological solutions, and crisis management strategies must be designed in a complementary manner.
- **Technological and data-driven approaches:** ITS, GIS, and SHM systems are effective tools for monitoring and managing the accessibility of critical routes.
- **Future research directions:** The use of autonomous vehicles for emergency logistics, drone-supported transport operations, and blockchain-based supply chain systems represent promising innovative approaches to enhancing transportation system resilience.
- **Case studies as guidance:** Examples from Japan, Türkiye, and the United States underscore the importance of pre-identifying critical infrastructure components and designing flexible network structures.

A summary of the key success factors and recommended measures for post-earthquake transportation network performance is provided in Table 4.

Table 4. Success Factors in Post-Earthquake Transportation Systems

Factor	Description
Structural Resilience	Design of bridges, roads, and tunnels in accordance with seismic codes
Network Flexibility	Pre-identification of alternative routes and redundant connections
Use of Technology	Deployment of ITS, GIS, SHM, and data-driven decision systems
Operational Planning	Integration of evacuation, logistics, and emergency response plans
Communication & Coordination	Real-time information flow for the public and emergency teams

REFERENCES

Batty, M., Axhausen, K. W., Giannotti, F., Pozdnoukhov, A., Bazzani, A., Wachowicz, M., Ouzounis, G., & Portugali, Y. (2012). Smart cities of the future. *The European Physical Journal Special Topics, 214*(1), 481–518. https://doi.org/10.1140/epjst/e2012-01703-3

Boakye, R. T., & Sobanjo, J. O. (2018). Resilience of regional transportation networks subjected to hazard-induced bridge damages. *Journal of Transportation Engineering, Part A: Systems, 144*(10). https://doi.org/10.1061/JTEPBS.0000186

Bruneau, M., Chang, S. E., Eguchi, R. T., Lee, G. C., O'Rourke, T. D., Reinhorn, A. M., Shinozuka, M., Tierney, K. J., Wallace, W. A., & von Winterfeldt, D. (2003). A framework to quantitatively assess and enhance the seismic resilience of communities. *Earthquake Spectra, 19*(4), 733–752. https://doi.org/10.1193/1.1623497

Budak, L., & Selçuk, F. (2025). *Afete Dirençli İzmir Raporu I: İzmir'de afet toplanma alanlarına erişilebilirliğin mekânsal analizi*. İzmir Planlama Ajansı (İZPA).

Chang, S. E. (2000). Disasters and transport systems: Loss, recovery and competition at the Port of Kobe after the 1995 Earthquake. *Journal of Transport Geography, 8*(1), 53–65.

Chang, S. E., & Nojima, N. (2001). Measuring post-disaster transportation system performance: The 1995 Kobe earthquake in comparative perspective. *Transportation Research Part A: Policy and Practice, 35*(6), 475–494. https://doi.org/10.1016/S0965-8564(00)00003-3

Chang, S. E., & Shinozuka, M. (2004). Measuring improvements in the disaster resilience of communities. *Earthquake*

Spectra, 20(3), 739–755. https://doi.org/10.1193/1.1775796

Chen, R., Sharman, R., Rao, H. R., & Upadhyaya, S. J. (2008). Coordination in emergency response management: A case study of the South Florida emergency response infrastructure. *Decision Support Systems, 44*(4), 885–897. https://doi.org/10.1016/j.dss.2007.10.005

Chen, X., Zhang, L., & Yu, K. (2017). Intelligent transportation systems (ITS) for emergency response: A review. *Transportation Research Part C: Emerging Technologies, 85*, 363–380. https://doi.org/10.1016/j.trc.2017.09.028

Cimellaro, G. P. (2016). *Urban resilience for emergency response and recovery: Fundamental concepts and applications.* Springer.

Cimellaro, G. P., Arcidiacono, V., & Reinhorn, A. M. (2018). Disaster resilience assessment of building and transportation system. *Journal of Earthquake Engineering, 25*(4), 703–729. https://doi.org/10.1080/13632469.2018.1531090

Coppola, D. P. (2015). *Introduction to international disaster management.* Butterworth-Heinemann.

DesRoches, R., Padgett, J., Rix, G. J., Hammons, M., & Nielson, B. (2012). Impact of earthquakes on lifeline systems: Transportation. *Earthquake Spectra, 28*(S1), S531–S550. https://doi.org/10.1193/1.4000045

Farrar, C. R., & Worden, K. (2007). An introduction to structural health monitoring. *Philosophical Transactions of the Royal Society A, 365*(1851), 303–315. https://doi.org/10.1098/rsta.2006.1928

Federal Emergency Management Agency. (2019). *Lifelines and community resilience: Transportation systems.*

Federal Highway Administration. (2013). *Traffic management and transportation operations in emergencies.* U.S. Department of Transportation.

FEMA. (2003). *Guidelines for earthquake resistant design of transportation infrastructure.* Federal Emergency Management Agency.

FEMA. (2012). *Turkey earthquake response and assessment report.* Federal Emergency Management Agency.

FHWA. (2013). *Post-disaster transportation system performance: Lessons from U.S. earthquakes.* Federal Highway Administration.

Hara, Y., & Kuwahara, M. (2015). Traffic monitoring immediately after a major natural disaster: The Great East Japan Earthquake. *Transportation Research Part A: Policy and Practice, 75*, 1–15. https://doi.org/10.1016/j.tra.2015.02.002

Herrera, J. C., Work, D. B., Herring, R., Ban, X. J., Jacobson, Q., & Bayen, A. M. (2010). Evaluation of traffic data obtained via GPS-enabled mobile phones. *Transportation Research Part C: Emerging Technologies, 18*(4), 568–583. https://doi.org/10.1016/j.trc.2010.01.006

Kapucu, N. (2006). Interagency communication networks during emergencies: Boundary spanners in multiagency coordination. *The American Review of Public Administration, 36*(2), 207–225. https://doi.org/10.1177/0275074005283147

Kawashima, K. (2004). Seismic isolation of highway bridges. *Journal of Japan Association for Earthquake Engineering, 4*(3), 283–297.

Kermanshah, A., & Derrible, S. (2017). Transport network criticality assessment for post-disaster resilience: The role

of traffic flow. *Transportation Research Part D: Transport and Environment, 55*, 96–111. https://doi.org/10.1016/j.trd.2017.06.020

Liao, T. Y., Hu, T. Y., & Ko, Y. N. (2018). A resilience optimization model for transportation networks under disasters. *Natural Hazards, 93*, 469–489. https://doi.org/10.1007/s11069-018-3310-3

Lu, X. Z., Liao, W., Fang, D., Lin, K., Tian, Y., Zhang, C., Zheng, Z., & Zhao, P. (2020). Quantification of disaster resilience in civil engineering: A review. *Journal of Safety Science and Resilience, 1*, 19–30. https://doi.org/10.1016/j.jnlssr.2020.06.008

Lynch, J. P., & Loh, K. J. (2006). A summary review of wireless sensors and sensor networks for structural health monitoring. *The Shock and Vibration Digest, 38*, 91–130. https://doi.org/10.1177/0583102406061499

Ouyang, M. (2014). Review on modeling and simulation of interdependent critical infrastructure systems. *Reliability Engineering & System Safety, 121*, 43–60. https://doi.org/10.1016/j.ress.2013.06.040

Partigöç, N. S., & Erdin, H. E. (2024). 30 Ekim 2020 Ege Denizi depremi sonrası toplanma alanlarına yönelik kapasite yeterliliğinin değerlendirilmesi: Bayraklı ilçesi. *Afet ve Risk Dergisi, 7*(1), 242–255.

Perry, R. W., & Lindell, M. K. (2003). Preparedness for emergency response: Guidelines for the emergency planning process. *Disasters, 27*(4), 336–350. https://doi.org/10.1111/j.0361-3666.2003.00240.x

Tierney, K., & Bruneau, M. (2007). Conceptualizing and measuring resilience: A key to disaster loss reduction. *TR News, 250*, 10–20.

Zhang, Y., & Wang, D. (2016). Resilience-based analysis of transportation networks: A framework for post-disaster mobility. *Reliability Engineering & System Safety, 152*, 149–158. https://doi.org/10.1016/j.ress.2016.03.015

Zhou, X., & Mahmassani, H. S. (2008). Dynamic traffic assignment and simulation for advanced traveler information systems. *Transportation Research Part C: Emerging Technologies, 16*(2), 167–186. https://doi.org/10.1016/j.trc.2007.07.001

RADIATION DOSIMETRY AND MEASUREMENT METHODS

Özgül KARATAŞ[1]

1. INTRODUCTION

In recent years, the development of nuclear technology has led to a big increase in the use of high-energy ionizing radiation (X-rays, gamma rays, etc.) in many ways, including in industry, medical diagnostics, food preservation, nuclear reactors, and radioisotope research (Cleland et al., 2003; Sayyed et al., 2017). The development of nuclear technology is increasing concern about the harmful effects of ionizing radiation on human life. Prolonged exposure to this type of radiation can lead to deleterious effects such as cutaneous irritation, nausea, neoplasms, anemia, and even death (Sathiya and Ramachandran, 2024). Ionizing radiation is used extensively and constantly in many human activities and effective protection against exposure to it is necessary. So, we need systems that can accurately and sensitively measure radiation doses in environments where there is a radiation risk.

A dosimeter is a device that measures exposure to ionizing radiation in areas where radiation is present, either directly or indirectly. In other words, it measures the amount of energy transferred from a radiation field to a target and is frequently used in radiation assessments. It provides a

[1] Asst. Prof. Dr., Konya Technical University, Technical Sciences Vocational School, Department of Electricity and Energy, Nuclear Technology and Radiation Safety Program, ORCID: 0000-0003-3848-5800.

measurement of a property that varies depending on the amount of absorbed radiation in a predictable and repeatable manner.

Dosimeters are divided into two groups according to the detection method: active and passive (Yang et al., 2024). Active dosimeters measure radiation or light intensity by converting radiation intensity into an electrical signal based on the effect of light on electricity. Examples of this group include ion chambers, digital electronic pocket dosimeters, scintillation detectors, and pen dosimeters. In contrast, passive dosimeters detect energy accumulated in the environment through physical or chemical processes resulting from radiation interacting with matter. They only provide integrated data. Basic examples of passive dosimeters include thermoluminescence dosimeters (TLD), optically stimulated luminescence dosimeters, electron spin resonance dosimeters (ESR) and film dosimeters (Dönmez, 2017).

In some applications involving active radiation, such as measuring environmental or personal radiation exposure, only integrated dose information is important. In such cases, the dosimeter must operate continuously over long periods to detect the radiation. Passive dosimeters are an attractive option for such applications due to their low cost, robust construction, compact size and lack of continuous power requirement.

The characteristics and applications of each dosimeter type vary depending on the conditions. A variety of dosimeters made from different materials and operating using different mechanisms have been developed to meet the dosimetry range, sensitivity, accuracy and stability requirements of the system or field to be studied. Dosimetry is therefore a field of continuous research, as evidenced by studies and statistical data in the literature (Abaza, 2018; Seco et al., 2014; Chand et al., 2020). Research is being done in this area, but more studies are needed

to make new dosimeters and improve the old ones using the latest technology and developments in the nuclear industry.

2. FEATURES OF AN IDEAL DOSIMETER

To make sure that the dose is measured correctly and can be trusted in areas where there is radiation, a dosimeter must meet certain basic requirements. These include a linear energy and dose response, depending on irradiation intensity, a dosimetry range, sensitivity and stability, and repeatability and dependency on environmental conditions (Adl bookcase & Adlytė, 2017; Yang et al., 2024).

- **Dose response:** This shows the response of a selected parameter to the dose of irradiation. Ideally, this response would be linear with the dose. In nonlinear regions, large deviations can occur in the dose estimation process, meaning that a small error in the dosimeter signal can lead to significant errors. For ionizing radiation dosimetry, only the linear response range is relevant.
- **Dose Range:** It is a critical parameter to consider in dosimeter designs, and it is important to take it into account when planning and developing new dosimeters. The dose range is the difference between the smallest and largest doses that can be measured without a big error. The minimum absorbed dose is the lowest level of a substance that can be detected and is defined in relation to the dosimeter and the device used to read it. The most amount of radiation that can be absorbed depends only on the dosimeter.
- **Sensitivity:** This is how much the dosimeter reacts to a certain amount of radiation. High sensitivity is particularly important in applications where low doses are significant,

and this is especially true in cases where there is a need for precise measurement and accurate results. The sensitivity of a dosimeter can be affected by several factors. This includes how it is put together, the response that has been chosen, and how the information is read out.

- **Attenuation:** In passive dosimetry, the radiation dose is measured and then stored by the dosimeter before being read by the user using a suitable system. Depending on the application, the time interval between exposure and reading can vary considerably. Therefore, a dosimeter that is ideal should be able to store information about radiation dose for long periods of time without losing any of that information.
- **Repeatability:** This refers to a dosimeter's ability to produce the same result when measuring a constant dose of radiation. The precision and accuracy of dosimetry depend on this parameter.
- **Reusability:** As the dosimeter is not disposable, it can be used multiple times after being reset. This is typically achieved through heat or optical stimulation. However, high temperatures can alter the dose-response of some dosimeters, thus affecting their reusability.
- **Irradiation Intensity:** The intensity of the radiation source can vary significantly depending on the dosimetry application. A dosimeter reading following short-term exposure at a high dose rate should be equivalent to a reading following long-term exposure at a low dose rate. However, dose independence is only possible if the dosimeter response is linear with respect to irradiation intensity.
- **Dependence on Environmental Conditions:** The response of dosimeters is independent of environmental conditions

such as temperature, pressure and humidity, on account of the variation of these conditions during dosimetry. In practical applications, however, the response of some dosimeters is often subject to interference from these conditions, with appropriate calibration being necessary.

3. DOSIMETRE CALIBRATION AND VERIFICATION

Dosimetry procedures typically comprise two main stages: calibration and dose measurement. A known dose is received by the dosimeter during the calibration stage from a reference source. A specific external stimulus is then responded to with a signal reading. This reading can be used as the response parameter. It can also be used after processing. Generate a dose-dependent calibration curve for the response parameter by repeating the above steps after irradiating the dosimeter with different doses. The calibration curve, once acquired, allows the dosimeter to be used to determine the dose of radiation from an unknown source. For the dose to be evaluated, the same reading procedure for calibration must be employed. This is because the dosimeter's response or the calibration curve is usually dependent on the reading procedure and the instrument used. Comparisons of signals from unknown sources can be made using the calibration curve. Information can be obtained by comparing signals, which this can also be used for. (Dietze, 2001; McLaughlin & Desrosiers, 1995).

4. RADIATION DOSIMETER TYPES

4.1. Ion Chambers

Determining radiation doses in radiotherapy and diagnostic radiology involves the use of ion chambers, which

are active dosimeters. Calibrating the beam is also known as determining the dose under reference irradiation conditions. An ion chamber is essentially a gas-filled cavity that an outer wall with conductive properties surrounds and that contains a central collector electrode. The use of a high-quality insulator is for the separation of the wall and collector electrode, with the reduction of leakage current when a polarizing voltage is applied to the chamber as its purpose. The chamber is designed to minimize leakage by incorporating a guard electrode. The leakage current is interrupted by this, which allows it to flow to ground and bypass the collector electrode. Enhanced field uniformity within the active or sensitive volume of the chamber is also provided by this, which improves charge collection. While the shape and size of ion chambers can vary depending on specific requirements, they generally share the same characteristics (DeWerd and Smith, 2021; Abaza, 2018).

4.2. Film Dosimeters

Within the passive dosimeter group, film dosimeters are divided into two categories: radiographic films and radio chromic films. Radiography, radiotherapy and radiation protection all make use of radiographic X-ray films. Unexposed X-ray film consists of a thin plastic base with a special emulsion (a mixture of silver bromide and gelatin) on one or both sides. This emulsion is sensitive to radiation. The occurrence of interaction between the AgBr grains and radiation results in the production of a latent image on the film. This image is only rendered visible and permanent after processing, when the film darkens. Film provides excellent two-dimensional spatial resolution. This provides information about the spatial distribution of radiation of interest. It also provides information about radiation attenuation by intervening objects in a single exposure. However, films have a limited range of applications and are significantly dependent on energy for low-energy

photons. Although film is typically used to measure the dose of a substance, with the correct calibration, handling and analysis, it can also be used to assess it. Using radio chromic film for radiotherapy dosimetry is a relatively recent development. The most widely used type is GafChromic film. This colorless film has a chemical composition that is almost identical to tissue, and it turns blue when exposed to radiation. Radio chromic films contain a special dye that polymerizes when exposed to radiation. This polymer absorbs light. The amount of light transmitted through the film can be measured. This can be done using a suitable densitometer. As radio chromic films are graining less, they have a very high resolution and can be used in areas with high dose gradients for dosimetry. Radio chromic films have several advantages over radiographic films. They are easy to use; eliminate the need for darkroom facilities, film cassettes or film handling; are independent of dose rate; have improved energy properties; and are insensitive to ambient conditions. However, radio chromic films are generally less sensitive than radiographic films, making them more useful at higher doses (Izewska & Rajan, 2005; Abaza, 2018; Devic, 2011).

4.3. Semiconductor Dosimeters

The idea of semiconductors being used as detectors of ionizing radiation was first suggested in the 1950s. These detectors are classified as active dosimeters. These are a special type of instrument that can directly convert accumulated energy into specific electrical signals, such as charge, current, and voltage. The current or voltage response is proportional to the dose rate or irradiation intensity, making them useful for measuring instantaneous dose rates in medical treatment and industrial processes. The total dose can be calculated by the addition of the induced current or voltage over the exposure time. This gives a charge equivalent to the total dose. A practical

dosimetry system comprises three main components: a radiation detector, a signal acquirer and processor/storage unit, and a data transmitter and display. The detection component of the system converts light into electrical signals. This is achieved using a photodiode or phototransistor. However, the resulting electrical signal may be too weak. This could prevent the readout system from detecting it. This is particularly true at low dose rates/intensities. In this case, an amplifying circuit is used to generate a measurable electrical signal for further analysis. An integrated circuit then accumulates and processes these signals. The system stores these signals in real time and integrates them to provide the cumulative dose. For long-term operation, the dosimetry system requires a power source. Transmitting dose information to an electronic device via near-field communication depends on the detector type. The same applies to how the user perceives it (Yunusov et al., 1995; Rosenfeld, 2011).

4.4. Luminescence Dosimeters

Luminescence is when atoms, ions or molecules give off light when they are not very active. In certain solid-state substances, a proportion of this energy can be stored as held electronic charges. This stored energy can be let out by heating or using light to make the trapped charges move, which makes the light shine brighter. The brightness of the light depends on how much energy was stored. The term 'thermoluminescence' (TL) is used to describe the excitation of luminescence by heat, while 'optically stimulated luminescence' (OSL) is used to describe the excitation of luminescence by optical energy. The most common passive dosimeters are TL and OSL dosimeters. Typically, the temperature-dependent luminescence of a TL dosimeter is monitored by heating the material in a linear fashion. Light can be emitted when a released charge carrier is recombined with an oppositely charged carrier at the

luminescent centre. Information about the associated traps and the irradiation dose can be obtained by plotting the luminescence intensity against the sample temperature. The operating principle of OSL dosimeters is very similar to that of TL dosimeters, with both types of dosimeters measuring the dose based on the principle of ionization. Nevertheless, the accumulated charge is discharged by optical energy as opposed to thermal energy (Yukihara et al., 2022; Yang et al., 2024).

5. CONCLUSION AND DISCUSSION

A radiation dosimeter is a device that measures exposure to ionizing radiation. It is used for radiation protection, measuring the dose in medical and industrial processes. This study provides an overview of the fundamental principles and technologies of radiation dosimetry. Dosimeters and dosimetry systems can take many different forms and withstand various physical effects when storing and reading the dosimetric signal. The most used active and passive dosimeters are discussed in the study, and the availability of alternative protective systems is highlighted, particularly for high-risk nuclear applications involving exposure to ionizing radiation.

REFERENCES

Abaza, A. (2018). New trend in radiation dosimeters. *American Journal of Modern Physics*, *7*(1), 21-30.

Adlienė, D., & Adlytė, R. (2017). Dosimetry principles, dose measurements and radiation protection. *Applications of ionizing radiation in materials processing. Vol. 1*, 55-80.

Chand, B., Kumar, M., & Kumar, M. (2020). Comprehensive review of small field dosimetry. *European Journal of Molecular & Clinical Medicine*, *7*(7), 3595-607.

Cleland, M. R., Parks, L. A., & Cheng, S. J. N. I. (2003). Applications for radiation processing of materials. *Nuclear Instruments and Methods in Physics Research Section B: Beam Interactions with Materials and Atoms*, *208*, 66-73.

Devic, S. (2011). Radiochromic film dosimetry: past, present, and future. *Physica medica*, *27*(3), 122-134.

DeWerd, L. A., & Smith, B. R. (2021). Ionization chamber instrumentation. In *Radiation Therapy Dosimetry* (pp. 19-30). CRC Press.

Dietze, G. (2001). Dosimetric concepts and calibration of instruments. In *IRPA* (Vol. 10, No. 1-23, p. 307).

Dönmez, S. (2017). Radyasyon tespiti ve ölçümü. *Nucl Med Semin*, *3*, 172-177.

Izewska, J. O. A. N. N. A., & Rajan, G. (2005). Radiation dosimeters. *Radiation oncology physics: a handbook for teachers and students*, *36*, 71-99.

McLaughlin, W. L., & Desrosiers, M. F. (1995). Dosimetry systems for radiation processing. *Radiation Physics and Chemistry*, *46*(4-6), 1163-1174.

Rosenfeld, A. B. (2011, May). Advanced semiconductor dosimetry in radiation therapy. In *AIP Conference Proceedings* (Vol. 1345, No. 1, pp. 48-74). American Institute of Physics.

Sathiya, K., & Ramachandran, K. (2024). Impacts of Radiation on Human Health: A Narrative Review. *J Radiol Med Imaging*, *7*(1), 1-4.

Sayyed, M. I., Lakshminarayana, G., Kityk, I. V., & Mahdi, M. A. (2017). Evaluation of shielding parameters for heavy metal fluoride based tellurite-rich glasses for gamma ray shielding applications. *Radiation Physics and Chemistry*, *139*, 33-39.

Seco, J., Clasie, B., & Partridge, M. (2014). Review on the characteristics of radiation detectors for dosimetry and imaging. *Physics in Medicine & Biology*, *59*(20), R303.

Yang, Z., Vrielinck, H., Jacobsohn, L. G., Smet, P. F., & Poelman, D. (2024). Passive dosimeters for radiation dosimetry: materials, mechanisms, and applications. *Advanced Functional Materials*, *34*(41), 2406186.

Yukihara, E. G., McKeever, S. W., Andersen, C. E., Bos, A. J., Bailiff, I. K., Yoshimura, E. M., ... & Christensen, J. B. (2022). Luminescence dosimetry. *Nature Reviews Methods Primers*, *2*(1), 26.

Yunusov, M. S., Akhmadaliev, A., & Begmatov, K. A. (1995). Semiconductor detector as ionising radiation dosimeter. *Radiation Physics and Chemistry*, *46*(4-6), 1287-1290.

FERROCHROME PRODUCTION AND SUSTAINABLE VALORIZATION OF FERROCHROME SLAG: MATERIAL PROPERTIES, INDUSTRIAL APPLICATIONS, AND ENVIRONMENTAL CONSIDERATIONS

Osman Hulusi ÖREN[1]

1. INTRODUCTION

The production of ferrochrome began in 1821 when P. Bertier reduced Cr and FeO using charcoal, marking an important milestone in metallurgical history. In 1893, Mossian achieved industrial-scale production of high-carbon ferrochrome through the application of electrothermic methods, which represented a major technological breakthrough. Later, in 1907, Beket successfully produced low-carbon ferrochrome by reducing chromium with silicon (Habashi, 1997). Depending on their carbon content, ferrochromes are classified as high-, medium-, or low-carbon types and are primarily used as essential alloying components in stainless steel production. Due to their corrosion resistance and high hardness, ferrochromes are also employed as strengthening additives in steel manufacturing.

Globally, approximately 90% of mined chromium is used in ferrochrome production, of which about 90% is consumed in stainless steel manufacturing (Rozhikhina, et al., 2020). Ferrochrome production is highly energy-intensive; in Turkey, approximately 4,300 kWh of electricity is required to produce one

[1] Asst. Prof. Dr., Sirnak University, Faculty of Engineering, Department of Civil Engineering, ORCID: 0000-0001-7601-5549.

ton of ferrochrome. This high energy demand significantly increases production costs, reducing the competitiveness of the domestic industry (Yılmaz and Sütaş, 2008). Countries such as South Africa, Kazakhstan, and India—where energy costs are substantially lower—dominate global ferrochrome production (USGS, 2019).

In Turkey, annual production of low-carbon ferrochrome is approximately 10,000 tons in Antalya, while high-carbon ferrochrome production reaches about 150,000 tons in Elazığ Guleman. Despite the high metallurgical quality of Turkish chromite ores, rising energy expenses have resulted in reduced production levels. Data from the Istanbul Mineral Exporters' Association (İMİB) indicate that ferrochrome output fell by 18%, dropping from 124,524 tons in 2017 to 103,432 tons in 2020. Among all ferroalloy products, ferrochrome maintains the highest export value, with the main export destinations being the Netherlands, Italy, and Sweden (İMİB, 2020).

During ferrochrome smelting, ferrochrome slag (FS) forms as a by-product, produced through high-temperature reactions between the gangue minerals in chromite ore and the added fluxes and reducing agents. On average, 1 ton of ferrochrome production generates 1.1–1.6 tons of slag, depending on ore grade and process efficiency (Beukes, et al., 2010). The global generation of FS exceeds 12 million tons annually, with South Africa being the leading producer due to its dominant role in ferrochrome manufacturing (Singh, et al., 2021). In Turkey, the annual FS generation is estimated at approximately 250,000–300,000 tons, mainly concentrated around Elazığ and Antalya smelting facilities (Kaya, et al., 2019).

FS exhibits high density, hardness, and chemical stability, which makes it a suitable material for use in construction applications, road base layers, cement additives, and refractory

aggregates. Recent research has shown that it can serve as a partial replacement for natural aggregates in concrete and asphalt mixtures, and can also be utilized in geopolymer and ceramic production, thereby supporting sustainable material management and waste valorization. (Singh, et al., 2021; Kaya, et al., 2019).

Ferrochrome and its slag thus represent not only critical inputs for stainless steel production but also emerging materials in sustainable construction and industrial recycling. Improving energy efficiency, enhancing slag reutilization, and reducing production costs are essential strategies for increasing Turkey's competitiveness in the global ferrochrome sector.

2. FERROCHROME SLAG

Steel slag, a by-product of steel production, is considered a desirable alternative material in various engineering applications. Initially, researchers attempted to reduce slag generation by improving steelmaking processes or by reintroducing slag into the production cycle. However, these methods proved to be costly and inefficient at an industrial scale. Consequently, research has shifted toward exploring how steel slag can be reused in other fields (Amelian, et al., 2018; Skaf, et al., 2017).

In Europe, steelmaking slags are predominantly used as aggregate in road construction (46%), while smaller quantities are utilized in metallurgy and agriculture as fertilizers. The remaining portion is either disposed of as waste (14%) or stored on-site (8%) (Euroslag, 2016). In advanced industrial economies like the United States, Japan, Germany, and France, slag recycling rates reach almost 100%. About half is utilized directly as road base material, while the remaining portion is recovered through sintering and ironmaking processes. In contrast, the utilization rate of slag in China remains relatively low—around 22% as of

2012 (Yi, et al., 2012).According to the International Stainless Steel Forum (ISSF, 2021), global stainless steel production increased by 16.9% in the first nine months of 2021, reaching 43.0 million tons. It is estimated that approximately 0.3 tons of slag are generated per ton of stainless steel produced, corresponding to a total of about 13 million tons of stainless steel slag in 2021 (ISSF, 2021).

The quantity of slag produced during ferrochrome manufacturing depends on the specific type of ferrochrome being produced. Globally, the annual production of high-carbon ferrochrome is approximately 13 million tons. The production of one ton of high-carbon ferrochrome generates between 1.1 and 1.6 tons of ferrochrome slag, leading to an estimated global annual slag output of around 17 million tons. For low-carbon ferrochrome, each ton of product generates 2.4–2.5 tons of slag, resulting in a global annual production of 0.9 million tons, which corresponds to a total of 2.2 million tons of FS per year. (Horckmans, et al., 2019).

Although a significant portion of stainless steel and FS produced in Europe are utilized in the construction sector (e.g., road building, cement, and concrete additives), their relatively high chromium (Cr) content (1–10 wt%) poses a major challenge to full utilization. Additionally, the volume instability caused by high free lime content and environmental concerns arising from heavy metal leaching mean that a portion of these slags is still disposed of in landfills (Karhu, et al., 2020). Nevertheless, studies have shown that chromium leaching from FS remains within the limits established by the U.S. Environmental Protection Agency (USEPA) (5 mg/L for Cr), indicating that these materials are not considered potential pollutants. Toxicity Characteristic Leaching Procedure (TCLP) test results for Elazığ ferrochrome slag produced in Turkey indicated chromium leaching concentrations

of 0.54 mg/L for crushed samples and 0.80 mg/L for ground samples (Erdem, et al., 2005).

2.1. Production

In ferrochrome production, ore extracted from chromite mines is transported to the processing facility. At the beginning of production, the ore is ground and formed into pellets to ready it for sintering. The pellets are heated in a furnace and sintered at temperatures reaching 1400 °C. Prior to smelting, the chromium-bearing material undergoes preheating at 500–800 °C. Afterward, the sintered ore undergoes reduction in an electric arc furnace, transforming the chromium and iron oxides into metal. During this reduction process, a portion of the silica is also reduced, and the resulting metal is referred to as “charge chrome” (Zelic, 2005). Figure 1 illustrates the overall process of ferrochrome production.

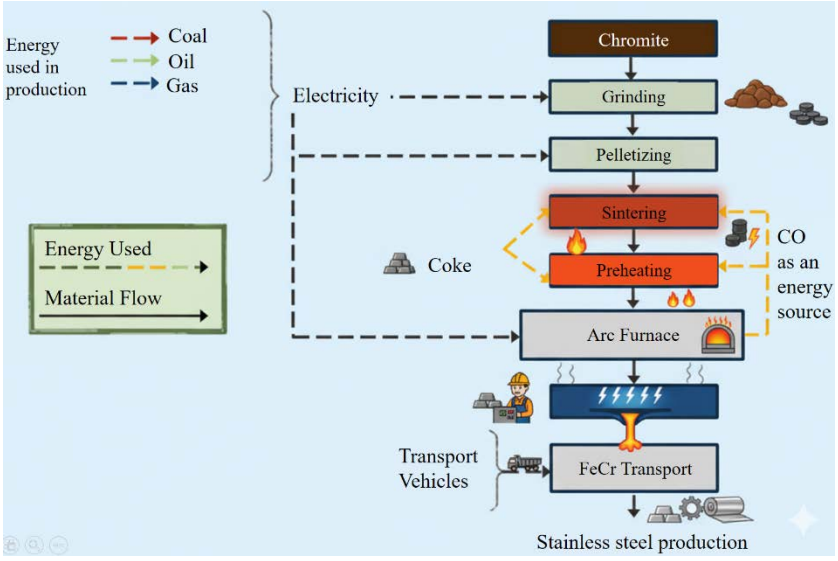

Figure 1. Typical reduction reactions in the ferrochrome furnace (Niemelä and Kauppi, 2007)

The submerged arc furnace is the most widely used method for smelting chromite ores with carbon-based reductants.

(Zelic, 2005). Chromite, a mineral with the general formula $(Fe^{2+}, Mg^{2+})O\cdot(Al^{3+}, Cr^{3+}, Fe^{3+})_2O_3$, has a spinel structure. During the smelting process, chromite produces both slag and molten metal. The denser ferrochrome metal forms droplets within the slag layer, enabling it to separate from the slag and settle at the bottom of the furnace. Both slag and metal exit through the same tap hole, while the low-density slag collected on top is poured off to separate it from the metal. For practical use, the molten slag is granulated (Niemelä and Kauppi, 2007; Wang, et al., 2021).

The slag's composition and melting point primarily depend on the fluxing agents added during smelting. Quartzite is often added as a flux to lower the slag's melting temperature. Ferrochrome slag contains varying amounts of SiO_2, MgO, and Al_2O_3, along with minor quantities of CaO, Cr_2O_3, and Fe_2O_3 (Zelic, 2005; Kim, et al., 2019).

The smelting process also generates carbon monoxide gas and slag as by-products. Carbon monoxide is generated as a by-product of the reduction reactions (Li, et al., 2020). Insoluble materials within the metallic ferrochrome phases form the silanate phases that constitute the primary slag. Ferrochrome and slag produced in the electric arc furnace are periodically transferred to ladles. FS products are categorized into granulated slag and crushed-and-screened slag. The majority of the slag is in granulated form, while the crushed and screened slag is produced from air-cooled nodules collected at different process stages (Niemelä and Kauppi, 2007; Zhang, et al., 2022)

2.2. Physical properties

For engineering applications, it is crucial to determine the specific physical properties of raw materials, including shape, size, density, and water absorption. Moreover, assessing the mechanical properties of the material—such as its resistance to abrasion, impact, and crushing—is highly important. The

different physical properties of FS, when used as fine and coarse aggregates, are presented in Tables 1 and 2 (Fares, et al., 2021).

Table 1. Physical properties of ferrochrome slag as coarse aggregate (Fares, et al., 2021).

Properties	Ferrochrome Slag	Limestone	Granite
Specific Gravity	2.14-3.21	2.5-2.82	2.83
Bulk Density (kg/m^3)	1480-2182	-	-
Water Absorption(%)	0.30-2.32	0.50-0.73	0.20
Abrasion (%)	18.19-25.84	22.0-30.0	1.60

Table 2. Physical properties of ferrochrome slag as fine aggregate (Fares, et al., 2021).

Properties	Ferrochrome Slag	River Sand
Specific Gravity	2.52-3.27	2.6-2.70
Bulk Density (kg/m^3)	1164-1870	-
Water Absorption (%)	0.63-0.8	1.10-3.15
Fineness Modulus	2.38-4.80	2.0-3.10
Thermal Conductivity (W/mK)	0.27-0.96	-

The specific gravity of FS as coarse aggregate ranges between 2.63 and 3.21 g/cm³, which is relatively higher than that of conventional limestone aggregate. This higher specific gravity compared to traditional aggregates is attributed to FS's content of heavy metals such as Mg and Fe (Sahu, et al., 2016). As shown in Table 1., the bulk density of FS is also higher than that of conventional granite and limestone aggregates, ranging between 1480 and 2182 kg/m³.

FS has a water absorption rate exceeding 2%, which is higher than that of conventional concrete aggregates. Consequently, when using FS as an aggregate in concrete or asphalt, adjustments to the water and bitumen content calculations should be taken into account. The high water absorption is related to the porosity and structural formula of FS. Previous studies report that impact, crushing, and abrasion values are below 20% (Sahu, et al., 2016), making coarse FS aggregate

a suitable alternative for areas subjected to wear, such as concrete pavements and flooring.

The number of studies investigating the physical and mechanical properties of granulated FS remains limited. Nevertheless, granulated FS appears to meet the general requirements for fine aggregate in concrete, including particle size distribution and water absorption. The fineness modulus of granulated FS ranges between 2.38 and 4.8, while water absorption values are between 0.63% and 0.80% (Fares, et al., 2021).

2.3. Chemical properties

The composition of FS is influenced by the chromium content of the slag, its overall chemical composition, temperature, and the tapping arrangement (Hayes, 2004). During casting, the slag temperature ranges from 1700 to 1750 °C, while the ferrochrome temperature is between 1550 and 1600 °C; however, in practical ferrochrome production, the optimum smelting temperature typically varies between 1680 and 1720 °C. The chemical composition of FS generally consists of: SiO_2: 15–30%, Al_2O_3: 19–33%, MgO: 13–25%, CaO: 1–5%, Cr: 1–18% (as unreduced CrO or Cr_2O_3 or entrapped in ferrochrome metal), and Fe: 1–12% (as either unreduced FeO or trapped ferrochrome metal) (Nkohla, 2006).

Table 3. Chemical properties of ferrochrome slag (Fares, et al., 2021).

Chemical properties (%)							
SiO_2	**Al_2O_3**	**Fe_2O_3**	**CaO**	**MgO**	**$Cr2O_3$**	**SO_3**	**K_2O + Na_2O**
21.28-59.70	7.9-31.09	0.61-10.00	0.49-47.35	5.70-38.50	2.12-33.38	0-3.68	0-0.41

Slag viscosity, which varies with pressure and temperature, is a key factor in separating slag from the metal. Table 3 presents the range of chemical compositions for FS

(Fares, et al.,2021). The total chemical composition of the slag also governs the sequence of crystallization during cooling, with the cooling rate affecting the degree of crystallization. The evolution of mineralogical phases in the FS system is largely determined by the slag's chemical composition, cooling rate, and the way it solidifies. Additionally, the slag's chemical composition is affected by the ore type, smelting process, partial oxygen pressure, reduction temperature, and the duration that materials remain in the furnace's high-temperature zones (Hayes, 2004).

Understanding the melting and crystallization process of FS is crucial for controlling the development of crystalline phases that influence the product's durability, heat resistance, density, and chromium retention. The melting and crystallization behavior of F belongs to the broad $CaO\text{-}Al_2O_3\text{-}MgO\text{-}SiO_2$ system. During cooling, MgO, MgO+spinel, and MgO+spinel+forsterite crystals precipitate from the molten solution. The final ferrochrome contains phases such as chromite spinel, forsterite, enstatite, anorthite, and minor phases like spinel and chromium carbide (Hayhurst, 1974).

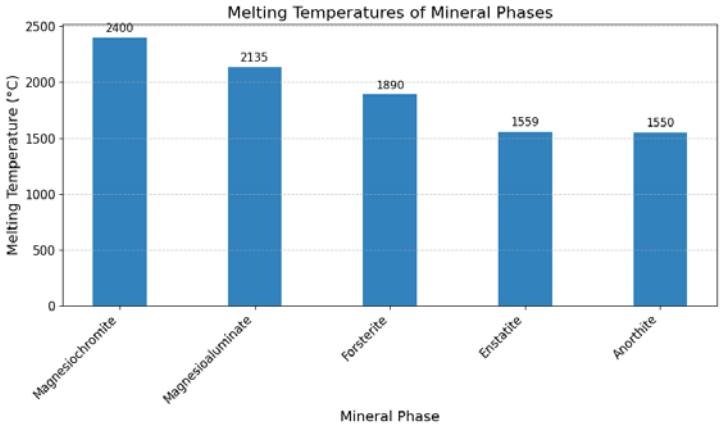

Figure 2. Phase composition of ferrochrome slag and the melting temperatures of the phases (Fares, et al., 2021).

FS is produced from chromite containing chromium and iron oxides, which typically occurs as fine heaps or lumps that can accumulate in furnaces. Fine materials in casting furnaces can negatively affect production. Different types of carbon are employed to reduce metal oxides in the furnace, with high-grade furnace coke playing a particularly important role. Strict quality control of raw materials ensures optimal yield and consistent casting quality.

To achieve the correct slag composition, quartzite, bauxite, dolomite, corundum, lime, and olivine are used as fluxing agents. The materials obtained from the casting furnaces include the ferrochrome alloy and slag. With modern process control and good quality management, the optimum slag composition can be obtained. The most critical factors include temperature, slag composition, viscosity, and electrical conductivity. The main components of the slag are SiO_2, MgO, and Al_2O_3, along with Cr and Fe oxides and CaO. The primary phases of the slag are glass, spinel, and phosphorite (Niemelä and Kauppi, 2007). SEM images of FS show a partially crystalline, dense, and homogeneous amorphous matrix (Tanskanen and Maknonen, 2006). Utilization Areas of Ferrochrome Slag

3. UTILIZATION AREAS OF FERROCHROME SLAG

In the iron and steel industry, slags generated as by-products of metal production are widely utilized as asphalt and concrete aggregates, railway ballast, and as base materials in road construction. These slags are also used in the manufacturing of prefabricated structural components, bricks, and construction materials. FS, in particular, finds application in the ceramics and refractory industries, high-valent chromium processing, and various civil engineering applications.

Producers of ferrochrome in Finland, Sweden, and Russia have successfully employed these waste materials in road construction and building applications. The superior combination of high-strength and refractory phases in FS enables its use in road construction, building materials, refractory products, and as fill material (Sahu, et al., 2016).

The composition of FS includes high-refractory phases, such as spinel and forsterite, along with low-melting-point phases rich in calcium, aluminum, chromium, and iron oxides, including enstatite and silicate glass. Consequently, FS shows chemical properties akin to conventional refractory materials (Tanskanen and Maknonen, 2006).

The refractory characteristics of FS can be improved by raising the levels of MgO, Al_2O_3, and Cr_2O_3, either individually or together. However, the glassy phases and metallic ferrochrome present in FS can negatively affect its refractory performance. The refractory strength of high-carbon F can be improved by transforming low-melting-point phases into high-refractory phases. For instance, the addition of 20% MgO can raise the refractory temperature of FS to 1740 °C (Ashimov, et al., 1984). Conventional low-cement castables can be prepared using high-carbon ferrochrome, calcined bauxite, high-alumina cement, and a small amount of microsilica (Kumar, et al., 2014).

In concrete pavements, FS as an aggregate is more cost-effective than conventional magmatic stones. Air-cooled FS is typically employed as coarse aggregate in high-strength concrete due to its larger particle size and strength, while water-cooled granulated FS, with its finer texture, is more appropriate for use as fine aggregate in concrete mixtures. (Zelic, 2005). Numerous studies on incorporating FS into asphalt and concrete pavements have indicated that, owing to its high strength and exceptional

resistance to abrasion, FS can effectively replace natural aggregates (Zelic, 2005; Lind, et al., 2001).

4. CONCLUSION

Ferrochrome production has evolved into a strategically important but energy-intensive process, primarily supporting stainless steel manufacturing worldwide. Despite the high metallurgical quality of Turkish chromite ores, domestic production is constrained by high energy costs, highlighting the need for cost-effective smelting technologies and efficient resource management. Globally, countries with lower energy costs dominate production, emphasizing the economic pressures inherent in the ferroalloy sector.

FS, a significant by-product of smelting, offers substantial potential for sustainable industrial applications. Its high density, hardness, and chemical stability enable its use in concrete, asphalt, refractory products, and road construction. While chromium content and free lime pose challenges to full utilization, proper processing and quality control can mitigate environmental risks, including heavy metal leaching, ensuring safe incorporation into construction materials.

The physical and chemical characteristics of FS, including specific gravity, water absorption, and crystalline phase composition, are critical in determining its suitability for engineering applications. Granulated and crushed slag can serve as effective substitutes for conventional aggregates in high-strength concrete and asphalt pavements, while high-refractory phases enhance performance in refractory products. Optimizing energy efficiency, production processes, and slag valorization strategies is essential for improving competitiveness and promoting sustainable material management within the global ferrochrome industry.

REFERENCES

Amelian, S., Manian, N., Abtahi, S. and Goli, M. (2018). Steel slag applications in construction materials: A review. Construction and Building Materials, 188, 1103–1114. https://doi.org/10.1016/j.conbuildmat.2018.08.009

Ashimov, S. B., Bolotov, I. A. and Satvaldiev, R. S. (1984). Refractory properties of high-carbon ferrochrome. Moscow: Metallurgy Press.

Beukes, J. P., Dawson, N. F. and Van Zyl, P. G. (2010). Theoretical and practical aspects of Cr(VI) in the South African ferrochrome industry. Journal of the Southern African Institute of Mining and Metallurgy, 110(12), 743–750.

Euroslag. (2016). Steel slag statistics in Europe. Brussels, Belgium: European Slag Association.

Erdem, M., Altundogan, H. S., Turan, M. and Tumen, F. (2005). Characterization and leaching behavior of ferrochrome slag. Journal of Hazardous Materials, 123(1–3), 123–130. https://doi.org/10.1016/j.jhazmat.2005.03.041

Fares, H., Sohel, M., Al-Jabri, K. and Al-Mamun, A. (2021). Physical and mechanical properties of ferrochrome aggregates for concrete applications. Construction and Building Materials, 280, 122500. https://doi.org/10.1016/j.conbuildmat.2021.122500

Habashi, F. (1997). Handbook of extractive metallurgy. Weinheim: Wiley-VCH Verlag GmbH. https://onlinelibrary.wiley.com/doi/book/10.1002/9783527619571

Hayes, P. (2004). The metallurgy of ferrochrome. London, UK: Institute of Materials.

Hayhurst, D. R. (1974). Phase formation in ferrochrome alloys. Journal of the Less Common Metals, 35(1), 1–12. https://doi.org/10.1016/0022-5088(74)90105-6

Horckmans, L., Vandenberghe, L., De Craemer, S. et al. (2019). Global ferrochrome production and slag generation. Journal of Cleaner Production, 234, 1234–1245. https://doi.org/10.1016/j.jclepro.2019.06.123

International Stainless-Steel Forum (ISSF). (2021). World stainless steel production statistics – Q1–Q3 2021. Brussels, Belgium: ISSF.

İMİB (İstanbul Maden İhracatçıları Birliği). (2020). Faaliyet raporu 2020. https://www.imib.org.tr/tr/faaliyet-raporlari.html

Karhu, M., Talling, J., Piotrowska, M., Matas, J. and Adams, A. (2020). Environmental challenges of steel and ferrochrome slag utilization. Resources, Conservation and Recycling, 161, 104953. https://doi.org/10.1016/j.resconrec.2020.104953

Kaya, A., Gökçe, A. and Erdem, R. (2019). Ferrokrom cürufunun inşaat sektöründe alternatif malzeme olarak değerlendirilmesi. Pamukkale Üniversitesi Mühendislik Bilimleri Dergisi, 25(4), 487–495. https://doi.org/10.5505/pajes.2019.65832

Kim, J., Park, S. and Lee, H. (2019). Characterization and utilization of ferrochrome slag from submerged arc furnaces. Journal of Cleaner Production, 234, 123–134. https://doi.org/10.1016/j.jclepro.2019.06.045

Kumar, R., Srivastava, R., Majhi, S. and Singh, B. (2014). Utilization of ferrochrome slag in low-cement castables. Ceramics International, 40(6), 7851–7857. https://doi.org/10.1016/j.ceramint.2014.02.051

Li, Y., Chen, X. and Wang, F. (2020). Gas emissions and environmental impacts during ferrochrome production. Environmental Science & Technology, 54(7), 4567–4578. https://doi.org/10.1021/acs.est.0c00234

Lind, H., Fällman, L. and Larsson, M. (2001). Use of ferrochrome slag as aggregate in concrete and asphalt pavements. Waste Management, 21(5), 449–457. https://doi.org/10.1016/S0956-053X(01)00008-3

Niemelä, R. and Kauppi, H. (2007). Ferrochrome production and slag processing techniques. Helsinki: Metallurgical Publications.

Nkohla, P. (2006). Chemical composition and properties of ferrochrome slag. Journal of Metals, 58(5), 32–38.

Rozhikhina, I. D., Nokhrina, O. I., Yolkin, A. A. and Golodova, M. A. (2020). Ferrochrome production and its environmental impact. Metallurgist, 64(1–2), 102–109. https://doi.org/10.1007/s11015-020-00969-3

Sahu, J., Biswas, S. and Kapure, S. (2016). Physical and mechanical characterization of ferrochrome slag for construction applications. Construction and Building Materials, 123, 1–10. https://doi.org/10.1016/j.conbuildmat.2016.07.039

Singh, R., Mohanty, B. and Naik, B. (2021). Sustainable utilization of ferrochrome slag in construction and environmental applications. Journal of Cleaner Production, 279, 123689. https://doi.org/10.1016/j.jclepro.2020.123689

Skaf, M., Boudenne, A., Denis, S. et al. (2017). Use of steel slag in road construction: Environmental and mechanical assessment. Construction and Building Materials, 135,

416–427. https://doi.org/10.1016/j.conbuildmat.2016.12.102

Tanskanen, P. and Maknonen, J. (2006). Microstructural analysis of ferrochrome slag. Journal of Materials Processing Technology, 177(1–3), 175–181. https://doi.org/10.1016/j.jmatprotec.2006.04.030

USGS (U.S. Geological Survey). (2019). Mineral commodity summaries: Chromium. Reston, VA: U.S. Department of the Interior. https://pubs.usgs.gov/periodicals/mcs2020/mcs2020-chromium.pdf

Wang, Q., Liu, J. and Zhang, Y. (2021). Ferrochrome slag granulation and reuse in the metallurgical industry. Minerals Engineering, 170, 107038. https://doi.org/10.1016/j.mineng.2021.107038

Yi, W., Zhang, Q., Li, H. et al. (2012). Current utilization of steel slag in China. Journal of Materials in Civil Engineering, 24(4), 420–428. https://doi.org/10.1061/(ASCE)MT.1943-5533.0000478

Yılmaz, M. and Sütaş, İ. (2008). Türkiye'de ferrokrom üretimi ve enerji maliyetlerinin etkisi. Metalurji Dergisi, 143(3), 35–42. https://www.metalurji.org.tr/dergi/

Zelic, O. (2005). Ferrochrome: Production, properties, and utilization. Belgrade: Mining Institute Press.

Zhang, L., Hu, X. and Sun, Y. (2022). Processing and classification of electric arc furnace slags: Granulation and screening techniques. Journal of Materials Research and Technology, 20, 532–545. https://doi.org/10.1016/j.jmrt.2022.01.075

GRADED DESIGN OF FUNCTIONAL LAYERS IN PROTON EXCHANGE MEMBRANE FUEL CELLS: NEW APPROACHES WITH RESPECT TO PERFORMANCE, COST AND DURABILITY

Mehmet Şefik ÜNEY[1]

Mehmet Latif LEVENT[2]

1. INTRODUCTION

Proton exchange membrane fuel cells (PEMFCs) are energy conversion systems that directly convert the chemical energy of hydrogen into electrical energy (Jamil et. al, 2022). They are distinguished by their low operating temperature, high efficiency, and zero-emission characteristics. However, the commercialization of this technology is hindered by two major challenges: the high cost of platinum catalysts and limited durability (Seselj et. al, 2023).

The primary cause of these issues lies in the homogeneous design of membrane electrode assemblies (MEAs). In a homogeneous MEA, under varying operating conditions particularly at high current densities the distribution of reactants and products becomes non-uniform. Consequently, reactant starvation occurs in some regions, while water flooding develops in others, leading to significant irregularities in current density and temperature distribution.

[1] Asst. Prof. Dr., Batman Üniversitesi, Department of Electricity and Energy, Vocational School, Batman University, Turkey, ORCID: 0000-0003-4743-0764.

[2] Asst. Prof. Dr., Hakkari University, Faculty of Engineering, Department of Electrical and Electronics Engineering, Hakkari/Türkiye, ORCID: 0000-0002-7185-9029.

These irregularities not only cause performance degradation but also lead to localized material degradation (Shan et. al, 2016). For example, membrane drying in hot spots reduces proton conductivity, while in flooded regions, oxygen transport is hindered. Therefore, in recent years, researchers have increasingly focused on the concept of graded MEA design.

The graded design approach involves spatially varying the physical, chemical, or morphological properties of the four main components of the MEA namely, the gas diffusion layer (GDL), microporous layer (MPL), catalyst layer (CL), and membrane (Yuan et. al, 2022). This spatial optimization enables balanced transport of charge, heat, and mass throughout the cell, resulting in higher performance with reduced platinum loading.

2. FUNDAMENTAL OPERATING PRINCIPLE OF PEM FUEL CELLS

As shown in Figure 1, a proton exchange membrane fuel cell (PEMFC) consists of an anode, a cathode, a proton-conducting membrane, and gas diffusion layers (GDLs) forming a layered structure (Guo et. al, 2022).

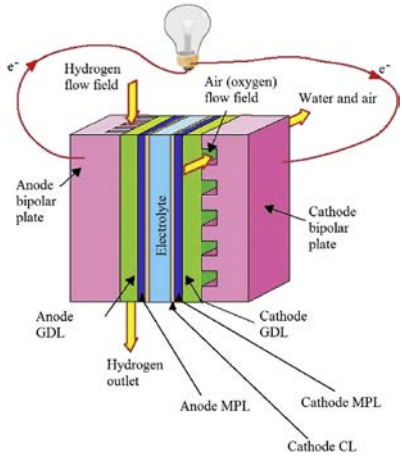

Figure 1. Schematic cross-section of a typical PEM fuel cell.

At the anode, hydrogen molecules are split into protons and electrons, a process referred to as the anodic reaction:

$$H^2 \rightarrow 2H^+ + 2e^- \quad (1)$$

While the protons migrate through the membrane, the electrons travel through the external circuit to reach the cathode, where oxygen reduction and water formation occur:

$$\frac{1}{2}O_2 + 2H^+ + 2e^- \rightarrow H_2O \quad (2)$$

The overall electrochemical reaction taking place in the cell can be expressed as:

$$H_2 + \frac{1}{2}O_2 \rightarrow H_2O + electric\ energy + heat \quad (3)$$

The theoretical cell voltage (reversible potential) is defined by the Nernst equation:

$$E = E^0 + \frac{RT}{2F}\ln\left(\frac{{p_{H_2}p_{O_2}}^{1/2}}{p_{H_2O}}\right) \quad (4)$$

Here, E^0=1.229 V (25 °C, 1 atm), R is the universal gas constant, T is the temperature, F is the Faraday constant, and p_{H2}, p_{O2}, p_{H2O} are the partial pressures of hydrogen, oxygen, and water, respectively.

In practice, the actual cell voltage is lower than the theoretical value due to activation, ohmic, and mass transport losses.

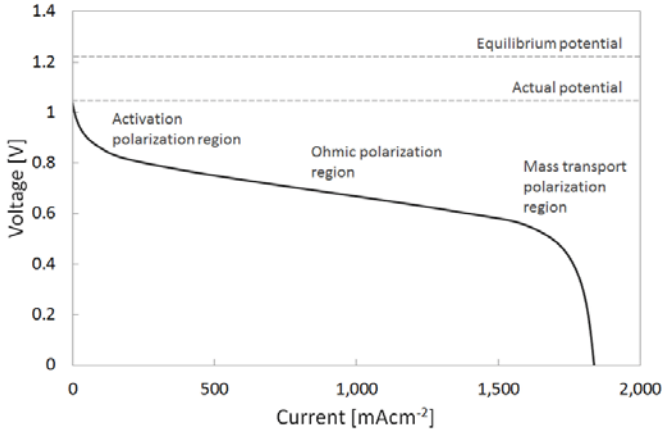

Figure 2. Typical PEMFC polarization curve showing activation, ohmic, and mass transport loss regions.

The magnitude of these losses depends on material properties and current density. Figure 2 illustrates the impact of these losses on the cell voltage.

3. CURRENT DENSITY DISTRIBUTION AND CAUSES OF NON-UNIFORMITIES

Current density serves as a key indicator of how effectively the ionic and electronic pathways function within a fuel cell (Gidey et. al, 2012). However, in homogeneous MEAs, this distribution is never perfectly uniform. The primary causes of these non-uniformities are as follows:

- Gas transport imbalance: The partial pressure of oxygen decreases along the flow channel, leading to concentration gradients.
- Porosity variations: Differences in the permeability of gas and liquid phases create uneven mass transfer resistance.
- Temperature gradients: Thermal expansion and water evaporation alter membrane hydration levels.

- Contact resistance: Uneven compression between bipolar plates and gas diffusion layers results in local variations in resistance.

The combined effect of these factors leads to the formation of hot spots and localized material degradation. Such phenomena contribute to both performance losses and durability issues.

The graded design approach aims to systematically minimize these non-uniformities by spatially tailoring material properties and structural characteristics across the MEA, ensuring a more balanced current and heat distribution throughout the cell.

4. CONCEPT AND FUNDAMENTAL APPROACH OF GRADING

Grading refers to the spatial variation of material properties within a structure. In the context of MEAs, this concept involves intentionally altering the physical, chemical, or morphological characteristics of a layer as a function of position (Kundu et. al, 2006).

This variability can be considered in two dimensions:

- Through-plane grading: A difference in properties is created between the gas-facing side and the membrane-facing side of a layer.
- In-plane grading: Variations are introduced along the flow direction to account for changes in reactant consumption and product generation.

The main grading parameters typically include porosity (ε), tortuosity (τ), PTFE content, catalyst loading, ionomer ratio, electronic conductivity (σ), and protonic conductivity (κ). These

parameters directly influence the equations governing diffusion reaction balance:

$$\nabla.\left(D_{eff}\nabla C\right) - R(C,\eta) = 0 \quad (5)$$

$$\nabla.\left(\sigma_{eff}\nabla\phi_s\right) = ai_{faradaic} \quad (6)$$

$$\nabla.\left(K_{eff}\nabla\phi_m\right) = -ai_{faradaic} \quad (7)$$

Here, D_{eff}, σ_{eff}, κ_{eff} represent the effective diffusion coefficient, electronic conductivity, and protonic conductivity, respectively. These quantities are typically correlated with porosity through the Bruggeman relationship:

$$D_{eff} = D_0\varepsilon^{1.5}, \sigma_{eff} = \sigma_0\varepsilon^{1.5} \quad (8)$$

These relationships demonstrate, in mathematical terms, that a graded structure enables optimized transport rates in different regions of the MEA, allowing the balance of diffusion and reaction processes throughout the cell.

5. GRADING IN THE GAS DIFFUSION LAYER (GDL)

The gas diffusion layer (GDL) facilitates the transport of gases to the electrodes while also providing pathways for water removal [8]. This dual functionality can be optimized through gradients in porosity, PTFE content, and thickness across the layer.

As shown in Figure 3, the upper region of the GDL (facing the flow channel) typically features low PTFE content and high porosity, which enhances oxygen diffusion. In contrast, the lower region (adjacent to the catalyst layer) has higher PTFE content, which regulates capillary transport, thereby preventing both excessive water accumulation (flooding) and complete drying of the structure.

Additionally, the fiber orientation within the GDL significantly influences the electrical conductivity profile under compression. Uneven compression can lead to localized increases in resistance and current non-uniformity. Therefore, graded GDL structures are designed to minimize such variations and ensure uniform current distribution across the cell.

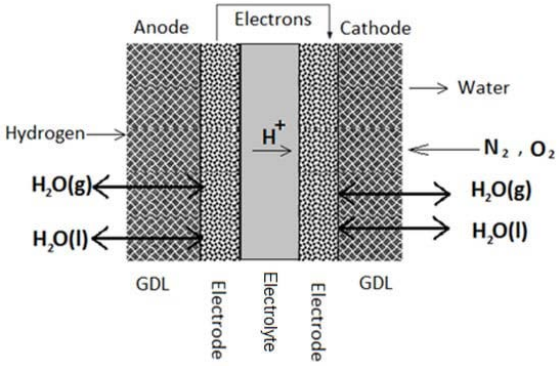

Figure 3. Schematic representation of a graded GDL structure.

6. GRADING IN THE MICROPOROUS LAYER (MPL)

The microporous layer (MPL) serves as a bridge between the gas diffusion layer (GDL) and the catalyst layer (CL) (Zhang et. al & Chen, 2022). As illustrated in Figure 4, the MPL generally consists of two sub-layers, each characterized by different PTFE contents and carbon morphologies.

The MPL plays a critical role in regulating capillary transport. The upper layer (adjacent to the GDL) possesses a larger pore structure and higher electrical conductivity, allowing efficient gas passage. Conversely, the lower layer (facing the CL) exhibits smaller pores and is more hydrophobic, facilitating the upward transport of water through capillary action.

From an electrical standpoint, a well-adhered MPL reduces surface potential variations by ensuring uniform contact across interfaces. Furthermore, this layer helps to smooth current streamlines within the reaction zone, thereby improving electrode performance and long-term stability.

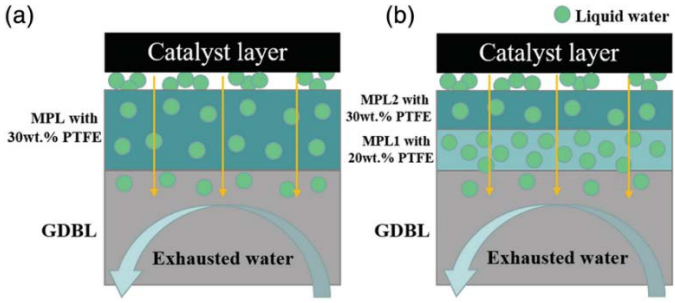

Figure 4. Schematic representation of a dual-layer MPL with different PTFE contents and carbon morphologies.

7. GRADING IN THE CATALYST LAYER (CL)

The catalyst layer (CL) is the most complex and performance-defining region of the membrane electrode assembly (MEA) (Wilke, et. al, 2025). As depicted in Figure 5, grading within this layer can be implemented along three primary dimensions.

The first is the ionomer gradient: near the membrane, a higher ionomer content enhances proton conduction, whereas on the gas side, a lower ionomer fraction improves gas accessibility and diffusion.

The second is the platinum (Pt) distribution: a higher Pt loading near the membrane promotes catalytic activity and reaction kinetics, while a lower loading on the gas side reduces material cost without significantly compromising performance.

The third dimension is the pore architecture: a multi-modal structure combining macro, meso, and micropores

balances the transport of gas, protons, and water, optimizing overall reaction efficiency.

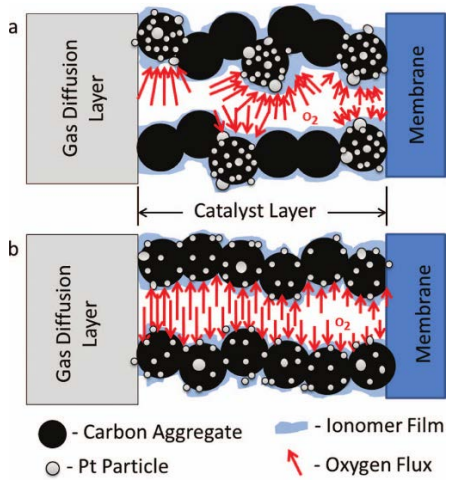

Figure 5. Ionomer and platinum concentration profiles within the catalyst layer.

This structural design simultaneously reduces activation losses and mitigates mass transport resistance at high current densities. The local reaction rate is expressed by the Butler–Volmer equation:

$$i = i_0 \left[exp\left(\frac{\alpha_a F \eta}{RT}\right) - exp\left(-\frac{\alpha_a F \eta}{RT}\right)\right] \quad (9)$$

Here, i_0 represents the exchange current density, which depends on the electrochemically active surface area (ECSA). In a graded structure, spatial variation in ECSA directly affects the local reaction intensity.

From an engineering perspective, this approach enables the reduction of total platinum loading while maintaining equivalent electrochemical performance, contributing to a lower-cost yet high-efficiency fuel cell design.

8. GRADING IN THE MEMBRANE

The membrane is the layer where proton transport occurs and plays a direct role in determining the overall performance of the fuel cell (Tang, Zhang). As shown in Figure 6, varying the ion-exchange capacity (IEC) and water retention capability across the membrane thickness can simultaneously enhance proton conductivity and mechanical strength.

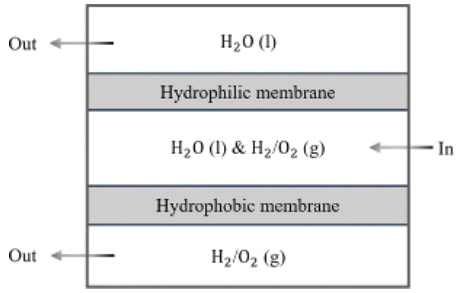

Figure 6. Membrane structure with a graded proton conductivity profile.

In regions near the catalyst interfaces, a high water-retention capability facilitates proton conduction by maintaining proper membrane hydration. In contrast, the central region of the membrane typically incorporates a reinforced structure, improving mechanical stability and resistance to deformation under hydration, dehydration cycles.

Furthermore, the application of radical scavenger or barrier coatings on membrane surfaces can significantly slow down chemical degradation, particularly that caused by hydroxyl (•OH) radicals. These surface modifications extend membrane lifetime and maintain performance stability over long-term operation.

9. MANUFACTURING METHODS

The fabrication of graded MEAs requires the controlled spatial deposition of different material compositions at specific locations within the assembly. As illustrated in Figure 7, several manufacturing techniques can be employed to achieve such structural and compositional gradients.

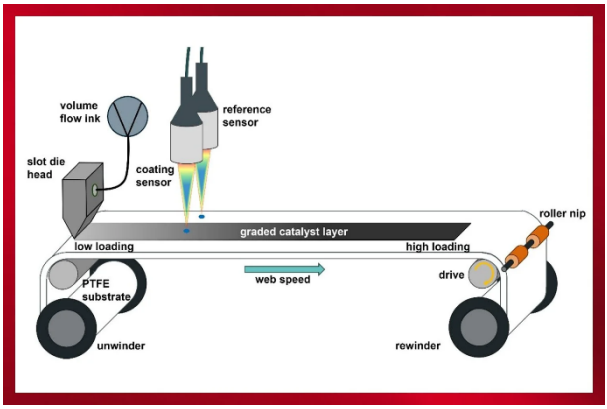

Figure 7. Schematic illustration of the main fabrication methods used for producing graded MEAs.

One of the primary methods is slot-die coating, which utilizes multi-reservoir systems to vary the composition across the thickness of the deposited layer, enabling precise through-plane grading (Ren et. al, 2023).

The masked spraying technique allows for in-plane grading by applying different material mixtures to specific planar regions, enabling local tuning of catalyst or ionomer distribution.

Electrospinning enables the fabrication of nanofiber-based structures, offering precise control over pore morphology and fiber alignment, which are critical for optimizing gas and water transport.

Finally, lamination techniques can be used to combine two layers with distinct porosities, such as GDLs or MPLs, to

construct composite graded structures that deliver both efficient gas diffusion and effective water management.

10. DIAGNOSTICS AND MODELING

The impact of graded structures on fuel cell performance is evaluated using both experimental and numerical approaches.

Among experimental techniques, segmented current collectors are particularly useful for mapping current density distributions across the cell surface, revealing local variations in electrochemical activity.

Electrochemical impedance spectroscopy (EIS) enables the separation and quantification of different resistance components ohmic, activation, and diffusion within the cell (Padha et. al, 2022).

Neutron imaging provides operando visualization of water accumulation and evaporation, offering insights into transient water management behavior.

Thermal imaging helps evaluate the temperature uniformity within the cell, identifying hotspots and validating thermal management strategies.

In addition, three-dimensional multiphysics modeling allows for the simultaneous simulation of electrical, thermal, gas, and water transport processes, providing a comprehensive understanding of the coupled phenomena occurring within graded MEAs.

The integration of these experimental and numerical techniques offers a powerful feedback mechanism for optimizing grading parameters, ultimately guiding the rational design of high-performance and durable MEAs.

11. PERFORMANCE, COST AND DURABILITY EVALUATION

Graded MEAs enable higher power density to be achieved with the same amount of platinum catalyst (KP et. Al, 2022). As shown in Figure 8, this design approach can reduce platinum usage by 30–50% while simultaneously increasing performance by 10–20%.

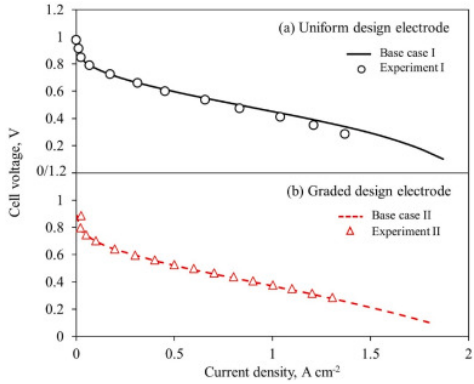

Figure 8. Comparison of performance and durability between homogeneous and graded MEAs.

Moreover, grading helps mitigate current and temperature gradients within the cell, which in turn reduces carbon corrosion and membrane degradation. As a result, the electrochemical environment becomes more uniform, minimizing localized stresses and extending component lifetimes.

Long-term durability tests have demonstrated that graded MEAs can operate for approximately twice as long as homogeneous ones under identical conditions, highlighting the strong potential of grading to balance performance, cost efficiency, and durability in next-generation PEM fuel cells.

12. CONCLUSION AND FUTURE PERSPECTIVES

The graded membrane electrode design enables the simultaneous optimization of performance, cost, and durability in proton exchange membrane fuel cells (PEMFCs). Through this approach, platinum loading can be reduced while maintaining or even enhancing power output, current and temperature distributions can be homogenized, and water management can be significantly improved. Consequently, material degradation is mitigated, resulting in higher overall efficiency and extended operational lifetime of the system.

Future research will focus on integrating graded structures with scalable manufacturing techniques, advancing operando diagnostic tools, and coupling multiphysics models with artificial intelligence based optimization algorithms. These developments are expected to accelerate the transition of graded MEA concepts from laboratory prototypes to commercially viable fuel cell systems.

In conclusion, the graded MEA concept represents a new paradigm in fuel cell technology one that offers a sustainable pathway toward achieving the high-performance, low-cost, and long-lifetime objectives required for widespread adoption. This design philosophy marks a turning point in the development of efficient, durable, and economically competitive energy conversion technologies.

REFERENCES

Giddey, S., Badwal, S. P. S., Kulkarni, A., & Munnings, C. (2012). A comprehensive review of direct carbon fuel cell technology. *Progress in Energy and Combustion Science*, *38*(3), 360-399.

Guo, H., Chen, L., Ismail, S. A., Jiang, L., Guo, S., Gu, J., ... & Han, D. (2022). Gas diffusion layer for proton exchange membrane fuel cells: a review. *Materials*, *15*(24), 8800.

Jamil, A., Rafiq, S., Iqbal, T., Khan, H. A. A., Khan, H. M., Azeem, B., ... & Hanbazazah, A. S. (2022). Current status and future perspectives of proton exchange membranes for hydrogen fuel cells. *Chemosphere*, *303*, 135204.

KP, V. B., Varghese, G., Joseph, T. V., & Chippar, P. (2022). Optimization of graded catalyst layer to enhance uniformity of current density and performance of high temperature-polymer electrolyte membrane fuel cell. *International Journal of Hydrogen Energy*, *47*(6), 4018-4032.

Kundu, S., Fowler, M. W., Simon, L. C., & Grot, S. (2006). Morphological features (defects) in fuel cell membrane electrode assemblies. *Journal of Power Sources*, *157*(2), 650-656.

Okonkwo, P. C., & Otor, C. (2021). A review of gas diffusion layer properties and water management in proton exchange membrane fuel cell system. *International Journal of Energy Research*, *45*(3), 3780-3800.

Padha, B., Verma, S., Mahajan, P., & Arya, S. (2022). Electrochemical impedance spectroscopy (EIS) performance analysis and challenges in fuel cell applications. *Journal of Electrochemical Science and Technology*, *13*(2), 167-176.

Ren, H., Meng, X., Lin, Y., Li, X., & Shao, Z. (2023). Surface enrichment of ionomer in fuel cell catalyst layer prepared using slot-die coating method. *Journal of power sources*, *580*, 233399.

Seselj, N., Alfaro, S. M., Bompolaki, E., Cleemann, L. N., Torres, T., & Azizi, K. (2023). Catalyst development for high-temperature polymer electrolyte membrane fuel cell (HT-PEMFC) applications. *Advanced Materials*, *35*(40), 2302207.

Shan, J., Lin, R., Xia, S., Liu, D., & Zhang, Q. (2016). Local resolved investigation of PEMFC performance degradation mechanism during dynamic driving cycle. *International journal of hydrogen energy*, *41*(7), 4239-4250.

Tang, M., Zhang, S., & Chen, S. (2022). Pt utilization in proton exchange membrane fuel cells: structure impacting factors and mechanistic insights. *Chemical Society Reviews*, *51*(4), 1529-1546.

Wilke, V., Rivera, M., Morawietz, T., Sata, N., Mues, L., Hegelheimer, M., ... & Friedrich, K. A. (2025). Novel atmospherically plasma sprayed micro porous layer for anion exchange membrane water electrolysis operating with supporting electrolyte. *Electrochemical Science Advances*, *5*(3), e202400036.

Yuan, X. Z., Shaigan, N., Song, C., Aujla, M., Neburchilov, V., Kwan, J. T. H., ... & Fatih, K. (2022). The porous transport layer in proton exchange membrane water electrolysis: perspectives on a complex component. *Sustainable Energy & Fuels*, *6*(8), 1824-1853.

Zhang, J., Wang, B., Jin, J., Yang, S., & Li, G. (2022). A review of the microporous layer in proton exchange membrane

fuel cells: Materials and structural designs based on water transport mechanism. *Renewable and Sustainable Energy Reviews*, *156*, 111998.

DEVELOPMENTS IN THE FIELD OF ENGINEERING 2025

yaz
yayınları

YAZ Yayınları
M.İhtisas OSB Mah. 4A Cad. No:3/3
İscehisar / AFYONKARAHİSAR
Tel : (0 531) 880 92 99
yazyayinlari@gmail.com • www.yazyayinlari.com

ISBN: 978-625-8508-85-7